From the Comprehensive Pneumology Center (CPC)

in collaboration with the Department of Medicine V, University Hospital

of the Ludwig-Maximilians-University Munich,

the Asklepios Pulmonary Hospital Munich-Gauting

and the Helmholtz Center Munich

Dissertation

zum Erwerb des Doctor of Philosophy (Ph.D.) an der

Medizinischen Fakultät

der Ludwig-Maximilians-Universität zu München

Secretory to multi-ciliated cell imbalance by altered cellular progeny in end-stage COPD facilitates resilience to environmental pollutants

vorgelegt von:

Dr.med. Mircea-Gabriel Stoleriu

geboren in Iasi, Rumänien

2022

Mit Genehmigung der Medizinischen Fakultät der

Ludwig-Maximilians-Universität zu München

First Supervisor: PD Dr. med. Anne Hilgendorff

Second supervisor: Prof. Dr. Dr. med. Rudolf Hatz

Third supervisor: Prof. Dr. med. Claus Neurohr

Fourth supervisor: Prof. Dr. med. Andrea Koch

Dean: Prof. Dr. med. Thomas Gudermann

Datum der Verteidigung:

08.11.2022

Eidesstattliche Versicherung

Ich, Mircea-Gabriel Stoleriu, erkläre hiermit an Eides statt, dass ich die vorliegende Dissertation mit dem Thema:

„Secretory to multi-ciliated cell imbalance by altered cellular progeny in end-stage COPD facilitates resilience to environmental pollutants "

selbständig verfasst, mich außer der angegebenen keiner weiteren Hilfsmittel bedient und alle Erkenntnisse, die aus dem Schrifttum ganz oder annähernd übernommen sind, als solche kenntlich gemacht und nach ihrer Herkunft unter Bezeichnung der Fundstelle einzeln nachgewiesen habe. Ich erkläre des Weiteren, dass die hier vorgelegte Dissertation nicht in gleicher oder in ähnlicher Form bei einer anderen Stelle zur Erlangung eines akademischen Grades eingereicht wurde.

München-Gauting   Mircea-Gabriel Stoleriu

8.11.2022

_____   _____

Ort, Datum   Unterschrift

Summary

Background: Air pollution is a major risk factor for patients suffering from chronic respiratory conditions including chronic obstructive pulmonary disease (COPD), as it drives episodes of exacerbation and subsequently disease progression.

Analysis of the differentiation process of the primary human bronchial epithelial cells (pHBECs) from non-chronic lung disease (non-CLD) and CLD/ COPD-diseased tissue samples is of critical importance to understand the underlying pathophysiological mechanisms that characterize the disease specific response to air pollutant exposure at the first line of defense, i.e. the human bronchial epithelium. In addition, pHBECs culture contributes to potential identification of preventive and therapeutic strategies in CLD.

Materials and Methods: We established 3D air-liquid interface (ALI) cultures in pHBECs isolated from large airway resections of diseased (n=3 COPD-II and n=6 COPD-IV) and healthy (non-CLD, n=4) patients. To mimic air pollution, pHBECs were exposed to relevant aerosolized nanoparticles (NPs, i.e. carbon black soot surrogate NP (CNP) and Zinc oxide (ZnO)) using the pre-clinical, highly standardized VITROCELL® CLOUD 12 nebulization system (Waldkirch, Germany). ALI cultures, validated for their disease specific, biomimetic cellular composition using trans-mural bronchial punches (BP), were analyzed for functional consequences of NP exposure via transepithelial electrical resistance (TEER), WST-1, LDH, 3D confocal immunofluorescence (IF), transcriptome, secretome as well as ciliary beating frequencies (CBF) of multi-ciliated cells (MCC). To highlight the cell differentiation trajectory that explains the outlined cell composition and functional changes postexposure, single cell RNA-seq drop-seq analysis and immunofluorescence (IF) stainings of native bronchial tissue samples were performed.

Results: ZnO exposure induced effects on the amount of MCC and function exceeded the effects observed by CNP or LPS exposure. Exposure to moderate ZnO doses induced a decrease in the number of MCC in COPD-II ($20.35\pm14.07\%$) and COPD-IV pHBECs ($18.51\pm11.86\%$) when compared to non-CLD cells ($47.01\pm2.80\%$), as well as an elevated number of MUC5AC$^+$ cells in COPD-IV cultures ($12.75\pm2.90\%$) when compared to non-CLD cultures ($5.17\pm2.43\%$). These findings were accompanied by a concentration dependent reduction in epithelial barrier integrity (TEER), metabolic cell viability (WST-1) and membrane integrity (LDH release) in non-CLD and COPD-II pHBECs when compared to COPD-IV pHBECs. Following ZnO and CNP exposure, COPD-IV cultures were characterized by transcriptional regulation of genes involved in secretory cells (SC)-MCC differentiation axis (cilium assembly and organization), TLR-mediated innate immunity and regulation of extracellular matrix remodeling (ECM). Also at baseline level, transcriptome analysis revealed an overrepresentation of ECM gene clusters in COPD-IV cultures.

Cellular composition of pHBECs ALI cultures resembled the *ex vivo* picture achieved by culturing BPs at ALI. These findings highlight an oligo-ciliated hypersecretory phenotype in COPD-IV cultures, with a skewed basal cells (BC)-induced cell trajectory towards SC at the expense of the more vulnerable MCC. Terminal differentiation into MCC resulted from progenitor SC (MUC5AC$^+$, CC10$^+$).

The outlined phenotype was in line with an aberrant expression of MCC genes together with a pathologic CBF spectrum in COPD-IV cultures.

Drop-seq single cell RNA-seq analysis in both non-CLD and COPD-IV cultures on ALI day 0 and ALI day 28 revealed two distinct BC populations (basal_1, basal_2) as progenitor cells for the SC-MCC differentiation axis. BC present a strong shift between non-CLD and COPD-IV patients on both ALI day 0 and day 28. Specifically, basal_1 cells characterized the COPD-IV cultures, being predominantly detected on ALI day 0 and exclusively on ALI day 28 in COPD-IV derived pHBECs. Conversely, basal_2 cells characterized the non-CLD derived pHBECs on both ALI day 0 and 28. These signatures were validated by IF stainings of native bronchial tissue samples.

Conclusion. In summary, our results identify the predominance of SC in the large airways of patients suffering from COPD-IV resulting in a greater functional resilience of the pHBECs to environmental small particle exposure underlined by the unsuccessful drive to induce trans-differentiation of the SC cells into MCC.

Zusammenfassung:

Hintergrund: Luftverschmutzung ist der wichtigste Risikofaktor für Patienten mit chronischen obstruktiven Lungenerkrankung (COPD). Die chronische Nanopartikel (NP) Exposition führt zur wiederholten Exazerbationen und zu einem unvermeidbaren Fortschreiten der COPD Erkrankung.

Die Analyse des Differenzierungsprozesses der primären humanen Bronchialepithelzellen (pHBECs) von Patienten ohne chronische Lungenerkrankungen (non-chronic lung disease/ non-CLD) und mit chronischen Lungenerkrankungen (CLD/ e.g. COPD) ist von entscheidender Bedeutung, die pathophysiologischen Mechanismen des Bronchialepithels nach Luftverschmutzung zu charakterisieren sowie präventive und therapeutische Strategien für CLD zu etablieren.

Materialen und Methoden: Wir haben eine 3D Zellkultur an der Luft-Flüssigkeit-Grenzschicht (air liquid interface/ ALI) mit pHBECs aus den proximalen Hauptbronchien von COPD (n = 3 COPD-II und n = 6 COPD-IV) und gesunden (n = 4 non-CLD) Patienten etabliert. Um die Umweltverschmutzung *in vitro* zu simulieren, wurde eine Exposition der pHBECs mit relevanten aerosolierten NP (z.B. Carbon soot surrogate NP (CNP) und Zinkoxid (ZnO)) mit Hilfe eines standardisierten Expositionssystems (VITROCELL® CLOUD 12, Waldkirch, Germany) durchgeführt. Die Validierung von ALI-Zellkulturen und deren krankheitsspezifischen und biomimetischen Zellzusammensetzung erfolgte mit Hilfe eines neuen 3D Kulturmodells unter Verwendung von frischen nativen humanen Bronchialwand-Präparaten (bronchial punches/ BPs), die die intakte Struktur der gesamten Bronchialwand aufrechterhalten. Für die Validierung der 3D ALI pHBECs Kulturen erfolgte die Analyse des transepithelialen elektrischen Widerstands (TEER), der Zellviabilität (WST-1) und der Membranintegrität (LDH), sowie die 3D konfokale Immunfluoreszenz (IF), Transkriptom- , Sekretomanalyse, und die Analyse der Zilienschlagfrequenz (ciliary beating frequency/ CBF). Um die Änderungen der Zellzusammensetzung und der Epithelfunktion nach NP Exposition genauer zu analysieren, wurden eine single cell RNA-seq drop-seq Analyse und IF von nativen Bronchusgewebeproben ergänzend durchgeführt.

Ergebnisse:
Die ZnO-induzierte Effekte auf die Zilien-tragenden Zellen (multi-ciliated cells/ MCC) übertrafen die bei CNP- oder LPS-Exposition beobachteten Effekte. Die Exposition mit moderaten ZnO NP Dosierungen führte zu einer leichten Zahlabnahme der MCC in COPD-II (20,35 ± 14,07%) und COPD-IV pHBECs (18,51 ± 11,86%) im Vergleich zu non-CLD Zellen (47,01 ± 2,80%), sowie zu einer erhöhten Zahl von MUC5AC+ Zellen in COPD-IV Kulturen (12,75 ± 2,90%) im Vergleich zu non-CLD Zellen (5,17 ± 2,43%). Diese Befunde korrelieren mit einem konzentrationsabhängigen Verlust des transepithelialen elektrischen Widerstands (TEER), der Zellviabilität (WST-1) und der Membranintegrität (LDH-Freisetzung) in non-CLD und COPD-II im Vergleich zu COPD-IV pHBECs.
Die ZnO und CNP Exposition führte zu einer aberranten Überexpression von Zilien spezifischen Genen in den COPD-IV Kulturen. Die Transkriptomanalyse der COPD-IV Kulturen nach ZnO und CNP Exposition zeigte eine Aktivierung der Mukuszellen-MCC

Differenzierungsachse, der TLR-Immunität und der extrazellulären Matrix Biosyntese (extracellular matrix remodeling/ ECM). Des Weiteren bestätigen die unbehandelten COPD-IV Kulturen eine signifikante ECM Genexpression.

Darüber hinaus ähnelte die Zellzusammensetzung der pHBEC-ALI-Kulturen dem *ex vivo* Bild der BPs. Diese Ergebnisse demonstrieren einen „oligo-ciliated" hypersekretorischen Phänotyp der COPD-IV ALI Kulturen im Rahmen einer verzerrten, Basalzellen-induzierten Zelldifferenzierung in Richtung sekretorischen Zellen, auf Kosten der anfälligen MCC. Die sekretorischen Zellen (MUC5AC$^+$, CC10$^+$) sind Vorläuferzellen für MCC. Dieser Phänotyp stimmte mit einer aberranten MCC Genexpression sowie einem pathologischen CBF Spektrum in COPD-IV Kulturen überein.

Die drop-seq single cell Analyse bei non-CLD und COPD-IV Patienten zeigt zwei unterschiedliche Basalzellpopulationen (basal_1, basal_2) am ALI Tag 0 und 28. Die basal_1 Zellen sind überwiegend am Tag 0 und ausschließlich am Tag 28 in COPD-IV Kulturen identifizierbar. Die basal_2 Zellen charakterisieren die non-CLD-Kulturen sowohl am Tag 0 als auch am Tag 28. Die single cell Signaturen wurden durch IF Färbungen validiert.

Schlussfolgerung: Der hypersekretorische Phänotyp der COPD-IV ALI Kulturen führt zu einer größeren funktionellen Widerstandsfähigkeit des Bronchialepithels nach NP Exposition und resultiert aus einer erfolglosen Transdifferenzierung der sekretorischen Zellen in MCC.

List of figures

List of tables

List of abbreviations

A

Ac.-Tub[+]	Acetylated Tubulin
AECOPD	Acute exacerbation of chronic obstructive pulmonary disease
Al	Aluminium
ALI	Air liquid interface
ALId7	Air liquid interface day 7
AM	Alveolar macrophages
AT1/ 2	Alveolar type 1/ 2 cells
α-1 AT	Alpha -1 antitrypsin
As[-]	Arsenic

B

BC	Basal cells
BET	Mass-specific surface area of NPs according to Brunauer et al.[7]
BH	Benjamini-Hochberg Test
BP	Bronchial punches
BSA	Bovine serum albumin
BOLD	Burden of obstructive lung disease (study)

C

Ca	Calcium
CBF	Ciliary beating frequency
CC10[+]	Club cells specific protein 10[+]
Cd	Cadmium
Cr	Chromium
CLD	Chronic lung disease
CMV	Cytomegalovirus
CNP	Carbon (black soot surrogate) nanoparticle
CNTROB	Centrobin
COPD	Chronic obstructive pulmonary disease
CPC	Comprehensive Pneumology Center
CSE	Cigarette smoke extract
CT	Computer tomography
Cu	Copper

D

DAPI[+]	4,6-diamidino-2-phenylindole[+]
DABG	Background of the gene datasets
DEG	Differentially expressed genes

DC1, 2   Diffusion map embeddings 1, 2

DC   Dendritic cells

DLS   Dynamic light scattering

E

ECM   Extracellular matrix

EMT   Epithelial-to-mesenchymal transition

ESCAPE   European Study of Cohorts for Air Pollution Effects

F

FC   Fold change

FCS   Fetal calf serum

FDR   False discovery rate

FEV_1 Forced expiratory volume in one second

$FOXJ1^+$ Forkhead/ winked helix transcription factor J1$^+$

FVC   Forced vital capacity

G

GC   Goblet cells

GHO   Global Health Observatory

GO   Gene ontology

GOLD   Global Initiative for chronic obstructive lung disease

GPX   Glutathione peroxidase

H

HBSS   Hanks' balanced salt solution

huAEC   Human airway epithelial cells

HMOX   Haem oxygenase

I

IARC   International Agency for Research on Cancer

ICS   Inhalative corticosteroids

IF   Immunofluorescence

IPA®   Ingenuity Pathway Analysis®

K

KRT   Keratin

L

LAMB3   Laminin-β3

LDH	Lactate dehydrogenase
LPS	Lipopolysaccharyde
LSM	Laser Scanning Microscope
LTX	Lung transplantation

M

MCC	Multi-ciliated cells
Mg	Magnesium
MT1IH	Metallothionein1IH
MUC5AC$^+$	Mucin5AC$^+$
MUC5B$^+$	Mucin5B$^+$
Mn	Manganese

N

non-CLD	Non chronic lung disease
NHBE	Normal human bronchial epithelial cells
NP	Nanoparticle
NP conc	Nanoparticle concentration

O

OS	Oxidative stress

P

PAH	Pulmonary artery hypertension
pCO$_2$	Partial pressure of CO_2
pO$_2$	Partial pressure of O_2
Pb	Lead
PBS	Phosphate buffer saline
pHBECs	Primary human bronchial epithelial cells
PM	Particulate matter
PM$_{10}$	Particulate matter with a diameter between 10 and 2.5 μm
PM$_{2.5}$	Particulate matter with a diameter between 2.5 and 0.1 μm
PM$_{0.1}$	Particulate matter with a diameter ≤ 0.1 μm
PTEN	Phosphatase and tensin homolog

Q

QCM	Quartz crystal microbalance

S

sBC	Suprabasal cells

SC	Secretory cells
SC-MCC	Secretory-multi-ciliated cells differentiation axis
SCB1A1	Secretoglobulin 1A1
SD	Standard deviation
SEM	Standard error of mean
SOD	Superoxide dismutase
Sp-A	Surfactant protein-A
SW/MWCNT	Single-walled/ multi-walled carbon nanotubes

T

TAC	Transcriptome Analysis Console
TEER	Transepithelial electrical resistance
Ti	Titanium
TP63^{+}	Transcription factor protein 63^{+}
TNF-α	Tumor necrosis factor-α

U

UMAP	Uniform Manifold Approximation and Projection

W

WHO	World Health Organization

Z

ZnO	Zinc oxide

1. Introduction

1.1 Air pollution

1.1.1 Impact of air pollution on the environment and human health

Air pollution is one of the most important environmental risk factors that contributes to the development and progression of various respiratory and cardiovascular diseases, thus causing a major medical burden [8–13]. Epidemiological studies demonstrated air pollution to be responsible for increased morbidity and for up to 7 million premature deaths worldwide[14]. Environmental pollutants play a crucial role in the development of various malignancies including lung cancer, pleural mesothelioma, breast cancer, bladder cancer, leukemia and malignant melanoma [15,16].

Because of high industrialization and urbanization processes, the air pollution-associated multimorbidity and subsequent premature mortality are expected to increase in the next decades. According to the Global Health Observatory (GHO) data (2015), provided by the World health organization (WHO), environmental toxin exposure was associated with 26% deaths after respiratory infections, 25% of deaths related to chronic obstructive pulmonary disease (COPD), 17% cardiovascular and neurologic deaths and 16% deaths in lung cancer patients. Reduction of environmental toxin exposure could prevent approximately 125 000 deaths/ year in European cities [17].

The Health Effects Institute classified the global deaths in accordance with the trigger (environmental particulate matter/ PM with a diameter between 0.1-2.5 μm or household pollution), as shown in **Table 1**.

Disease	Global Mortality	
	Particulate matter PM$_{2.5}$	**Household Air Pollution**
Ischemic heart disease	17%	8%
Lung cancer	16%	9%
Chronic obstructive pulmonary disease (COPD)	27%	20%
Cerebrovascular disease (stroke)	14%	9%
Lower respiratory infections	28%	26%

Table 1: Classification of air pollutants-related global mortality according to the Health Effects Institute with focus on the top 5 air pollutants-related diseases (https://www.stateofglobalair.org/sites/default/files/soga-2018-report.pdf). PM$_{2.5}$ particulate matter with a diameter between 0.1-2.5 μm.

Because of its large surface contact area, the respiratory tract is affected by environmental pollution. Several diseases including acute and chronic respiratory infections, COPD, interstitial lung diseases (e.g. idiopathic pulmonary fibrosis) and lung cancer are shown to be directly triggered by air pollutants [18,19]. In particular, air pollution contributes not only to the development, but also to the acute exacerbation of COPD (AECOPD). Basically, AECOPD episodes are caused in 88% of all cases by viral (Rhinoviruses, Influenza) or bacterial (Gram-positive: *Haemophilus influenzae, Streptococcus pneumonie* and Gram-negative *Enterobacter, Pseudomonas aeruginosa*) pathogens [20]. Of critical importance in the pathogenesis of AECOPD is the active and repetitive exposure to cigarette smoke (CS) or environmental air pollutants. Interestingly, it has been demonstrated that exposure to air pollutants not only increases the number of the AECOPD episodes, but also gradually decreases the lung function parameters (forced expiratory volume in one second/ FEV_1) by ca 40 ml each year[21,22].

In order to better understand the pathomechanisms of air pollution-induced AECOPD and to avoid the onset of new exacerbations that contribute to a gradual decline of lung function, it is mandatory to characterize the pathogenic effect upon environmental toxins exposure on bronchial epithelium. Accordingly, air pollutants are classified by composition, size, mechanism of action, bioavailability and permeability.

1.1.2 Classification and characterization of air pollutants

Air pollutants are classified according to their size in small/ coarse particles (particulate matter/ PM) with diameters between 2.5-10 μm (PM_{10}), fine nanoparticles (NPs) with diameters between 0.1-2.5 μm ($PM_{2.5}$) and ultrafine NPs with a diameter under 0.1 μm ($PM_{0.1}$).

Sources of particulate matter are summarized in **Table 2**.

Features	PM_{10}	$PM_{2.5}$	$PM_{0.1}$
Nomenclature	Small, inhalable, coarse NPs	Fine NPs	Ultrafine NPs
Particle size	2.5-10 μm	0.1-2.5 μm	< 0.1 μm
Consistency	solid or liquid	solid or liquid	solid or liquid
Sources			
Organic compounds	-Coal dust -Coal fly ash -Dirt from factories, farming and roads	-Settling dust -Coal fly ash -Oil smoke -Smog	-Suspended atmospheric dust -Smog, soot -Metal fumes -Seasalt nuclei

	-Crushing and grinding rocks and soil	-Toxic organic compounds -Heavy metal -Fire/ metal processing products	-Tobacco smoke -Diesel exhaust -Manufactured nanoparticles
Allergens	-Pollen -House dust mite -Animal allergens	-House dust mite -Animal allergens	
Infectious compounds	-Bacteria -Mold spores	-Bacteria	-Viruses
Examples of ambient PM	Iron, Calcium, Silicon, Sodium, Chrlorine, Aluminium	Sulphate, nitrate, Ammonium, Cadmium, organic Carbon, Gases: Sulphur/ Nitrogen dioxide, volatile organic compounds	

Table 2: Characterization of atmospheric particulate matter (PM) by size (PM_{10}, $PM_{2.5}$, $PM_{0.1}$), consistency and environmental distribution

As presented in **Table 2**, PM_{10}, $PM_{2.5}$ and $PM_{0.1}$ are organic, allergenic or infectious compounds, which originate in coal, petrol, diesel or chemical power stations as a result of hyper-industrialization and uncontrolled combustion processes in heavily urbanized cities.

Since our work aimed to analyze the cell composition and epithelial function of the NP exposed human bronchial epithelium, it is important to understand the source of air pollution and the main processes that cause PM production.

According to the *Canadian working group* (https://www.canada.ca/en/health-canada/services/environmental-workplace-health.html), the main sources of PM are industrial (chemicals- or dyes- manufacture, coal gasification, distillation, incineration, fuel production, tobacco industry, surface coatings, pesticides and fertilizer application) or non-industrial (transportation, welding fume and cigarette smoke).

Due to their detrimental short- and long-term effects for human health, PM are classified by *The International Agency for Research on Cancer* (IARC) as Group 1 human carcinogenic substances. Based on a PM exposure threshold of 10 μg/m^3 used by the *European Study of Cohorts for Air Pollution Effects* (ESCAPE), $PM_{2.5}$ and PM_{10} were associated with a relative risk of 1.09 and 1.07 for developing lung cancer, respectively [23].

1.1.3 Classification of nanoparticles (NP) mimicking air pollution

In order to mimic air pollution and to analyze the effects on the respiratory system, many studies focused on natural or manufactured PM (PM_{10}, $PM_{2.5}$, $PM_{0.1}$) and their application in different *in vitro* or *ex vivo* culture models.

For the study of PM_{10}, airborne pollutants have to be sampled via high-volume particle collectors from different commercial or industrial areas in highly industrialized and urbanized cities. Representative examples for PM_{10} are endotoxins, carbon-based or heavy metal-based (Arsenic/ As, Cadmium/ Cd, Chromium/ Cr, Copper/ Cu, Manganese /Mn, Nickel/Ni, Lead/ Pb and Zinc/ Zn) particles.

After collection and filter deposition, PM_{10} can be nebulized on lung epithelium[24,25] for the study of inflammatory and cytotoxic effects on human bronchial epithelial cells. Comparable effects at air liquid interface (ALI) cell cultures were also reported upon exposure to agricultural organic PM_{10} from dairy parlor dust [26,27].

Representative $PM_{2.5}$ are carbon-based (carbon soot surrogate NPs/ CNP/ Printex90) or metal-based (Aluminum/ Al, Calcium/ Ca, Sodium/ Na, Iron/ Fe, Copper/ Cu, Titanium/ Ti, Zinc/ Zn, Manganese/ Mn, Vanadium/ Vn, **Table 3**).

PM size	PM composition	Representative examples of PM used *in vitro*
PM_{10}	Carbon-based	SWCNT, MWCNT
	Heavy metals	As, Cd, Cr, Cu, Mn, Ni, Pb, Zn
	Endotoxins	LPS
$PM_{2.5}$	Carbon-based	Carbon NPs (CNP)/ Printex90, SWCNT, MWCNT
	Heavy metals	Al, Ca, Na, Fe, Cu, Ti, Zn, Mn, Vn
	Endotoxins	LPS

Table 3: Classification of the particulate matter (PM) used *in vitro*, based on the PM size (> 2.5 μm or < 2.5 μm), source and composition. NP - nanoparticle, CNP - carbon nanoparticles, NT - nanotubes, SWCNT - single-walled carbon nanotubes, MWCNT - multi-walled carbon nanotubes

Similar to PM_{10}, $PM_{2.5}$ exposure models were used for the study of cytotoxic, proinflammatory and oxidative stress (OS) responses provoked at the level of human bronchial epithelium [28,29].

1.1.4 Mechanisms of action of particulate matter (PM) on the respiratory tract

The size, distribution and solubility of PM are determinant factors for the progression of respiratory diseases including COPD and AECOPD.

Accordingly, the PM size dictates particular defense mechanisms at the level of human bronchial epithelium:

i) PM_{10}:

PM$_{10}$ enter the nasal cavity, deposit at the level of the upper respiratory tract (larynx, trachea and main bronchi), accumulate temporarily into the thick mucus film and are eliminated via the muco-ciliary escalator.

ii) $PM_{2.5}$

PM$_{2.5}$ cannot be removed via muco-ciliary escalator. PM$_{2.5}$, are transported to the terminal bronchioles and alveolar epithelium, interact with the surfactant proteins (SP-A and D) and are presented to the resident cells of the alveolar epithelium (alveolar type 1/ AT1, alveolar type 2/ AT2 cells, alveolar macrophages/ AM and alveolar dendritic cells/ DC). At these levels, PM$_{2.5}$ induce inflammatory (Tumor necrosis factor-α/ TNF-α, IL-1β) and OS (glutathione peroxidase/ GPX3, Metallothionein/ MT2A, haem oxgenase/ HMOX, superoxide dismutase/ SOD) responses. While PM$_{2.5}$ are partially cleared via AM and DC by phagocytosis, residual PM$_{2.5}$ reach the bloodstream by paracellular translocation through AT1- or endothelial cells-induced transcytosis [30].

iii) $PM_{0.1}$

PM$_{0.1}$ easily enter the conductive bronchi, accumulate in the respiratory bronchioles and alveoli, and translocate into the bloodstream, leading to local as well as systemic inflammatory and OS responses.

Mechanistically, both PM$_{2.5}$ and PM$_{0.1}$ are immersed in the mucus film and can only be partially removed from the bronchi via the muco-ciliary escalator. The remaining PM are enclaved in the mucus film and subsequently attracted in the cytosol via hydrophobic and electrostatic interactions guided by the vesicles secreted by the goblet cells [31]. Simultaneously, the tight junctions facilitate PM absorption due to their immunologic intercellular barrier and selective bidirectional permeability for vesicles and ions [31,32].

The PM-triggered mechanisms on the respiratory tract are presented in **Figure 1**.
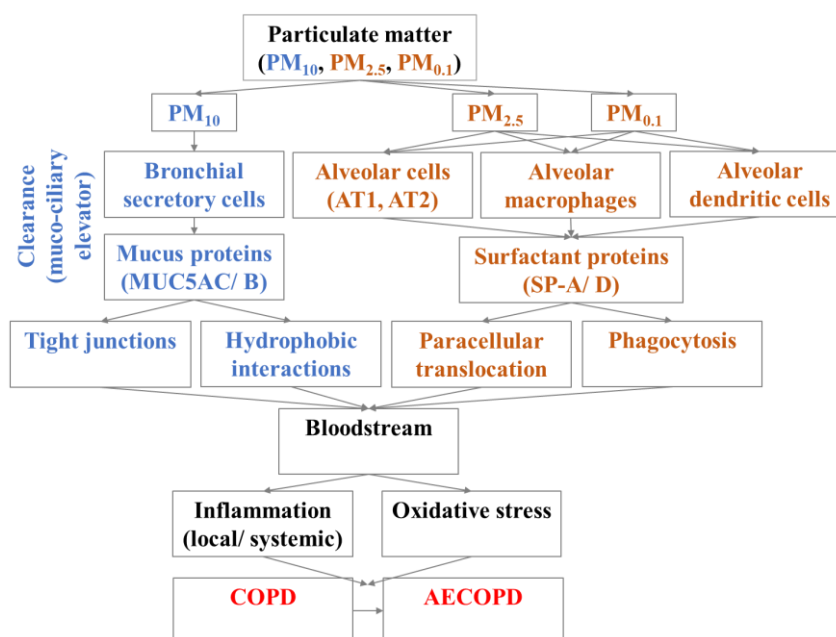
Figure 1: Particulate matter (PM)-triggered mechanisms at the level of the human bronchial epithelium: i) small PM (PM$_{10}$) are partially cleared via muco-ciliary escalator or translocated into the bloodstream, ii) fine PM (PM$_{2.5}$) are partially cleared by muco-ciliary escalator, or presented to the antigen presenting cells following phagocytosis or hematogenous translocation, iii) ultrafine PM (PM$_{0.1}$) reach the distal airway epithelium where they are presented and ingested by the antigen presenting cells. PM induce local effects by facilitating an acute COPD exacerbation (AECOPD) or systemic effects with consecutive extrapulmonal manifestations upon hematogenous translocation.

1.1.5 Classification of diseases triggered by environmental pollutants

Air pollutants are considered major environmental risk factors that play a crucial role in development, progression and exacerbation of many diseases, thus increasing morbidity, and premature mortality, leading to important medical and socio-economic consequences[17,33]. Therefore, the impact of air pollutants on human health is of crucial importance.

Of note, a healthy respiratory system promptly counteracts effects upon toxin inhalation when an efficient removal of environmental pollutants by intact barriers (e.g. bronchial epithelium, skin) is warranted. However, repeated long-term or even short-term toxin exposure can affect many organs and produce severe diseases[34–37].

The most frequent diseases triggered by outdoor and indoor pollutants classified by the WHO are illustrated in **Table 4**.

Disease	Source of air pollution	
	Outdoor air pollution	**Indoor air pollution**
Ischemic heart disease	40%	26%
Lung cancer	6%	6%
Chronic obstructive pulmonary disease (COPD)	11%	22%
Cerebrovascular disease (stroke)	40%	34%
Lower respiratory infections in children	3%	12%

Table 4: WHO classification of air pollutants-related major diseases. Percentages illustrate the disease incidence classified by indoor or outdoor air pollution source (https://en.wikipedia.org/wiki/List_of_pollution-related_diseases).

The mechanisms of disease development upon PM inhalation include both local (e.g. inflammation, mucus hypersecretion and fibrotic remodeling), as well as systemic effects upon activation of proinflammatory cytokines (e.g. IL-6, IL-1β, INF-γ, TNF-α) or acute phase proteins (e.g. CRP, SAA)[38].

While the intact respiratory system partially counteracts PM absorption and translocation, the altered respiratory system might further contribute to the development of severe diseases due to an inefficient muco-ciliary escalator, secretory cell hyperplasia or epithelial cell metaplasia [38,39].

Specifically, PM accumulation secondary to an inefficient clearance might facilitate a hematogenous translocation into different organs, leading to a PM-induced multiorgan dysfunction that could affect all systems of the body (e.g. respiratory[34,35], cardiovascular[36], cerebral[37], gastro-intestinal[40], urogenital[41], osteo-articular[42] and blood[43]).

1.2 Chronic Obstructive Pulmonary Disease (COPD)

Air pollution is one of the major risk factors that facilitates disease development and progression in patients suffering from chronic lung diseases (CLD), a disease family including COPD, asthma bronchiale, interstitial lung diseases, pulmonary hypertension, cystic fibrosis, chronic pneumonias and lung cancer [44–46]. These conditions are characterized by progressive and irreversible loss of pulmonary parenchyma with subsequent reduction of lung function, clinically translated in dyspnea, chronic cough and predisposition to pulmonary infections.

In particular in COPD, environmental pollutants trigger episodes of acute exacerbation (AECOPD) and subsequently lead to disease progression [47,48]. Unfortunately, COPD is a progressive, and only partially reversible disease[39] that cannot be causally treated. Lung transplantation, the gold standard in the treatment of end-stage lung diseases, prolongs the survival of these patients with 5.8 years in median [49].

Based on these considerations, it is of crucial importance to understand the pathophysiology of the affected tissue (i.e. primary human bronchial epithelium), as well as the underlying mechanisms that characterize the disease specific response to air pollutant exposure. This insight can inform the development of novel preventive and therapeutic strategies.

1.2.1 Epidemiology of COPD

COPD represents the fourth cause of mortality worldwide, with 3.2 million deaths representing 5% of all deaths globally (WHO report 2015). Due to its alarmingly increasing prevalence, it was estimated that COPD-related deaths will also continuously increase (ca. 4.6 million predicted deaths in 2030). Thus, it was estimated that COPD will become in 2030 the third leading cause of death worldwide after ischemic cardiovascular and cerebrovascular diseases.

Interestingly, more than 90% of the COPD-related deaths worldwide are reported in low and middle-income countries as a result of long-term exposure to environmental pollution or cigarette smoke.

Epidemiological studies in Germany reported 6.8 million COPD diseased people in 2010. According to WHO estimates, COPD prevalence is expected to continuously increase in Germany until 2030, by 7.9 million patients. According to the BOLD Study, COPD affects 13% of the people older than 40 years in Germany [50].

Of note, in 90% of the cases, COPD is caused by cigarette smoke followed by environmental indoor or outdoor toxin exposure. WHO reported in 2012 ca 3.7 million deaths and 2 million premature deaths worldwide as being related to the environmental air pollution [45]. Among all air pollutants, $PM_{2.5}$, PM_{10}, carbon monoxide, nitrogen dioxide, sulfur dioxide and ozone were causally related to COPD progression [51].

Given the direct causality between air pollution and COPD progression and the increasing pollution-related COPD mortality worldwide, a better understanding of the role of the environmental toxins at the level of bronchial epithelium is required.

1.2.2   Diagnosis of COPD

The diagnosis of COPD is based on medical history and clinical investigations.

Medical history reveals progressive and repetitive episodes of chronic productive cough, dyspnea, wheezing and chest tightness, especially during physical activities. More than 50% of the patients older than 40 years, presenting these symptoms are diagnosed with COPD. Of note, smoking history is positive in ca. 90% of COPD patients.

The clinical investigations include lung function tests (spirometry), blood gas analysis, laboratory tests, microbiological culture of the sputum, chest X-ray, CT scan and bronchoscopy (**Table 5**).

Diagnostic test	Parameters	Findings
Lung function	Forced expiratory volume 1s (FEV_1) Forced vital capacity (FVC)	FEV_1 < 80% FVC < 80%
Blood gas analysis	pO_2 pCO_2	pO_2 < 60 mmHg pCO_2 > 40 mmHg
Laboratory tests	α-1 antitrypsin (α-1 AT) IgA	α-1 AT < 80 mg/dl IgA < 7 mg/dl
Sputum culture	Bacterial culture	e.g. Haemophyilus influenzae (40%), Streptococcus pneumonie (15%), Moraxella catharrhalis (15%)
Chest X-ray/ CT scan	Broncho-alveolar tree Ribs/ diaphragm orientation	-Overinflation -Flattened intercostal spaces and hemidiaphragms
Bronchoscopy	Histopathological examination	-Chronic inflammation -↑ mucus production -Goblet cell hyperplasia -Peribronchial fibrosis

Table 5: Description of clinical investigations used in COPD diagnosis with specification of main findings for each diagnostic test

1.2.3 Classification of COPD

The parameters assessed for COPD classification are clinical severity, number of yearly exacerbations and FEV_1 decrease. The actual COPD classification proposed by the Global Initiative for chronic obstructive lung disease (GOLD) is mainly based on clinical severity (**Table 6**) [52].

Patient group	GOLD stage	Severity of the dyspnea	Risk profile	No. exacerbations/ year
A	GOLD 1-2	extreme physical activity	Low risk	≤1
B	GOLD 1-2	moderate physical activity	Low risk	≤1
C	GOLD 3-4	extreme physical activity	High risk	≥2
D	GOLD 3-4	moderate physical activity	High risk	≥2

Table 6: COPD classification elaborated by Global Initiative for chronic obstructive lung disease (GOLD) based on clinical severity (dyspnea upon physical activity and number of exacerbations/ year)

The clinical severity is directly linked to the histological changes of the bronchial epithelium (severity of bronchial obstruction) as well as the proportional decrease in FEV_1 (**Table 7**) [52,53].

GOLD stage	Severity of the airway obstruction	Predicted FEV_1
GOLD 1	Mild	≥ 80%
GOLD 2	Moderate	50-79%
GOLD 3	Severe	50-30%
GOLD 4	Very severe	<30%

Table 7: COPD classification elaborated by Global Initiative for chronic obstructive lung disease (GOLD) based on severity of the obstruction and percentual decrease in lung function. FEV_1- forced expiratory lung volume in 1 second.

1.2.4 Therapy guidelines in COPD

Since COPD is a progressive and irreversible CLD, the treatment strategies are focused on amelioration of COPD symptoms, decrease of yearly exacerbations, reduction of airway obstruction and optimization of lung function. In all COPD stages prevention and medication are necessary [54]. Preventive strategies (e.g. avoiding air pollution and cigarette smoke cessation) play a beneficial role in amelioration of the symptoms and counteract disease progression [55–57]. The medical treatment is stage-dependent and aims the reduction of the bronchial obstruction and inflammation by bronchodilators, sympathomimetic and anti-inflammatory agents.

According to the clinical severity and histopathological changes at the level of the human bronchial epithelium, COPD treatment is based on one or more inhalative bronchodilators (stage A→D), together with inhalative (stage A→D) or systemic corticosteroids (stage D) and long-term oxygen therapy (stage D). Inhalative drugs have reduced off-target effects (when compared to the systemic therapy) because of their efficient deposition and increased bioavailability at the level of the airways [58–60]. In particular in lung emphysema, endoscopic or surgical lung volume reduction might be considered as treatment option in selected cases. In end-stage COPD, lung transplantation represents the gold standard.

1.2.5 COPD pathogenesis

There are two distinct forms of COPD: chronic bronchitis and lung emphysema. Accordingly, the pathogenesis of these diseases is associated to:

- i) a chronic toxin exposure (air pollutants, cigarette smoke) inducing airway obstruction and tissue remodeling in chronic bronchitis
- ii) a genetic deficiency (α-1 antitrypsin) as cause for the airway destruction in lung emphysema

In both forms, disease progression might be triggered by active or passive cigarette smoke exposure as well as environmental indoor or outdoor air pollution.

Chronic bronchitis is characterized by bronchial wall thickening, peribronchial fibrosis and mucus hypersecretion, clinically reflected in chronic productive cough, dyspnea and progressive decline of lung function. Pathomechanistically, inhaled toxins induce a chronic airway inflammation with subsequent accumulation of inflammatory cells at the level of central and peripheral lung airways. Because of the mucus hypersecretion and inefficient muco-ciliary clearance, accumulated toxins are only partially cleared by resident macrophages and lymphocytes (B, NK). Particles that cannot be efficiently cleared, translocate in the bloodstream and induce local and systemic inflammatory responses [61–63]. The chronic local inflammation involves the resident cells of the bronchial epithelium (e.g. bronchial epithelial cells, fibroblasts, eosinophils, lymphocytes, neutrophils and macrophages, **Table 8**) that enhance host defense mechanisms by secreting proinflammatory and profibrotic cytokines and facilitate oxidative stress responses.

Cell types	Marker genes	Effects
Bronchial epithelial cells	TGF-β, TGF-β1, FGF, IL-8, ROS, TNF-α	-Bronchial wall thickening -Peribronchial fibrosis -Epithelial-to-mesenchymal transition (EMT) -Alveolar wall destruction
Fibroblasts	TGF-β, FGF	
Eosinophils	IgE	
Th17/ Tc17 cells	IL-22, IL-17A	-Alveolar wall destruction

Th1, Tc1 cells	INF-γ, perforin, granzyme B	
B lymphocytes	IgG, IgE	
NK-cells	Perforin, granzyme B	
Dendritic cells/ naive CD4$^+$ or CD8$^+$ T-cells	IL23, IL1B, IL6, CXCL9/ 10/ 11	-Cell apoptosis -Tissue remodeling
Neutrophils	CXCL8, G-CSF, proteases	-Alveolar wall destruction -Mucus hypersecretion

Table 8: Characterization of cell subpopulations involved in COPD pathogenesis with focus on the proinflammatory and profibrotic cytokines and histopathological effects at the level of bronchial epithelium (source modified after https://www.ncbi.nlm.nih.gov/core/lw/2.0/html/tileshop_pmc/tileshop_pmc_inline.html?title=Click on image to zoom&p=PMC3&id=6831915_jtd-11-S17-S2129-f2.jpg).

The pathomechanisms of chronic bronchitis are illustrated in **Figure 2**.
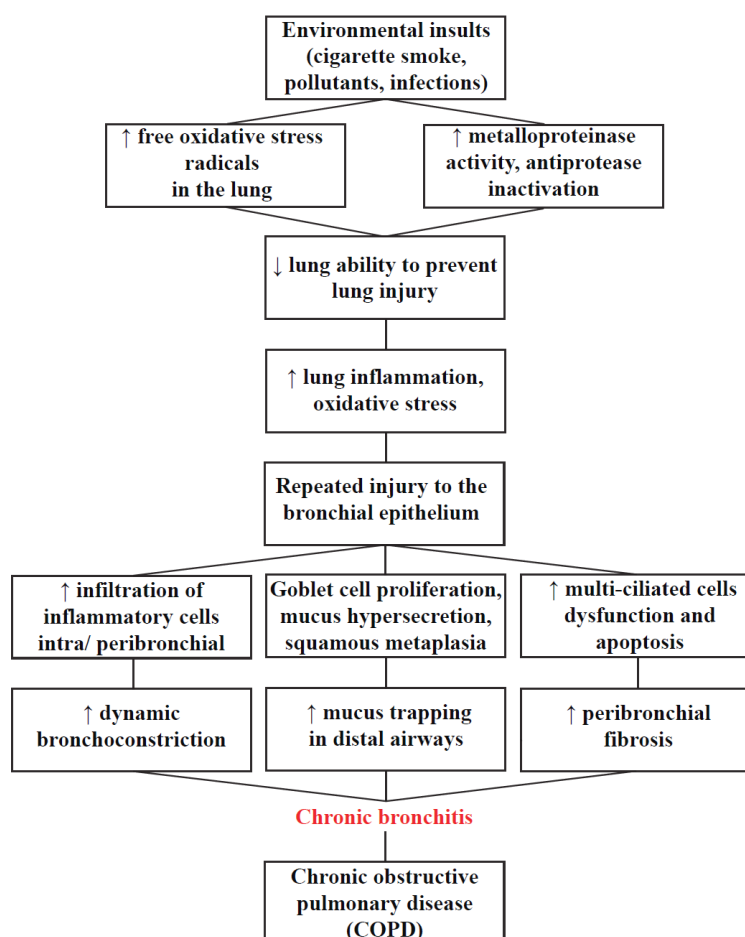
Figure 2: Pathogenesis of chronic bronchitis: upon environmental injury, increased oxidative stress-, protease-antiprotease imbalance and inflammatory responses lead to intrabronchial accumulation of inflammatory cells, goblet cell hyperplasia and multi-ciliated cells dysfunction. These changes facilitate progressive bronchoconstriction, intrabronchial mucus accumulation and peribronchial fibrosis as main findings for chronic bronchitis.

Lung emphysema is characterized by alveolar destruction and impaired alveolar distensibility, clinically reflected in chronic cough and dyspnea. These changes appear as result of an imbalance between proteases and anti-proteases activity (e.g. α-1 antitrypsin deficiency) that alters the physiological composition of the connective tissue of the lung airways. Subsequently, the inhaled air containing environmental pollutants accumulates in the damaged alveolar sacks and cannot be efficiently exhaled.

The pathomechanisms of lung emphysema are illustrated in **Figure 3**.
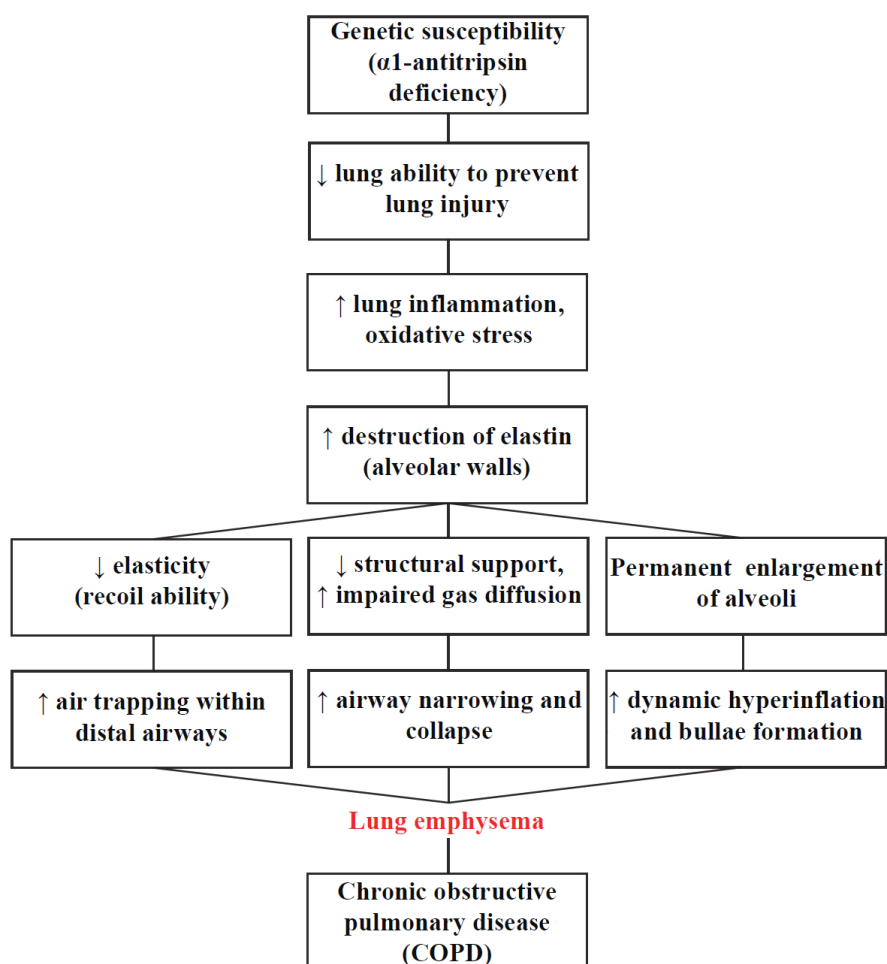
Figure 3: Pathogenesis of lung emphysema: genetic α1-antitrypsin deficiency leads to an imbalance between proteases and antiproteases activity with consecutive inflammation, oxidative stress and progressive destruction of alveolar walls. These changes facilitate a permanent enlargement of distal airways (bullae) and an increased air trapping with consecutive impaired gas diffusion.

Taken together, environmental toxins lead not only to mucus hypersecretion, bronchial obstruction, peribronchial fibrosis and tissue remodeling (changes observed in chronic bronchitis), but also to pathological enlargement and destruction of functional airways (changes observed in lung emphysema).

These morpho-functional changes lead ultimately to increased vulnerability to infections, impaired gas exchange and progressive decline of lung function (ca. 40 ml FEV_1 loss/year)[21,22].

Since bronchial epithelium continuously adapts to the chronic toxin exposure, early and late changes could be observed during COPD disease progression (**Table 9**).

Disease	Timeframe	Histopathological changes
Chronic bronchitis	Early changes	-Submucosal gland hypertrophy in distal trachea -Mucus hypersecretion -Minimal or absent inflammatory infiltrates
	Late changes	-Hyperplasia of basal cells and secretory cells -Increased amount of secretory cells and submucosal glands -Loss of multi-ciliated cells, reduction in cilia length -Cellular dysplasia and squamous metaplasia (transformation of bronchial cells intro squamous cells) -Obstruction of bronchi -Increased inflammatory infiltrates based on CD8$^+$ lymphocytes, neutrophils and macrophages
Lung emphysema	Early changes	-Enlargement of the respiratory bronchioles and alveoli -Thickness reduction of the bronchiolar wall -Inflammatory infiltrates with consecutive obliteration of bronchioles
	Late changes	-Apoptosis of the resident broncho-alveolar cells, AT1, AT2 and endothelial cells -Enlargement and destruction of respiratory bronchioles -Reduction of the elasticity of the bronchiolar wall due to the imbalance between proteases and anti-proteases -Accumulation of mucus and inflammatory infiltrates with consecutive intraluminal obstruction

Table 9: Description of early and late histopathological changes of the bronchial epithelium in chronic bronchitis and lung emphysema

The main cells affected by toxin exposure (**Table 8**) are the human primary bronchial epithelial cells (pHBECs). Under physiological conditions pHBECs give rise to secretory and multi-ciliated cells that build up the muco-ciliary escalator - the main barrier against environmental pollutants. Preliminary studies argued that chronic toxin exposure leads to an altered regeneration potential of the pHBECs, in comparison to the healthy unexposed

pHBECs [64]. Our study aims to analyze the differentiation potential of the healthy and diseased pHBECs upon NP exposure. To address this knowledge gap, we performed a comprehensive multi-omics analysis of human bronchial epithelium upon NP exposure, aiming for a better understanding of the factors that trigger disease progression and a potential identification of new therapeutic targets.

1.3   Human Bronchial Epithelium

1.3.1   Characterization of the cell subtypes of the main bronchi

The respiratory system continuously allows the entrance of environmental pollutants at the level of proximal bronchial epithelium. Only small particles can be partially cleared in the upper respiratory system, whereas fine or ultrafine NP are transported in the lower respiratory system, where they accumulate and translocate into the bloodstream.

The architecture of the airway epithelium varies at different levels in order to face chronic environmental challenges. Distal trachea and main bronchi present a pseudostratified epithelium, terminal bronchioles a columnar epithelium, bronchoalveolar regions a cuboidal epithelium and alveolar sacks a squamous epithelium.

The cell composition of the human bronchial epithelium is illustrated in **Figure 4**.
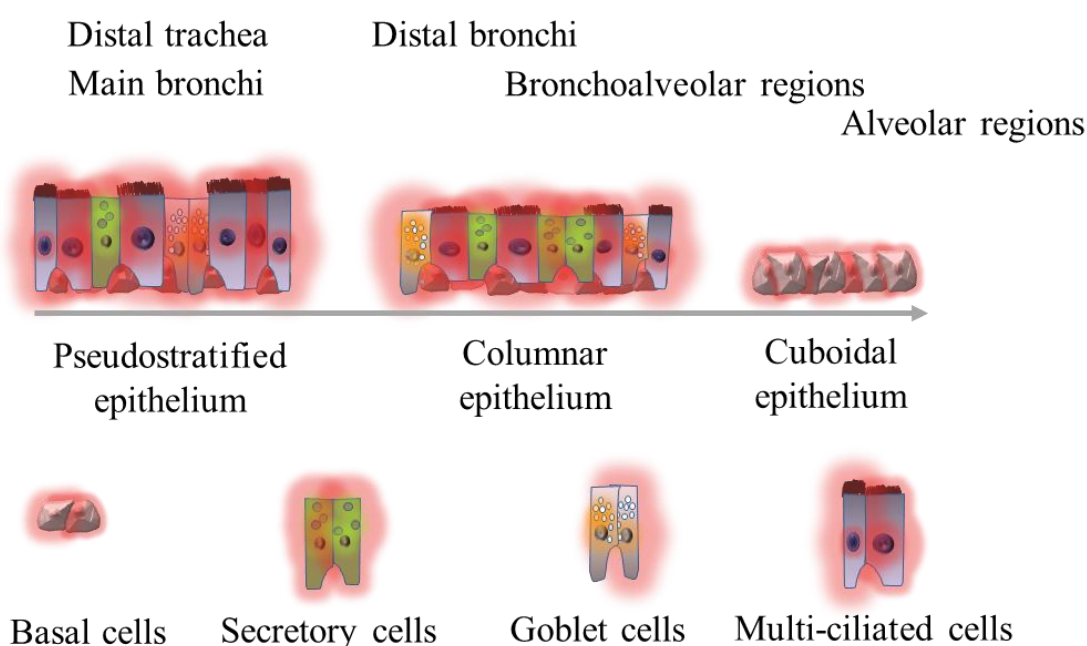
Figure 4: Schematic representation of the compositional differences at different levels of the human bronchial epithelium. Distal trachea and main bronchi present a pseudostratified epithelium, terminal bronchioles a columnar epithelium and bronchoalveolar regions a cuboidal epithelium.

Accordingly, airway epithelium is specialized for muco-ciliary clearance in the conductive airways (distal trachea, proximal bronchi) and gas exchange in the distal respiratory airways (respiratory bronchioles, alveoli).

Histologically, there are three major cell types at the level of the human bronchial epithelium: basal cells, secretory cells and multi-ciliated cells.

The developmental trajectory of these cell types, based on the human lung cell hierarchy atlas [1,2] is illustrated in **Figure 5**.
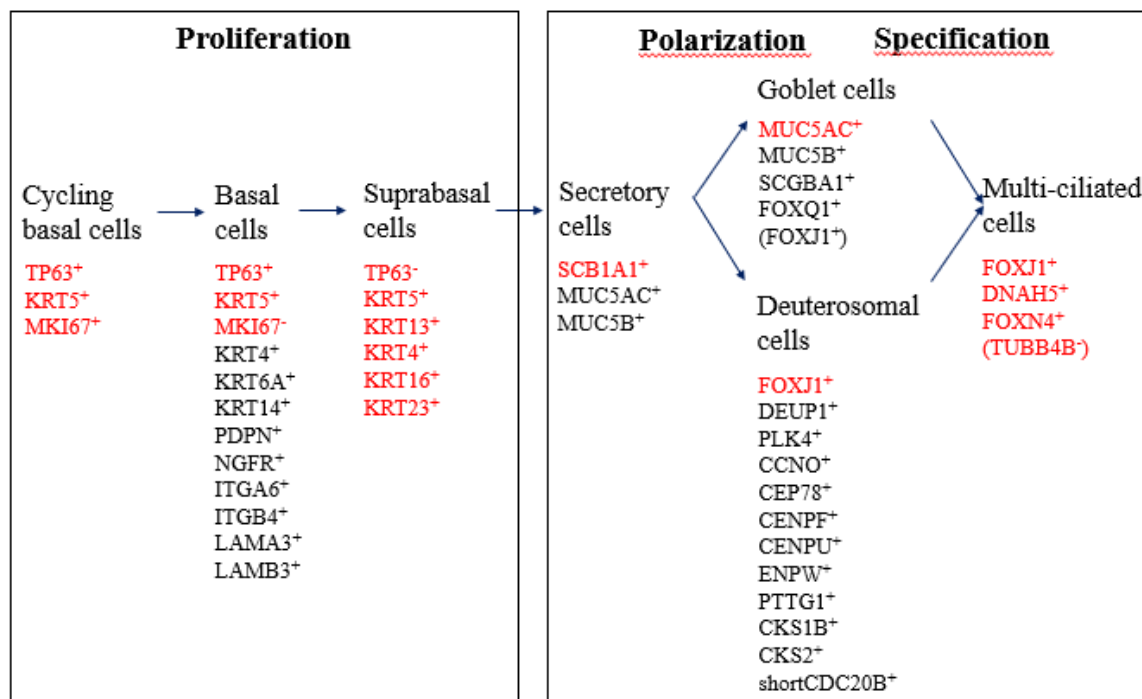
Figure 5: Schematic representation of cell differentiation axis of the primary human bronchial epithelial cells [1,2]. The cycling basal cells give rise to basal cells and suprabasal cells in the early phase of cell differentiation process. Suprabasal cells are progenitor cells for secretory cells (polarization phase), which in turn differentiate into end-differentiated multi-ciliated cells (specification phase). Specific marker genes that characterize the individual cell populations are labeled in red.

Basal cells (BC)

The main roles of BC are cell proliferation and renewal of the bronchial epithelium [65,66]. Next to their progenitor function, BC play crucial roles in cell-cell adhesion processes [65], epithelial barrier integrity [67,68] and intercellular homeostasis. BC control innate immunity processes [69,70] and confer an immune bronchial microenvironment. Their progenitor function is important for both self-renewal [71] and regeneration of neighboring epithelial cells [72] in different pathologic situations including epithelial-to-mesenchymal transition (EMT) [73,74] and malignant proliferation [75,76].

The percentage of BC decreases proportionally with airways size (30-31% in the conducting airways with a diameter > 4 mm and 6% in the smallest airways with a diameter < 0.5 mm) [77].

The specific functions of BC and suprabasal cells (sBC) are illustrated in **Table 10**.

Cell population	Cell subpopulation	Function	Marker expression
Basal cells (BC)	Cycling basal	-Cell proliferation -Cell differentiation -Progenitor function -Barrier integrity -Cell-cell homeostasis -Innate immunity	BC: TP63$^+$, KRT5$^+$, KRT6A$^+$, (small subtype coexpressing KRT14$^+$ or KRT4$^+$ or KRT8$^+$), PDPN$^+$, NGFR$^+$, ITGA6$^+$, ITGB4$^+$, LAMA3$^+$, LAMB3$^+$. Cycling BC: MKI67$^+$
	Non-cycling basal cells (BC type 1)	-Quiescent cells -Reduced migratory activity	TP63$^+$, KRT5$^+$, MKI67$^-$
	Non-cycling basal cells (BC type 2)	-End-differentiated, quiescent cells -Migratory activity	TP63$^+$, KRT5$^+$, FN1$^+$, VIM$^+$, SPARC$^+$, TAGLN$^+$
Suprabasal cell (sBC)	Suprabasal cells type 1, 2, 3 (sBC type 1, 2, 3)	-Intermediate state between BC and secretory cells	TP63$^-$, KRT5$^+$, KRT13$^+$, KRT4$^+$

Table 10: Classification and functional characterization of basal cells (BC) and suprabasal cells (sBC) of the proximal human bronchial epithelium. For each individual cell subtype gene expression signature and main cell functions are separately highlighted.

<u>Multi-ciliated cells (MCC)</u>

MCC are the most frequent cells at the level of the healthy bronchial epithelium. The amount of MCC is inversely correlated to airway size, accounting for 47% in the distal trachea, 53% in the proximal and 73% in the distal bronchi [78,79].

The apical pole of the MCC cells contains 100-300 cilia incorporated into the muco-ciliary escalator with a ciliary beating frequency (CBF) of 11.0 ± 1.3 beats/ second [80] or 7 -16 Hz [81].

The cilia present microtubules containing alpha and beta acetylated tubulin proteins regulated by Forkhead/ winked helix transcription factor (FOXJ1) [80,82,83].

The ciliogenesis comprises 3 steps:

i)   formation and attachment of the basal bodies on the apical side of the cells that exhibit a ciliated phenotype
ii)   formation and alignment of the cilia membrane
iii)   extension of axonemal microtubules for cilia assembly and disassembly [84,85]

Cilia enhance the clearance of accumulated toxin at the level of bronchial epithelium [86,86,87]. MCC play crucial roles in cell signaling (sonic hedgehog and Wnt signaling), membrane homeostasis [88], cell renewal, repair of the bronchial tissue and squamous trans-differentiation (squamous metaplasia) [89,90].

The specific functions and markers of MCC are illustrated in **Table 11**.

Cell population	Cell subpopulation	Function	Marker expression
Multi-ciliated cells (MCC)	Immature MCC (pre-ciliated MCC)	-Intermediate state (secretory ↔ MCC)	$PLK4^+$, MYB^+, $CDC20B^+$, $CEP41^+$
	$FOXJ1^+$ type 1	-Muco-ciliary clearance -Cell signaling -Terminal differentiation -Trans-differentiation	$FOXJ1^+$, $DNAH5^+$
	$FOXJ1^+$ type 2 (deuterosomal cells)	-Muco-ciliary clearance -Cilia biosynthesis, assembly, maturation -Regulation of mitochondrial activity	$FOXJ1^+$, $DEUP1^+$, $PLK4^+$, $CCNO^+$, $CEP78^+$, $CENPF^+$, $CENPU^+$, $ENPW^+$, $PTTG1^+$, $CKS1B^+/2^+$, $shortCDC20B^+$
	$FOXN4^+$ cells	-Intermediate state of ciliary differentiation	$FOXN4^+$, LYZ^+

Table 11: Classification and functional characterization of multi-ciliated cells (MCC) of the human proximal bronchial epithelium. For each individual cell subtype gene expression signature and main cell functions are separately highlighted.

Secretory cells (SC)

SC are classified in club cells/ CC (CC10$^+$, 11%) and goblet cells/ GC (MUC5AC$^+$, MUC5B$^+$, 25%).

i) CC10$^+$ cells

CC10$^+$ cells play crucial roles in mucus secretion, muco-ciliary clearance, mineral homeostasis, innate immunity and cell differentiation processes. In particular, CC10$^+$ cells produce the club cell specific protein 10 (CC10), a 10 kD protein with anti-inflammatory and immunomodulatory roles upon environmental nanoparticle exposure [91,92]. In addition, the presence of CC10 protein and surfactant protein A (Sp-A) in the broncho-alveolar lavage of the terminal bronchioles, indicates a possible role of the CC10$^+$ cells in surfactant production [54,93,94]. Besides secretory function, CC10$^+$ cells act as progenitor cells, being able to transdifferentiate in TFF1$^+$ (trefoil factor family) MCC and GC. This process was observed when bronchial epithelium was exposed to different allergens [95]. In addition, experimental studies showed that CC10$^+$ may regulate cell proliferation, whereas loss of CC10$^+$ may lead to aberrant cell proliferation and carcinogenesis [96].

ii) MUC5AC$^+$and MUC5B$^+$ GC

GC have muco-regulatory properties being responsible for secretion of mucins (MUC5AC$^+$ and B$^+$) on the apical side of the bronchial epithelium [97]. These large proteins (MUC5AC 641 kDa and MUC5B 600 kDa) are the main components of the lining fluid of the muco-ciliary escalator. Mucins increase the viscosity of the lining fluid and enhance due to their hydrophobicity the uptake of the inhaled environmental particles at the level of the bronchial epithelium. Together with MCC, GC facilitate the clearance of the environmental pollutants via muco-ciliary escalator [87]. GC play a crucial role in barrier maintenance, mineral absorption and lung homeostasis [98,99]. In addition, it has been reported that GC are crucial front-line defenders involved in autocrine and paracrine mediated innate immune responses [97,99,100]. Similar to the CC10$^+$ cells, GC act as progenitor cells, giving rise to MCC.

The interplay between SC and MCC is of utmost importance in the cell homeostasis of the bronchial epithelium.

The specific functions and gene markers for SC are illustrated in **Table 12**.

Cell population	Cell subpopulation	Function	Marker expression
Goblet cells (GC)	Goblet cells (GC type 1, 2, 3)	-Muco-regulatory properties -Muco-ciliary clearance -Barrier integrity -Mineral absorption -Autocrine innate immunity -Paracrine innate immunity -Progenitor role	$MUC5AC^+$, $MUC5B^+$, $FOXQ1^+$
	Goblet cell transitory state (GC-MCC)	-Intermediate state between secretory and MCC	$MUC5AC^+$, $FOXJ1^+$, $SCGBA1^+$
Club cells (CC)	$CC10^+$ cells	-Mucus secretion -Muco-ciliary clearance -Minerals homeostasis -Anti-inflammatory effects -Immunomodulatory effects -Progenitor role -Cell differentiation -Cell trans-differentiation	$CC10^+$, $SCGB1A1^+$, $NFIA^+$, $KRT13^+$, $KRT15^+$
	Secretory cells (SC) type 1, 2, 3	-Immune cell migration -Chemotaxis -Secretion of proinflammatory cytokines -Neuroinflammation -Dendritic cell maturation	$SCB1A1^+$

Table 12: Classification and functional characterization of secretory cells (SC) of the human proximal bronchial epithelium. For each individual cell subtype gene expression signature and main cell functions are separately highlighted.

The specific functions and gene markers of the remaining cell types excluding BC, sBC, SC and MCC are illustrated in **Table 13**.

Cell population	Cell subpopulation	Function	Marker expression
Other cells types	Primary neuroen-docrine cells (PNEC)	-Chemosensory function -Pulmonary blood flow -Bronchial tonus -Immunomodulation -Tissue remodeling -Neurosecretion	chromogranin-A (CgA^+), GRP^+, $CGRP^+$, $5\text{-}HT^+$, calcitonin$^+$, substance P^+, somatostatin, SYP
	Tuft/ Brush cells (type 1, 2, 3)	-Chemosensory function -Immunomodulatory effects -Epithelial remodeling -Lung homeostasis	$TRPM5^+$, $ChAT^+$, $G\alpha\text{-gustducin}^+$ ACT^-, $CCSP^-$
	Pulmonary ionocytes	-Regulation of Cl^-/K^+ and Na^+/H^- channels -Regulation of CFTR (cystic fibrosis transmembrane conductance regulator) activity	$FOXI1^+$, $CFTR^+$, GFP^+, $ASCL3^+$, $TFCP2l1^+$, $SLC9^+$
	SLC16A7 cells AIRE cells	-Antigen presentation -Mitochondrial regulation	$SLC16A7^+$, $AIRE^+$

Table 13: Classification and functional characterization of remaining cells excluding basal cells (BC), suprabasal cells (sBC), secretory and multi-ciliated cells (MCC) of the human proximal bronchial epithelium. For each individual cell subtype gene expression signature and main cell functions are separately highlighted.

The differentiation process and the continuous interplay between the outlined cell subtypes at the level of the bronchial epithelium, was comprehensively described using single cell and transcriptome analysis [1,101]. In summary, the single cell hierarchy atlas [1,2] showed that BC ($TP63^+$, $KRT5^+$) have progenitor function for sBC ($TP63^-$, $KRT5^+$, $KRT13^+$, $KRT4^+$), which give raise to SC including CC ($CC10^+$, $SCGB1A1^+$, $NFIA^+$, $KRT13^+$, $KRT15^+$) and GC ($MUC5AC^+$, $MUC5B^+$, $FOXJ1^+$/ $SCGBA1^+$). SC further differentiate into GC ($MUC5AC^+$, $MUC5B^+$, $FOXJ1^+$/ $SCGBA1^+$) and deuterosomal cells ($FOXJ1^+$, $DEUP1^+$, $PLK4^+$, $CCNO^+$), which give raise to end-differentiated MCC ($FOXJ1^+$, $FOXN4^+$, $TUBB4B^-$).

The schematic of pHBECs differentiation is summarized in **Figure 6**.
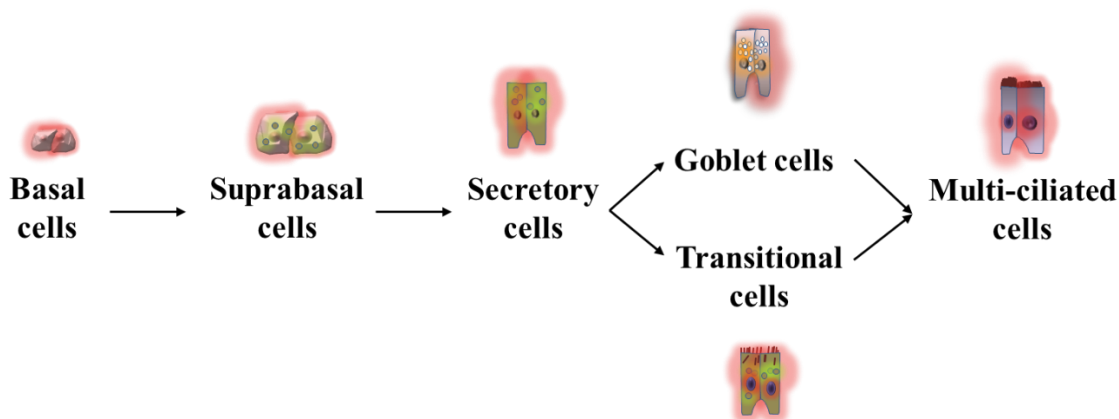
Figure 6: Schematic of cell differentiation axis of the primary human bronchial epithelial cells based on the human lung cell hierarchy atlas published by Ruiz Garcia et al. and Deprez et al. [1,2]. Accordingly, primary basal cells give rise to suprabasal cells which are precursors for secretory cells. Secretory cells further differentiate into goblet cells or transdifferentiate into transitional cells. This intermediate cell state gives rise to terminally differentiated multi-ciliated cells.

Interestingly, these physiological processes take place as outlined above when the bronchial epithelium has intact cell composition and functions.

Despite extensive research, however, the epithelial cell differentiation process in end-stage COPD patients remains to date an insufficiently characterized topic.

1.4 *In vitro* and *ex vivo* culture models of the human bronchial epithelium

Since air pollution is one of the major risk factors in COPD development and progression, many studies are focused on the complex responses of the respiratory mucosa upon $PM_{2.5}$ exposure. These studies proposed culture models under submerged conditions or at air liquid interface (ALI) under more physiologic short-term [27] or long-term culture conditions [27,102]. These ALI models were based on cultures of a single cell line including immortalized bronchial epithelial cells (e.g. BEA-2B)[103], adenocarcinoma cell lines (A549)[104 105,106] or primary human bronchial epithelial cells (pHBECs)[107].

In order to realistically simulate the physiological cell-cell interactions upon pollutant exposure, more sophisticated ALI co-culture models based on human bronchial epithelial cells (Calu-3, 16HBE14o- (16HBE), H292, and BEAS-2B) and AM have been established[108,109].

Besides the classical submerged 2D airway culture models, as well as the lung organoids and lung-on-a-chip models, development of novel 3D biomimetic cell culture models are crucial for the analysis of pHBECs differentiation and characterization of post-exposure effects.

The most frequent *in vitro* and *ex vivo* lung culture models are described in **Table 14**.

Culture type	Advantages	Disadvantages
2D *in vitro* submerged	-Cheap -Easy-to-use, fast culture -Toxicology and drug screening research	-Short-term culture (2-3 weeks) -Not physiologic/ no ALI -Lack of the native 3D *in vivo*-like architecture of the airways
3D *in vitro* Air Liquid Interface (ALI)	-Easy-to-use and reproducible -Maintenance of disease specific characteristics -Toxicological research, drug screening and toxin exposure -Lower costs than lung-on-a-chip or organoids	-Complex long-term culture -Risks for contamination or cell dedifferentiation. -Lack of the native 3D *in vivo*-like architecture, and of the morphological features of the native tracheo-bronchial system
3D *ex vivo* culture of bronchial punches (BPs)	-Preservation of the intact 3D native lung tissue architecture -Analysis of all cell population of the bronchial epithelium	-Limited culture lifetime -High risk for contamination.
3D lung organoids	-High reproducibility -Long-term preservation of disease specific cell features -Toxicological drug screening	-Expensive -Complex maintenance -Risks for contamination -Lack of the native 3D *in vivo*-like architecture of the airways
3D human lung-on-a-chip	-Physiological ALI lung-vessel microenvironment -Study of functional cells producing mucus/ surfactant, and of inflammatory and oxidative stress responses -Toxicological research	-Very expensive -Difficult to manufacture -High-throughput drug screening not possible -Lung architecture and its physiological functions cannot be accurately recapitulated.

Table 14: Characterization of 2D and 3D *in vitro* and *ex vivo* lung culture models, modified after Paolicelli et al. [6]. For each culture model main advantages and disadvantages are specified. The culture models used in our study are highlighted in gray.

The 3D *in vitro* ALI models are preferred over the unphysiological submerged cultures or the more sophisticated and expensive lung organoids or lung-on-a-chip models. Our project uses physiological long-term ALI cultures exposed to environmental NP.

Six steps are necessary to establish this culture (**Figure 7**):

i) Immediate isolation of pHBECs derived from native bronchial tissue pieces sampled upon lung transplantation
ii) Submerged culture on Petri dishes for 7-14 days
iii) Cell transfer on transwells inserts that permit the contact of the pHBECs with the medium on the basolateral side and with the air on the apical side
iv) Submerged culture on transwell inserts (2-7 days for healthy pHBECs and up to 21 days for COPD-IV diseased pHBECs)
v) Airlift by suction of the apical medium of the transwells (ALId0)
vi) Long-term ALI culture (up to 28 days, ALId0-28)

This culture facilitates a physiological cell differentiation in contact with the air on the apical side and with the growth factors (basal media) on the basolateral side. It can be maintained weeks or months, thus allowing the study of disease progression [110]. In addition, ALI culture can be performed for toxin and drug exposures, using standardized NP exposure devices (e.g. VITROCELL® CLOUD 12, VITROCELL Systems, Germany) [6].
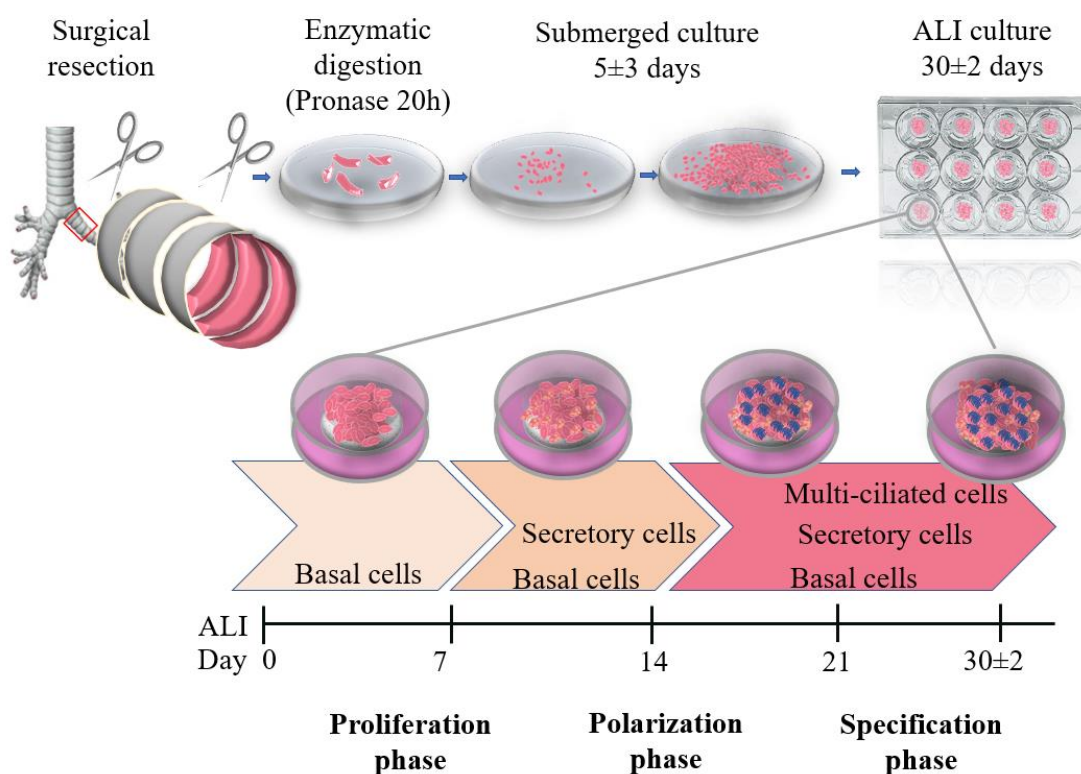
Figure 7: Schematic representation of the long-term air liquid interface (ALI) *in vitro* culture model based on primary human bronchial epithelial cells (pHBECs). Immediate isolation of pHBECs from proximal human bronchi derived from lung explants is followed by enzymatic digestion of the dissected bronchial mucosa and the submerged culture of the pHBECs. Cells are seeded on transwells upon achieving 70-90% confluency and air-lifted (ALId0) by suction of the apical media. The resulted ALI culture is maintained up to 28 days (ALId0-28) in order to facilitate terminal pHBECs differentiation into secretory and multi-ciliated cells.

The long-term ALI culture is based on three phases illustrated in **Figures 8**.

i)   Pre-expansion phase:

      -submerged culture of pure pHBECs on Petri dish (7-14 days) until achieving 70-90% confluency and transfer of the pHBECs on ALI transwells

ii)   Proliferation phase:

      -Expansion of pure pHBECs under submerged conditions on ALI transwells followed by airlift by 95% cell confluency and preliminary ALI culture (ALId0-12)

      -Polarization/ differentiation of pHBECs into suprabasal, secretory and multi-ciliated cells (ALId12-21)

iii)   Specification phase:

      -Terminal differentiation of pHBECs into secretory and multi-ciliated cells (ALId21-28) according to the human lung cell hierarchy atlas [1,2]
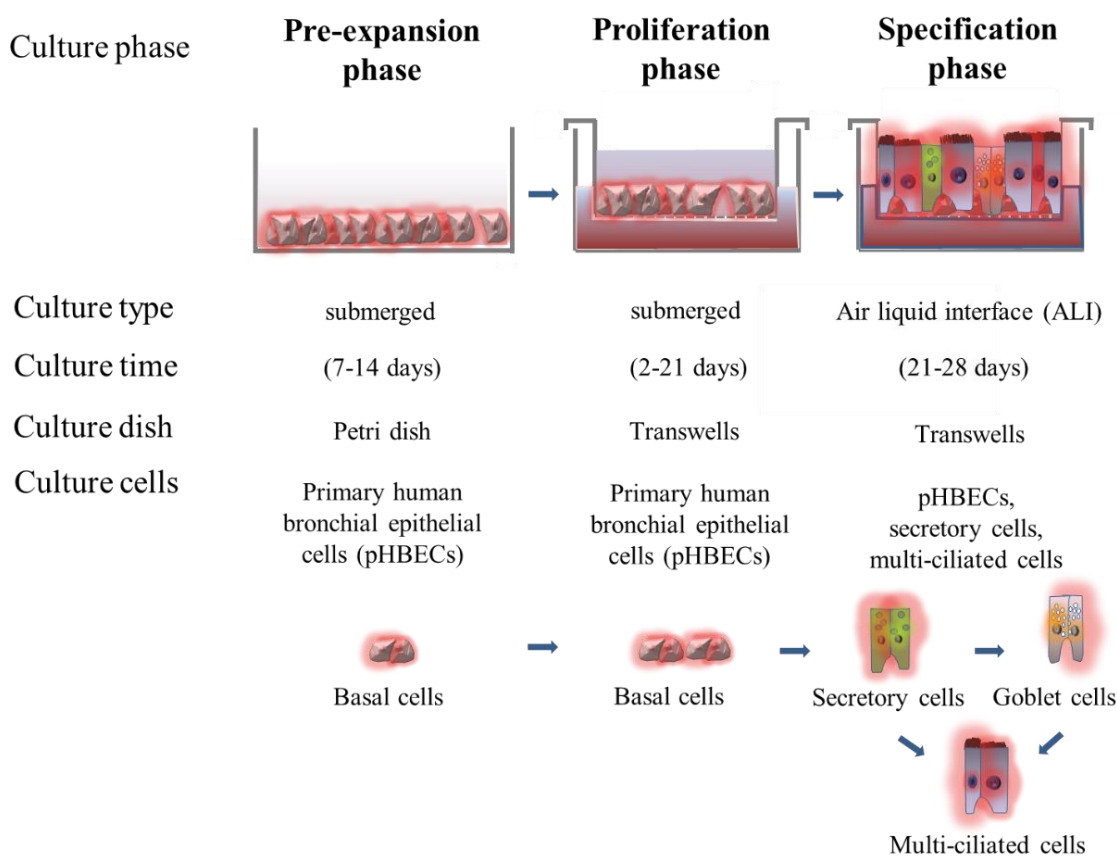
Figure 8: Characterization of the culture phases of the long-term air liquid interface (ALI) *in vitro* culture model based on primary human bronchial epithelial cells (pHBECs). Cell differentiation process comprises three phases: pre-expansion, proliferation and specification phase. While pre-expansion phase is exclusively based on submerged pHBECs until achieving 70-90% confluency, proliferation phase is based on pHBECs until achieving 95% confluency on transwells, followed by the culture of basal, secretory and multi-ciliated cells until ALId21. Specification phase coincides with the terminal differentiation of the pHBECs, with an end-differentiated epithelium containing basal, secretory and multi-ciliated cells.

1.5 Objectives of the PhD Thesis

To date, insight into the cell differentiation potential of the chronically challenged bronchial epithelium is missing. A better understanding of the mechanisms that trigger cell regeneration, repair and resilience of the diseased bronchial epithelium is of crucial importance to inform novel preventive and therapeutic strategies. In the light of the high impact of the continuous toxin exposure on human health and, in particular, in the development of untreatable irreversible respiratory diseases, our study aimed to:

1. Investigate the effects of air pollutant exposure on cell composition and epithelial function of the primary airway epithelium derived from healthy (non-CLD) and diseased (COPD-IV) patients

Airway cells from end-stage COPD patients are exposed to selected air pollutants (CNP, ZnO and endotoxin/ LPS) in order to analyze cell composition and functional changes at the level of the bronchial epithelium. In particular, survival mechanisms underlying regulatory signaling pathways and transcription factor profiling are investigated and compared between diseased (COPD-IV) and healthy controls (non-CLD).

2. Characterize the differentiation process of pHBECs from healthy (non-CLD) and diseased patients (COPD-IV) with a focus on differences in basal cell populations and their secretory-multi-ciliated differentiation axis.

Cell differentiation process is analyzed *in vitro* in a physiological, long-term ALI culture model by stimulating the growth pattern of the different cell subtypes as well as the physiological muco-secretory and ciliogenic pattern. The temporo-spatial dynamics of the differentiation process is analyzed at 7 different timepoints during differentiation via single cell RNA sequencing and 3D confocal IF. Specific cell populations identified in non-CLD cultures during differentiation are analyzed with those cultures derived from patients with COPD-II and COPD-IV. Signaling pathways that trigger terminal cell differentiation and ciliogenesis (i.e. Notch, Wnt and TGF-β) are comparatively analyzed at transcriptome and single cell level.

To address the outlined objectives, we:
    i) established and validated a physiological long-term 3D biomimetic ALI culture system using pHBECs derived from diseased patients (COPD-II and -IV) in reference to non-CLD derived cells

    ii) exposed pHBECs at ALI to relevant environmental pollutants by using the preclinical, highly standardized VITROCELL® CLOUD 12 cell exposure system

    iii) described for the first time particular cell trajectories of the non-CLD and COPD-IV bronchial epithelium with focus on distinct BC subpopulations regulating the SC-MCC differentiation axis.

2. Material and Methods

2.1 Patient characteristics

Lung bronchial tissue samples were obtained from n=9 patients suffering from COPD (n=3 COPD-II and n=6 COPD-IV) and n=4 non-chronic lung disease (non-CLD)/ healthy patients. The study was approved by the local ethics committee of the Ludwig-Maximilians-University, Munich, Germany (CPC-M bioArchive, #333-10 and #454-12). Written informed consent was obtained from all patients undergoing lung transplantation at the Thoracic Surgery Department of the Ludwig-Maximilians-University Hospital or lung tumor resection at the Asklepios Pulmonary Hospital Munich-Gauting, Germany. Collected tissue samples upon lung transplantation were included in the COPD group. Collected tissue samples (healthy peritumoral tissue) from patients with lung tumors were included in the healthy (non-CLD) group. Medical records included lung function parameters, microbiological and histopathological analysis as well as smoker status and comorbidities. CMV infection status was recorded for all patients undergoing lung transplantation.

2.2 Isolation of primary human bronchial epithelial cells (pHBECs)

Isolation of pHBECs from fresh native bronchial tissue was performed in accordance with the previously described protocol [107]. 3D biomimetic cultures at ALI derived from n=4 non-CLD, n=3 COPD-II and n=4 COPD-IV patients were established upon pHBECs isolation.

For the two parts (objectives, page 48) of the study two digestion protocols were used. Accordingly, the enzymatic digestion was performed by using two proteases:

i)   Pronase E® (protease from Streptomyces griseus, Type XIV ≥3.5 units/ mg solid, Sigma, REF: 5147) for 20 hours for both non-CLD and COPD-IV cultures (Pronase protocol)

ii) Dispase® (protease from Bacillus polymyxa, SIGMA, D4818, REF: 42613-33-2) and 25 µl RNase-free DNA-ase for 20 minutes for COPD-IV tissue samples and 30 minutes for non-CLD tissue samples (Dispase protocol)

The standard ALI cultures were processed according to the Pronase protocol. Here, freshly isolated bronchial mucosa pieces from n=4 non-CLD patients, n=3 COPD-II and n=3 COPD-IV patients were enzymatically digested with Pronase E®, followed by submerged cultures with PneumaCult™ - Ex Plus Media (STEMCELL Technologies, REF: 05041) until achieving 70-90% confluency.

The cultures required for the preparation of single cell suspensions and drop-seq single cell RNA-seq analysis were processed according to the Dispase protocol. In summary, fresh native bronchial tissue samples derived from n=2 non-CLD and n=2 COPD-IV

patients were enzymatically digested with Dispase® and RNase-free DNA-ase. This short-term digestion allowed the preservation of all cell populations of the bronchial epithelium. The enzymatic activity was inhibited with 5 ml of phosphate buffered saline (PBS) containing 10% FCS. Cells were filtered through a 70 μm strainer and centrifuged at 300xg for 5 minutes at 4°C. To remove the remaining cells and potential contaminants, the pellet was resuspended in 3 ml of red blood cell lysis buffer and incubated at room temperature for 2 minutes. In the next step, 10 ml of PBS containing 10% FCS was added to the suspension. The mix was resuspended and centrifuged for 5 minutes at 300xg and 4°C. The supernatant was discarded and the cells resuspended in 1 ml of PBS containing 10% FCS. Cell number was counted by using a Neubauer chamber and the cells were critically checked for single cell separation. The resulted dead cells were removed. A maximal amount of 15% is allowed to continue with 85% viable cells for the drop-seq analysis. 250.000 cells were aliquoted in 2.5 ml of PBS enriched with 0.04% of bovine serum albumin (BSA) to produce a final concentration of 100 cells/ μl that can be loaded for further drop-seq analysis.

2.3 *In vitro* cell culture at Air-Liquid-Interface (ALI)

Culture of pHBECs at ALI was performed according to our standardized protocol, in detail described by Schamberger et al. [107].

A schematic representation of long-term ALI culture is illustrated in **Figure 9**.
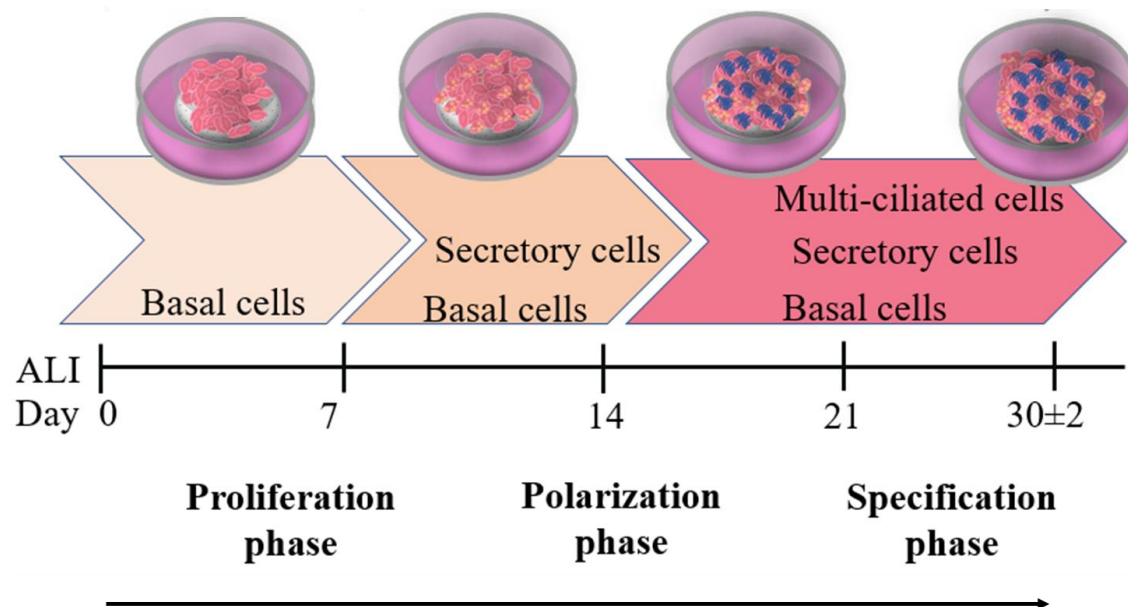
Figure 9: Schematic representation of the ALI culture phases of pHBECs culture model *in vitro*. Upon airlift (ALId0), differentiation process of pHBECs comprises three phases (proliferation, polarization and specification). Accordingly, basal cells (proliferation phase) give rise to secretory cells with a maximum amount on ALId14 (polarization phase) that initiate the differentiation into multi-ciliated cells. The specification phase coincides with the terminal differentiation of pHBECs culture containing basal, secretory and multi-ciliated cells with a maximum amount on ALId28.

Freshly isolated pHBECs seeded on Collagen IV-coated transwell inserts were cultured in PneumaCult^{TM} - Ex Plus Media (STEMCELL Technologies, REF: 05041) until 95% cell confluency. The apical media is aspirated (Airlift) and the ALI culture initiated. pHBECs at ALI have direct contact to the air on the apical side and to the basal media on the basolateral side. ALI Basal Media (PneumaCult^{TM} – ALI Basal Media, enriched with 100x PneumaCult^{TM} - ALI Maintenance Supplement, STEMCELL Technologies, REF: 05006) was changed every other day. pHBECs differentiation into SC (ALId7 onwards) is suggested by the presence of the apical mucus. The mucus was washed every 7 days with HBSS Ca^{2+}/ Mg^{2+} (Gibco Life Technologies, REF: 14065-049). ALI culture was validated by TEER, WST-1, LDH, IF and drop-seq single cell RNA-seq analysis.

2.4 *Ex vivo* culture of the native bronchial tissue at ALI

To validate the cellular distribution and composition of fully differentiated pHBECs culture a novel ALI model based on *ex vivo* culture of human bronchial tissue samples was developed in our laboratory. Human native bronchial tissue pieces were immediately processed after lung transplantation or tumor resections. Peribronchial fat was removed and bronchial pieces were washed 3 times in ice-cold PBS to remove mucus and reduce contamination risk. Bronchial rings were dissected in small tissue pieces (2 cm^2) and washed 3 times in ice-cold DMEM/ F12 Media (Gibco Life Technologies, REF: 11330-032) supplemented with 10000 U/ml Penicillin, 10000 µg/ml Streptomycin, 250ug/ml Amphotericin B (Gibco Life Technologies, REF: 15290-026), 15 mM HEPES and 29.2 mg/ml L-Glutamine (Gibco Life Technologies, REF: 10378016, 100x). Each bronchial piece was sectioned in bronchial punches (BPs) by a 4 mm tissue puncher (PFM medical, Kai Europe GmbH, REF: 48401). BPs were seeded on inserts that allow contact with the media on the basolateral side and with the air on the apical side (**Figure 10**).
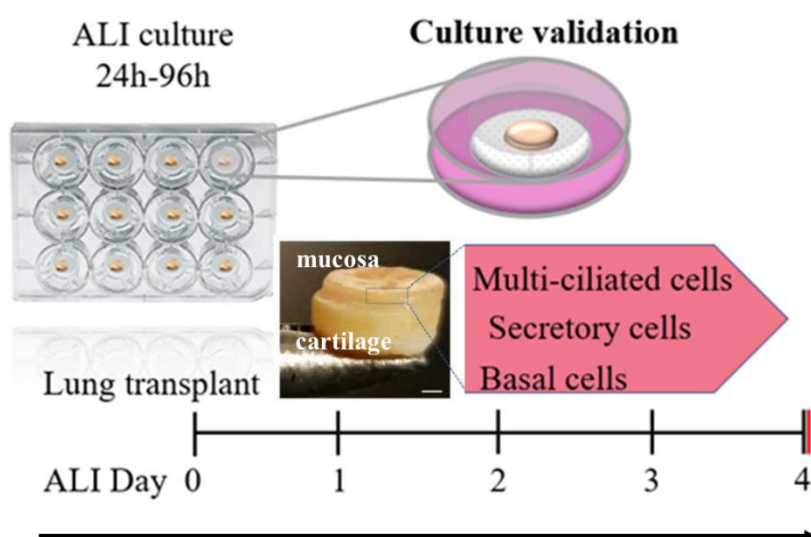
Figure 10: Schematic representation of the air liquid interface (ALI) *ex vivo* culture model based on native human bronchial punches (BPs). Upon lung transplantation, an immediate culture of BPs is initiated and maintained up to 4 days at ALI. BPs are bronchial wall samples entirely preserving the native architecture of the human bronchi, containing a cartilaginous part (basal side) and submucosa/ mucosa (apical side). Only the cartilaginous part of the BPs has contact with the media, whereas the mucosa has contact with the environmental air. BPs were cultured up to 4 days at ALI, carefully avoiding the mucosa submersion. The culture validation was done by immunofluorescence.

2.5   Nebulization of NP via VITROCELL® CLOUD 12 cell exposure system

Fully differentiated pHBECs were exposed to relevant aerosolized NPs in a dose- and time- dependent manner using the ALICE CLOUD technology (VITROCELL® CLOUD 12, VITROCELL Systems, Waldkirch, Germany) (**Figure 11**), according to the previously described protocol [111].
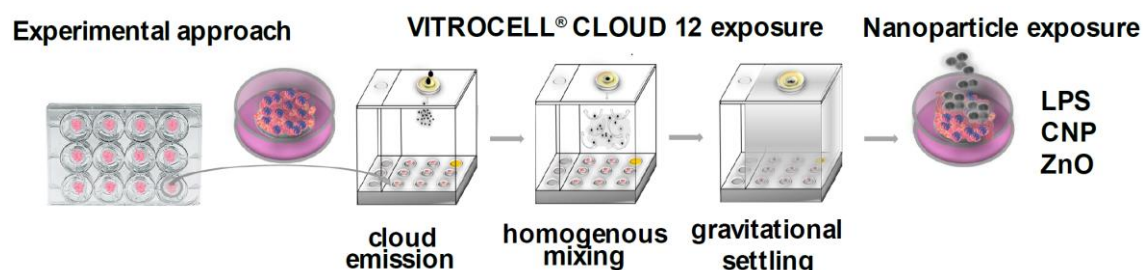
Figure 11: Experimental approach of Nanoparticle (NP) exposure by using the highly standardized, preclinical VITROCELL® CLOUD 12 cell exposure system: up to 8 ALI transwells containing fully differentiated pHBECs on ALId28 are transferred in the exposure system. The exposure comprises 3 steps: cloud emission, homogenous mixing of the aerosolized droplets and gravitational settling aiming at an uniform NP deposition on the apical surface of the cells in 3-5 min. LPS, Carbon soot surrogate NP (CNP) and Zinc Oxide were selected for NP exposure.

The NPs used in our experiments are present in the environmental air of the highly industrialized cities as result of uncontrolled combustion processes: carbon soot surrogate nanoparticles (CNPs, Printex 90, primary particle size: 14 nm, Degussa, Germany) and Zinc oxide nanoparticles (ZnO, JRC reference material NM110, primary particle size: 158 nm). Briefly, 200 µl of sample (test-solution or NP suspension) is pipetted into a clinically relevant vibrating mesh nebulizer (Aeroneb Pro, Serial number 186056-036, Aerogen Inc., Galway, Ireland). The sample is nebulized into the exposure chamber loaded with up to eight transwell inserts. The VITROCELL® CLOUD 12 system provides a realistic NP deposition on the apical side of the cells in three steps: cloud emission, homogenous mixing and gravitational settling. An uniform particle deposition is achieved in 3-5 min [111]. The doses that reach the apical surface of the cells are measured by an integrated quartz crystal microbalance (QCM), which is placed in the right upper corner of the device. To mimic physiological exposure conditions, a constant system temperature (37°C) was maintained during whole time of exposure. After exposure, the cells were immediately transferred back into the incubator for 24 hours. In order to obtain an optimal NP size, NP agglomerates were treated with a probe sonicator (Bachofer GmbH, Reutlingen, Germany) at 30% output energy for 30 seconds for CNP (37 J/mL sonication energy) and 160 seconds for ZnO (195 J/mL). The median volumetric diameter of the dispersed NP (160 nm for CNP and 260 nm for ZnO NP) was determined by DLS (Dynamic Light Scattering; Zetasizer, Malvern Instruments, GBR). Untreated (sham) controls in which the cells were only exposed to saline solution 0.9% (the same used for NP suspensions) were included. The proinflammatory and OS responses after NP exposure were compared to saline solution (sham control), LPS (positive control, inflammation reference, 1mg/ ml aerosolized particles, lipopolysaccharides from Escherichia coli O55:B5, L2880, Sigma-Aldrich) and 0.2 % TritonX-100 (used as cytotoxicity high control, $(C_2H_4O)_nC_{14}H_{22}O$, 9002-93-1, Sigma-Aldrich).

The characteristics of the nebulized NP are summarized in **Table 15**.

Nebulized Nanoparticles	BET (m^2/g)	Median diameter (nm)	NP conc (mg/ml)	Mass dose ($\mu g/cm^2$)*	Surface area dose cm^2/cm^2
Sham (water)	-	-	0	0	-
LPS (1 mg/ml)	-	-	1	0.70	-
CNP/ Printex90	310	201±48	5	3.50	10.8
ZnO low dose	12	307±12	1.75	1.22	0.147
ZnO high dose	12	-**	38.12	267	3.20

Table 15: Characteristics of the nebulized nanoparticles (NPs). Endotoxin (LPS), Carbon soot surrogate NP (CNP) and Zinc Oxide (ZnO, two doses) were selected for NP exposure. Upon NP exposure, following parameters were analyzed: BET (mass-specific surface area of NPs according to Brunauer et. al[7], m^2/g), median volume-weighted diameter (±SD, n=3, nm) of size distribution of NPs agglomerates in nebulized suspension measured by dynamic light scattering, nanoparticle concentration (NP conc, mg/ml), cell delivered mass dose (*, $\mu g/cm^2$) and surface area dose (cm^2/cm^2) calculated from the deposited NP mass per cell-covered area ($\mu g/ cm^2$) measured with a quartz crystal microbalance and the BET value of the NPs. ** DLS measurement not possible due to the high NP concentration.

2.6   Cigarette smoke extract (CSE) treatment of pHBECs

In order to characterize the differentiation process of the diseased pHBECs and to demonstrate the toxin-induced disease progression, COPD-II derived pHBECs (n=3) were treated on the basolateral side with cigarette smoke extract (CSE) during whole time of differentiation (ALId0-28) as previously reported [112].

The CSE resulted from the smoke of six Research Cigarettes (Tobacco laboratory research, University of Kentucky, Tobacco research and development center, TP-7-VA, V347X61B5, CODE 3R4F 12/2006). The CSE was filtered through a 0.22 µm filter and diluted in 100 ml basal media (PneumaCult[TM] STEMCELL Technologies, REF: 05006) to obtain a 5% extract solution. CSE medium was applied on the basolateral side of the cells every second day.

The membrane resistance and integrity of the exposed cells were analyzed weekly (on ALId7, 14, 21 and 28) by TEER and LDH. The compositional changes upon chronic CSE exposure were assessed by 3D confocal IF.

2.7   Functional and compositional analysis of NP challenged and unchallenged pHBECs *in vitro*

To describe the effects of the toxin exposure on the human bronchial epithelium, following assays were performed in the pHBECs cultures with and without NP exposure:

-functional assays: WST-1 (cell viability), lactate dehydrogenase (LDH) release (membrane integrity), transepithelial electrical resistance (TEER, barrier integrity), ciliary beating frequency (CBF)

-compositional assays: 3D confocal Immunofluorescence (IF) of pHBECs cultures and native bronchi, RNA isolation, transcriptome and secretome analysis

2.7.1 WST-1 assay

WST-1 assay is a functional assay usually performed to asses cell viability and proliferation. Reduction of WST-1 tetrazolium salt to a formazan dye product takes place at the cell surface of the viable cells in a NAPDH-dependent manner. This process can be spectrophotometrically measured at an optical density of 450 nm by an optical spectrometer (e.g. Magellan microplate reader device) according to the described manufacturer's instructions. Cell viability was measured for fully differentiated pHBECs at baseline level and 24 hours after NPs challenge. Accordingly, 500 µl WST-1 cell proliferation reagent (Roche Diagnostics GmbH, CAT: 11644807001) was added on the top of the cultured pHBECs and incubated for 25 minutes at 37°. After collection, WST-1 reagent was centrifuged for 5 minutes at 1000xg and analyzed spectrophotometrically. Following incubation, color of WST-1 reagent remains pinkish in viable cells and changes to yellow in dead cells.

2.7.2 Lactate dehydrogenase (LDH) assay

LDH assay is a functional cytotoxicity assay that analyses the integrity of the cell membrane. The extracellular release of LDH upon cell membrane injury reversibly catalyzes the conversion of lactate to pyruvate and NAD to NADH that can be quantified spectrophotometrically at an optical density of 450-490 nm. The LDH release assay kit (LDH Cytotoxicity Detection Kit, Roche Diagnostics GmbH, REF: 11644793001) provides a mixture of 2 reagents (1:45) that are added on the top of the cultured cells and incubated for 30 minutes at room temperature, according to the previously described protocol [112]. Following incubation, color of apical media remains pinkish in viable cells and changes to dark red in dead cells. Untreated cells were used as low control and 0.2% TritonX-100 treated cells were considered cytotoxic high controls.

2.7.3 Transepithelial Electrical Resistance (TEER)

TEER is a functional assay that assesses the barrier function and membrane integrity of the cells. TEER values are measured in Ohm (Ω) and adjusted to the surface area of the transwells inserts (x 1.12 cm^2), in accordance with the company instructions [112]. Physiologic TEER values for an intact cell membrane in pHBECs ALI culture are considered 766±154 Ohm x cm^2 according to Srinivasan et al.[4]. TEER measurement was used to validate the differentiation process of pHBECs at ALI (day 7-28) and to analyze the cell barrier integrity 24 hours after NPs exposure.

2.7.4 3D confocal Immunofluorescence microscopy (IF)

These analyses were performed in collaboration with M. Gerckens and Dr. G. Burgstaller (IF protocol of bronchial punches), Dr. M. Heydarian and PD Dr. A. Hilgendorff (IF protocol of native bronchi embedded in paraffine) (Institute for Lung Health and Immunity and Comprehensive Pneumology Center with the CPC-M bioArchive; Helmholtz Zentrum Munich, Germany).

pHBECS and BPs were washed with HBSS (Ca^{2+} and Mg^{2+}), fixed apical and basolateral with 4% paraformaldehyde, permeabilized with 0.2% Triton X-100/ HBSS for 15 minutes at room temperature and blocked with 5% BSA/ 0.2% Tween/ HBSS for one hour. The ALI membranes and BPs were stained with appropriate dilutions of primary antibody overnight at 4°C and secondary antibody for one hour in the dark. The used primary and secondary antibodies are summarized in **Table 16**.

	Biological source	Molecu-lar mass	Ig class	Dilution	Company
Primary antibody					
Acetylated α-Tubulin (Ac. Tub$^+$)	mouse	52 kDa	IgG2b	1:500	Abcam REF: 179484
MUC5AC$^+$protein	mouse	63 kDa	IgG1	1:250	Abcam REF: 3649
Club cells secretory protein (CC10$^+$)	mouse	10 kDa	IgG1	1:300	Santa cruz REF: 25554
Cytokeratin 5 (Krt5$^+$)	rabbit	58 kDa	IgG	1:100	Thermo Fisher REF: MA5-16372
Laminin β-3 (LAMB3$^+$)	rabbit	125 kDa	IgG	1:100	Thermo Fisher REF: PA5-21514
FOXJ1$^+$	mouse	50 kDa	IgG1	1:100	Bioscience™ REF: 14-9965-82
RPLP1$^+$	rabbit	29 kDa	IgG	1:100	Novus REF: 81293
Secondary antibody					
Alexa Fluor™ 488	goat anti-mouse		IgG H+L	1:400	Thermo Fisher REF: A11004
Alexa Fluor™ 568	goat anti-rabbit		IgG H+L	1:400	Thermo Fisher REF: A11008

Table 16: Key features of the primary and secondary antibodies used for immunofluorescence protocol according to the manufacturer' specifications. For each antibody biological source, molecular mass (kDa), Ig class, used dilution and company name were specified.

Representative 3D images were taken by using a confocal laser scanning microscope (LSM) from 6 independent differentiations (n=3 non-CLD and n=3 COPD-IV cultures) with 3 different pictures for each treatment condition. Taking the colocalization of the MUC5AC$^+$ cells and CC10$^+$ cells reported by Schamberger et al. into account [112] , we deduced the percentage of single positive MUC5AC$^+$ and CC10$^+$ cells by substracting the reported colocalization fractions (2/3 and 8/17 from the absolute number of MUC5AC$^+$ and CC10$^+$ cells, respectively). The 3D images of the IF stainings were analyzed by using the IMARIS Software and plotted as mean ± SEM via GraphPad prism 8.2 Software.

2.7.5   RNA isolation and transcriptome analysis

These analyses were performed in collaboration with Dr. M. Irmler and Prof. Dr. J. Beckers (miroarray, Ingenuity Pathway Analysis®) (Institute of Experimental Genetics, Ludwig-Maximilians-University of Munich (LMU), 81377 Munich, Germany)

RNA isolation from the lysed pHBECs at ALI was performed by using the RNeasy Plus Mini Kit (Qiagen, Hilden, Germany). Control of RNA quality was assessed using the Agilent 2100 Bioanalyzer. Only samples with a RNA integrity number >7 were used for further microarray analysis. Amplification of total RNA was performed via WT PLUS Reagent Kit (Thermo Fisher Scientific Inc., Waltham, USA) and hybridization of the cDNA was performed via Human Clariom S arrays (Thermo Fisher Scientific). Staining and scanning were performed with a Gene Chip Scanner (3000 7G) according to the previous protocol reported by the manufacturer. Normalized signal space transformation (SST-RMA) of gene-level data were performed via the Transcriptome Analysis Console (TAC; version 4.0.0.25; Thermo Fisher Scientific).

2.7.6   Single cell RNA-seq drop-seq analysis

These analyses were performed in collaboration with Dr. M. Strunz (single cell suspensions, drop-seq analysis), M. Ansari and Dr. H. Schiller (Ingenuity Pathway Analysis®, enrichments, datasets analysis) (Institute for Lung Health and Immunity and Comprehensive Pneumology Center with the CPC-M bioArchive; Helmholtz Zentrum Munich, Germany)

Drop-seq experiments were performed in accordance with the previously described protocol [113,114]. The protocol was adapted for an optimized preparation of the single cell library by Angelidis et al. [5].

One hundred/ µl single cell suspensions encapsulted with oligo-barcoded beads (120/ µl, ChemGenes Corporation, Wilmington, rates of 4000 µl/ hour) were incorporated in the droplet emulsions. The oligo-barcoded beads were produced by using a microfluidic Polydimethylsiloxane device (Nanoshift LLC, 1401 Marina Way South Suite 310, Richmond, CA 94804). Each droplet emulsion was collected for 10-20 minutes and broken for isolation of the oligo-barcoded beads carrying hybridized mRNA transcripts (Maxima RT, Thermo Fisher). For reverse-transcription and pre-amplification (12 cycles) a 100 µM PCR primer (AAGCAGTGGTATCAACGCAGAGT) was used according to the previously described protocol [113].

PCR products were cleaned up after collection using Solid Phase Reversible Immobilisation (SPRI) beads (CleanNA, Coenecoop 75, 2741 PH Waddinxveen) and prepared for

tagmentation. The unfragmented DNA was tagged with a P5 primer (Integrated DNA Technologies) using the Nextera XT Kit (Illumina, Inc, 5200 Illumina Way, San Diego, CA 92122 USA). Single cell libraries were sequenced via Illumina HiSeq4000 system in a 100 bp paired-end run (0.2 nM denatured sample, 5% PhiX spike-in). The microfluidic devices produced a polydimethylsiloxane (PDMS) master mold by using photolithography for the drop-seq device design (CAD file: http://mccarrolllab.org/dropseq/). The master mold fabricated from a SU-8 photoresist (MicroChem, USA) was spin-coated on a 3" silicon wafer for generation of 125 μm-thick uniform layers.

The master mold, filled with a 10:1 mixture (base, curing agent of the PDMS kit Sylgard 184 Dow Corning, USA) was incubated at 60°C for 4 hours to facilitate PDMS crosslinking. The resulted PDMS replica were extracted from the master mold via an 1 mm puncher, treated with O_2 plasma, sealed with a 2" x 3" microscopic slide and treated with Aquapel (Pittsburgh Glass Works, USA) to increase the inner surface roughness (super-hydrophobicity).

The cell signatures and trajectories published by Deprez et al.[2] were used to score the established cell types.

2.7.7 Secretome analysis - quantitative proteomics

These analyses were performed by Dr. SM Hauck (protein isolation, percolator algorithm, protein quantification) (Metabolomics and Proteomics Core, Helmholtz Center Munich, German Research Center for Environmental Health GmbH, 80939, Munich, Germany)

Apical wash of ALI cultures were lysed with LysC and trypsin according to the previously described FASP (filtered aided sample preparation) protocol [115,116]. Eluted peptides were analyzed by using a mass spectrometer (Thermo Fisher Scientific) combined with a UItimate 3000 RSLC nano-HPLC (nano-high performance liquid chromatography, Dionex). Resulted samples were introduced onto the C18 trap cartridge, eluted and separated on the C18 analytical column (Acquity UPLC M-Class HSS T3 Column, 1.8 μm, 75 μm x 250 mm; Waters) by a 90 minutes non-linear acetonitrile gradient at a flow rate of 250 nl/min. Spectra were analyzed at a resolution of 60000 with a maximum injection time of 30 ms from 300 to 1500 m/z. The 10 most abundant peptide ions were selected for fragmentation via HCD (higher energy collisional dissociation) with a normalized collision energy of 27, an isolation window of 1.6 m/z, and a dynamic exclusion of 30 s. Tandem mass spectrometry (MS/ MS spectra) was recorded at a resolution of 15000 with a maximum injection time of 50 ms. Acquired raw data was analyzed by using the Proteome Discoverer 2.4 SP1 software (Thermo Fisher Scientific; version 2.4.1.15). For peptide and protein identification the database Sequest HT against the SwissProt Human database (Release 2020_02, 20435 sequences; 11490581 residues) were used. The Percolator algorithm described by Käll et al. was used for validating the peptide spectrum matches [117]. Quantification of proteins, after precursor recalibration, was based on intensity values for all unique peptides per protein.

2.7.8 Ciliary beating frequency (CBF) analysis

These analyses were performed in collaboration with A. Castelblanco (script development, CBF quantification) (Institute for Lung Health and Immunity and Comprehensive Pneumology Center with the CPC-M bioArchive; Helmholtz Zentrum Munich, Germany)

CBF was calculated in accordance with the previously reported protocol (ciliaFA) by using some adaptations given the coexistence of different beating cilia (coordinated, fast-, slow-, or non-beating cilia) on the same culture [3]. A full HD camera was used to record videos (resolution 1920 x 1080 pixels, 50 fps). In order to calculate the CBF, a Phyton script was developed. Accordingly, each image was divided into 100 independent subregions by using a 10 x10 grid. The average intensity in time was calculated for each subregion and the highest frequency components of the signal were extracted by using a discrete fourier transform. For each video, the top 10 subregions with highest CBF measured in Hz were used for further analysis. For each culture condition, three videos (>10 s each) were recorded and the distributions of the CBF were comparatively analyzed.

2.8 Statistical analysis

These analyses were performed in collaboration with Dr. SM Hauck and Dr. B. Schubert (secretome data), M. Ansari and Dr. H. Schiller (single cell data), A. Castelblanco (CBF), Dr. M. Irmler (microarray data) (Institute for Lung Health and Immunity and Comprehensive Pneumology Center; Helmholtz Zentrum Munich, Germany)

Clinical characteristics of patients:

Results were presented as median [quartiles].

TEER, WST-1, LDH, IF:

Specific NPs- and disease-related effects were analyzed via two-way ANOVA with Dunett' post-hoc testing. Representative 3D IF images were analyzed by applying the T-Test or two-way ANOVA, if applicable. Results were presented as mean ± SEM, with P-values < 5% considered as statistically significant.

CBF:

Comparisons were performed by using Kolmogorov–Smirnov Test with P-values adjusted by Benjamini–Hochberg Test for multiple testing correction.

Transcriptome data:

Data were statistically analyzed by using the statistical programming environment R (R Development Core Team), CarmaWeb for paired analyses according to the previously described methods or GraphPrism 8.2 [118]. Testing of differential gene expression were done by (paired) Limma T-Test with Benjamini-Hochberg Test for multiple testing correction. The gene datasets with a false discovery rate (FDR) < 10% was considered significant. Background of gene datasets (dabg) was detected and reduced using P-values < 5% in at least 50% of the samples in at least one of the treatment groups. Datasets of regulated genes were defined by raw P-values < 5%, a fold change gene expression ≥ 1.3 and z-score transformation > 2 (activation) or < -2 (inactivation). Pathway analyses were generated by QIAGEN's Ingenuity Pathway Analysis® (IPA®, QIAGEN Redwood City, www.qiagen.com/ingenuity) using Fisher`s Exact Test. Gene enrichment datasets were analyzed by Perseus platform. GO terms from

the GO biological Process 2021 platform derived from the Enrichr database was attached. GO terms were sorted by *P*-value.

Proteome data:

Protein ratios were calculated using pairwise ratio-based approach, with a background-based Student's T-Test as hypothesis test [119], resulting in ratios and corresponding significance values for the individual proteins. Peptide abundance values were normalized on total peptide amount. Only top-scoring identifications for each spectrum were included into the final database, by using a FDR < 1%. The final list of proteins satisfied a FDR < 5%.

Single cell data:

The generation of count matrices was performed by using the Drop-seq tools computational pipeline (v2.0, STAR v2.5.3a). The reads were aligned to the hg19 human reference genome. Downstream transcriptomic analysis was performed using the Scanpy package (v1.8.0). Statistical significance was calculated with the Wilcoxon rank-sum Test using the Python package scipy, and the *P*-values were adjusted with the Benjamini-Hochberg Test for multiple testing correction. The number of the GO Terms and the corresponding gene lists were retrieved from http://geneontology.org/.

3. Results

3.1 Clinical characteristics of patients included in the study

pHBECs cultures derived from n=6 COPD-IV patients undergoing lung transplantation and n=3 COPD-II patients with lung tumors undergoing major lung resections. The median age of the patients admitted with COPD-IV was 62.5 [56-64.5] years and with COPD-II 70 [64-70] years.

Five out of six patients with COPD-IV underwent double lung transplantation. Five patients presented at last clinical examination prior to lung transplantation a severely decreased lung function (predicted $FEV_1 < 20\%$, median 18.6 [14.4-26.5] %). All patients with end-stage lung disease denied a history of pulmonary hypertension or heart disease.

All patients undergoing lung transplantation were ex-smokers with a median smoking history of 35 [26.3-40] Pack Years. Median follow-up of patients undergoing lung transplantation was 12 months.

Clinical characteristics of the COPD patients included in the study are summarized in **Table 17**.

Pat. No.	Age	COPD stage	Pack years	Smoker status	Surgery	FEV_1 (%)	PAH	Heart disease	CMV	Follow up (mo.)
P1	62	IV	40	Ex	Double LTX	13.15	No	No	-	12
P2	66	IV	30	Ex	Single LTX	18.33	No	No	-	12
P3	63	IV	40	Ex	Double LTX	14.79	No	No	+	12
P4	50	III-IV	15	Ex	Double LTX	19.28	No	No	-	12
P5	58	IV	30	Ex	Double LTX	48	No	No	-	6
P6	64	IV	40	Ex	Double LTX	18.88	No	No	-	0
P7	70	II	40	Ex	Lobectomy	70.6	No	Yes	n.a.	>12
P8	64	I-II	n.a.	Active	Lobectomy	79	No	No	n.a.	4
P9	70	II	80	Ex	Pneumonectomy	59	No	No	n.a.	24

Table 17: Clinical characteristics of the COPD patients included in the study. Following parameters were assessed: age, COPD-stage, smoker status, surgery type, forced expiratory volume in 1 second (FEV_1, % predicted value), pulmonary artery hypertension (PAH), history of heart disease, cytomegalovirus infection status of the recipient (CMV) and follow-up (months).

3.2 Analysis of the response of the bronchial epithelium upon NP exposure

The main goal of the project was to analyze the functional and compositional changes of the healthy and diseased bronchial epithelium upon environmental NP exposure.

The experimental approach is illustrated in **Figure 12**.
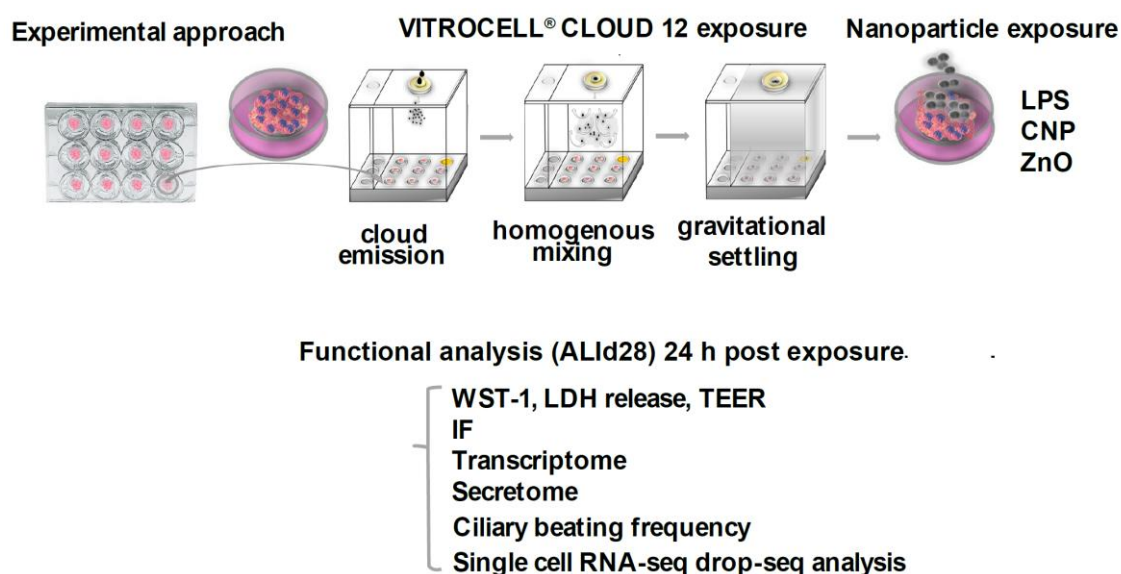
Figure 12: Experimental approach illustrating the long-term ALI pHBECs culture, consecutively challenged to environmental Nanoparticles (NPs) via the highly standardized preclinical VITROCELL® CLOUD 12 cell exposure system. LPS, Carbon soot surrogate NP (CNP) and Zinc Oxide were selected for NP exposure. Analysis post-exposure comprised functional assays (WST-1, LDH release, Transepithelial electrical resistance (TEER), Immunoflorescence (IF), ciliary beating frequencies of the multi-ciliated cells colonies) as well as transcriptome, secretome and single cell RNA-seq drop-seq analysis.

In summary, different aerosolized NP were realistically nebulized via VITROCELL® CLOUD 12 exposure system on the surface of the human bronchial epithelium at ALI. The chosen NPs (carbon soot surrogate nanoparticle/ CNP and ZnO) were selected as important components of the welding fume [12,120–123] present in high concentrations in industrial and heavily urbanized cities as a result of uncontrolled combustion processes. To highlight a potential dose-dependent response, two ZnO doses (ZnO low 0.14 cm^2/cm^2 and ZnO high 3.2 cm^2/cm^2) have been nebulized. For CNP, a repetitive nebulization (2x) has been used, since a single dose was not able to provoke significant cell compositional and functional changes. The analysis of cell composition and epithelial function post-exposure includes following steps:

i)   The toxin-induced effects on cell composition and function were comparatively analyzed via WST-1, LDH, TEER and IF.

ii)   The post-exposure changes were investigated at transcriptome and secretome level.

iii)   The SC-MCC differentiation axis was analyzed at single cell level.

iv)   The terminally end-differentiated MCC were functionally characterized by CBF analysis.

v)   Single cell analysis in freshly isolated and end-differentiated pHBECs at ALI was performed to highlight potential associations between the skewed cellular composition and the response upon NP exposure.

3.2.1 pHBECs ALI culture exposure to ZnO

3.2.1.1 Cytotoxicity, barrier integrity and viability (LDH release, TEER and WST-1)

The exposure to ubiquitously relevant, moderate ZnO doses (0.14 cm^2/cm^2 ZnO) was illustrated in **Figure 13**.
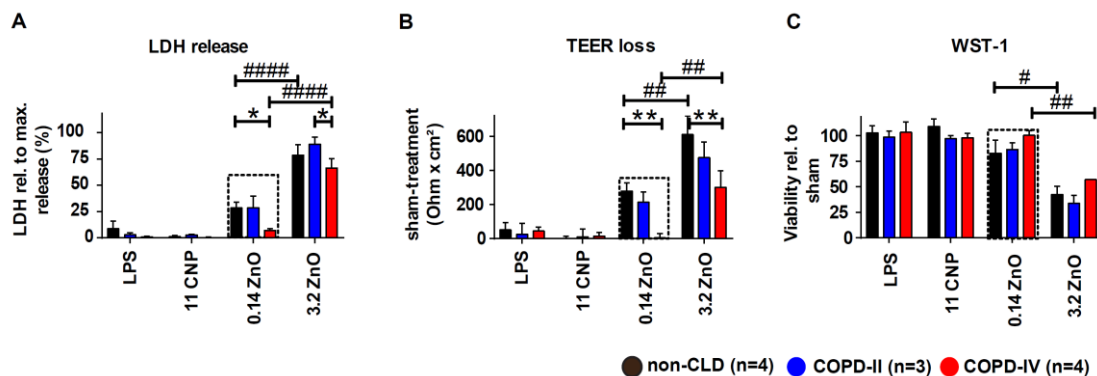
Figure 13: Analysis of membrane integrity **(A)**, barrier integrity loss **(B)** and metabolic cell viability **(C)** of the pHBECs cultures derived from non-CLD, COPD-II and COPD-IV patients 24 hours after NP exposure using lactate dehydrogenase (LDH release) assay, transepithelial electrical resistance (TEER) and tetrazolium salt (WST-1) assay. Results were presented as mean ± SEM with *P*-values < 5% considered as statistically significant. Specific NPs- and disease-related effects were analyzed via two-way ANOVA with Dunett' post-hoc testing. * Significances within same NP exposure group, # significances within different disease states.

Exposure to moderate ZnO was characterized by pronounced disease-stage specific effects in non-CLD and COPD-II derived pHBECs: next to a 4-fold increase of LDH release (ΔLDH 28.45 (ZnO, non-CLD); 28.49 (ZnO, COPD-II); 8.60 (LPS, non-CLD)), and a significant loss of cell barrier integrity, (i.e. membrane resistance (ΔTEER loss 278 (ZnO, non-CLD); 212 (ZnO, COPD-II) Ohm x cm^2)) we observed a pronounced reduction in metabolic cell activity (ΔWST-1 82.6 (ZnO, non-CLD); 86.5 (ZnO, COPD-II)), all together matching the clinical picture of ZnO-induced airway injury (**Figure 13 A-C**). In comparison to the non-CLD and COPD-II cultures, the COPD-IV bronchial epithelium revealed an increased resilience towards ZnO exposure mirrored in a reduced LDH release (ΔLDH 7.28, (COPD-IV), 28.49 (COPD-II), 28.44 (non-CLD)) and barrier integrity loss (ΔTEER loss 3.2 Ohm x cm^2 (COPD-IV), 212 Ohm x cm^2 (COPD-II), 277 Ohm x cm^2 (non-CLD), **Figure 13 B**) with a concomitant preserved metabolic cell viability (ΔWST-1 101.4% (ZnO, COPD-IV), 86.5% (COPD-II), 82.6% (non-CLD)). In particular, exposure to ZnO revealed a dose-dependent response with a significantly increased LDH release upon high ZnO exposure in non-CLD and COPD-II pHBECs (ΔLDH 78.5 (non-CLD); 88.9 (COPD-II)) when compared to COPD-IV pHBECs (ΔLDH 66.6 (COPD-IV)). This response was accompanied by a significant loss of cell barrier integrity (ΔTEER loss 609.8 (non-CLD); 474.5 (COPD-II) Ohm x cm^2, **Figure 13 B**). Exposure to high ZnO doses induced a decrease in cell viability independent of disease stage (ΔWST 42.5% (non-CLD); 41.6% (COPD-II); 45.8% (COPD-IV)).

Altogether, exposure to maximal ZnO doses induced a reduced LDH release (ΔLDH 66.6 (COPD-IV)) and loss of cell barrier integrity (ΔTEER loss 299.7 (COPD-IV) Ohm x cm^2) and an almost similar reduction in metabolic cell activity (ΔWST-1 45.8% (ZnO, COPD-IV)) when compared to non-CLD and COPD-II cultures.

3.2.1.2 Immunofluorescence

Exposure to moderate dose of ZnO NPs revealed a stable number of MCC in exposed non-CLD pHBECs (Ac.-Tub$^+$ 47.01±2.80% (ZnO, non-CLD)), when compared to the decreased number of MCC in COPD-II cultures (20.35±14.07% (ZnO, COPD-II)). The number of SC remains almost unchanged in non-CLD and COPD-II cultures (MUC5AC$^+$ 5.17±2.43 (ZnO, non-CLD); 6.04±2.18 (ZnO, COPD-II)) and CC10$^+$ cells (CC10$^+$ 16.58±3.32% (ZnO, non-CLD); 18.49±5.53% (ZnO, COPD-II)) on ALId28 (**Figure 14**).
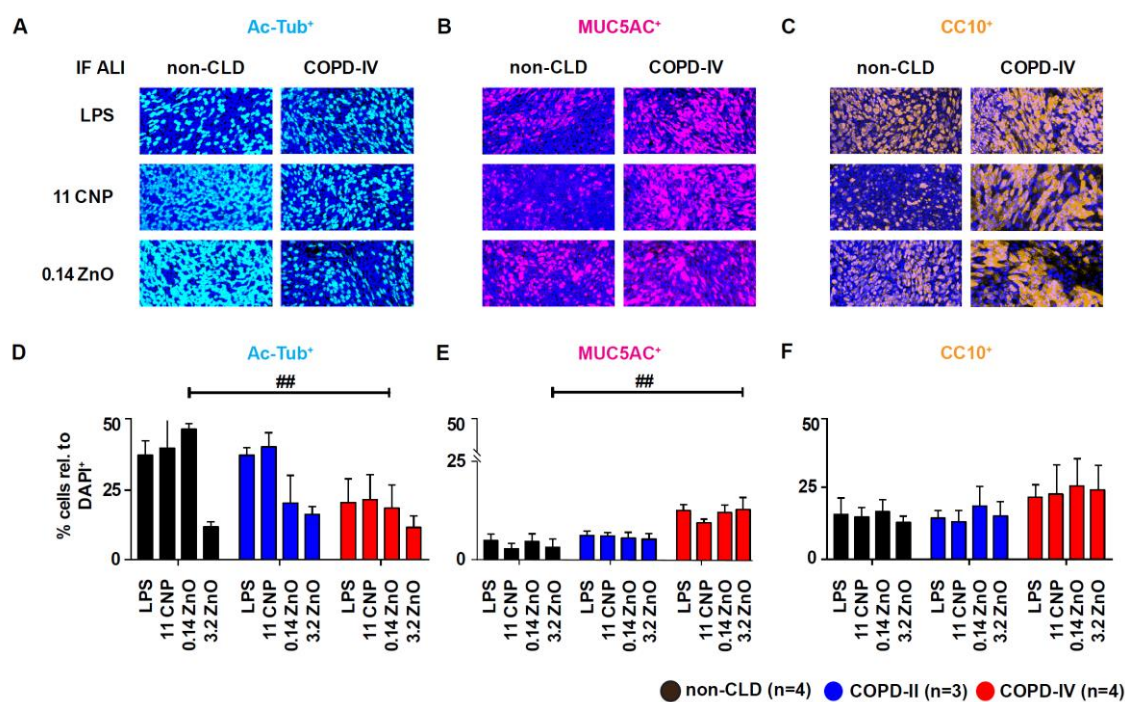
Figure 14: (A-C) Representative 3D IF and **(D-F)** quantification of confocal IF images of the NP exposed ALI cultures, reflecting an increased resilience of COPD-IV pHBECs associated with a hypersecretory oligo-ciliated cell phenotype (increased amount of secretory cells, decreased amount of multi-ciliated cells). Three images were quantified for each culture condition. Results were presented as mean ± SEM with *P*-values < 5% considered as statistically significant. Specific NPs- and disease-related effects were analyzed via two-way ANOVA with Dunett' post-hoc testing. [#]Significances within different disease states

Moreover, the reduced number of MCC (oligo-ciliated phenotype) in COPD-IV cultures (Ac.-Tub$^+$ 18.5±11.9% (ZnO, COPD-IV)) was accompanied by an increased number of secretory (MUC5AC$^+$ 12.8±2.9% (ZnO, COPD-IV) and CC10$^+$ (CC10$^+$ 25.5±7.4% (ZnO, COPD-IV)) cells when compared to non-CLD and COPD-II cultures (**Figure 14 D-F**).

Given the overall lower number of cells in COPD-IV cultures, the compositional changes were more reduced in COPD-IV in comparison to non-CLD and COPD-II cultures, with a relevant cell reduction of MCC.

3.2.1.3 Transcriptome and secretome analysis

Transcriptome analysis upon moderate ZnO exposure revealed an increased gene signaling involved in metal ion homeostasis in COPD-IV cultures (MT1IH, MT1IF, MT1IM, CKMT1B, MT1L, MT1IP) together with increased mineral absorption processes at the level of the cell membrane (KEGG: hsa04978).

The increased expression of the toxicity protecting metallothioneins illustrates the efficiency of the absorption mechanisms at the level of COPD-IV bronchial epithelium.

The expression of genes encoding metallothioneins is comparatively summarized in **Table 18**.

DEG	COPD-IV		non-CLD	
	P-value	FC	*P*-value	FC
MT1H	2.25E-03	2.65		
MT1F	2.90E-03	2.24		
MT1M	1.97E-03	2.05		
CKMT1B	5.77E-03	1.53		
MT1L	2.86E-02	1.53		
CKMT1A	1.58E-02	1.34	1.87E-02	1.63
MT1HL1	4.71E-02	1.32	4.24E-02	2.04
MT1IP	2.45E-02	1.32		

Table 18: Differential expression of metal toxicity protecting metallothioneins (MT1-) derived from bulk transcriptome analysis 24 hours after moderate ZnO exposure (0.14 cm^2/cm^2) of COPD-IV and non-CLD cultures. Datasets of regulated genes were defined by raw *P*-values $< 5\%$ by using a fold change (FC) gene expression filter ≥ 1.3. DEG - differentially expressed genes.

Enrichment analysis upon moderate ZnO exposure revealed a panel of upstream regulators involved in cell differentiation axis towards a hypersecretory phenotype (SPDEF, FOXO1, IL-17C, PPRC1, RELA, LAMC1, IRF3).

The secretory fate of ZnO-challenged pHBECs in COPD-IV cultures is complemented by an aberrant expression of genes involved in cilium organization and movement (GO: 0003341, GO: 0001539, GO: 0044782, GO: 0007018, **Table 19**).

Upstream Regulator	FC	z-score transformation	P-value
SPDEF*,$	1.2	3.04	1.81E-05
IL-17C#,$	-1.3	2.61	2.20E-04
LAMC1	-1.1	2.21	3.50E-04
PPRC1	-1.1	2.41	2.70E-02
RELA	1.2	2.3	3.00E-02
FOXO1*,$	1.1	3.23	3.40E-02
SMAD2	-1.1	-2.46	1.70E-04
RLIM	-1.1	-2	8.80E-04
SMAD4	1.1	-2.19	1.30E-03
SMARCA4	1.2	-2.83	3.10E-03
NRF1*,#	-1.1	-2.01	5.60E-03
TGFB3*,#	1.2	-2.87	8.60E-03
TGFB1*,#	1.1	-2.85	3.80E-02

Table 19: Bulk transcriptome in ZnO (0.14 cm^2/cm^2) challenged COPD-IV vs non-CLD derived cultures with focus on significantly expressed upstream regulators derived from Ingenuity Pathway Analysis®. Marked upstream regulators indicates *cell proliferation/ differentiation, #immune response, and $primary secretory fate. Datasets of regulated genes were defined by raw P-values < 5% by using a fold change (FC) gene expression filter ≥ 1.3 and a z-score transformation > 2 or < -2 (z-score > 2 = activation; z-score < -2 = inactivation). DEG - differentially expressed genes.

The exposure of non-CLD pHBECs to moderate ZnO doses reveals a gene cluster involved in epithelial differentiation as well as cilium movement. The top 30 upregulated differentially expressed genes in ZnO-exposed non-CLD cultures define a central cluster involved in epithelial cell differentiation axis and keratinization ([DSP, SPRR2E, SPRR2F, SPRR3, GRHL3, OVOL1, POU2F3, KLK7, KRT9, SCEL, STS, SPRR2A, SPRR2B, SPRR1A, SPRR1B, ZNF750, SPRR2D], **Table 20**) as reflected in the Gene Ontology terms (**Figure 15**).

Non-CLD ZnO vs non-CLD sham   **Non-CLD ZnO vs non-CLD sham**

Top 30 upregulated genes   **Top 30 downregulated genes**

Gene symbol	P-value	BH	FC≥1.3, p<0.05, dabg	Gene symbol	P-value	BH	FC≥1.3, p<0.05, dabg
SPRR3	0.00005	0.49645	32.74	CNGA4	0.04511	0.79910	-8.13
SPRR2A	0.00102	0.79910	16.90	CFAP157	0.03717	0.79910	-7.76
KLK7	0.02682	0.79910	16.54	CCDC65	0.04881	0.79910	-6.91
C15orf48	0.00570	0.79910	9.18	CYP2F1	0.00014	0.79910	-6.51
A2ML1	0.01710	0.79910	9.07	FAM166B	0.04115	0.79910	-6.44
MUC21	0.00615	0.79910	8.60	TMEM212	0.04629	0.79910	-6.40
SPRR2D	0.00225	0.79910	6.81	AGBL2	0.04694	0.79910	-6.27
SERPINB7	0.00487	0.79910	6.53	DNAAF1	0.02845	0.79910	-5.64
IFIT1	0.01715	0.79910	6.38	MROH9	0.04937	0.79910	-5.53
ALPL	0.00306	0.79910	6.16	SLC23A1	0.00096	0.79910	-5.15
IFI44L	0.02027	0.79910	6.08	DNAH5	0.04442	0.79910	-5.02
SPRR2B	0.00944	0.79910	5.84	SCGB3A1	0.00475	0.79910	-4.92
MX2	0.00380	0.79910	5.78	C1orf194	0.03803	0.79910	-4.90
KRT24	0.01988	0.79910	5.45	CCDC181	0.01908	0.79910	-4.78
IFIT2	0.01148	0.79910	5.07	C2orf73	0.03273	0.79910	-4.70
SPRR2E	0.00765	0.79910	5.01	PROS1	0.00032	0.79910	-4.60
IFIT3	0.02776	0.79910	4.64	ST3GAL6	0.00486	0.79910	-4.56
CRYAB	0.00004	0.49645	4.53	TSNAXIP1	0.02467	0.79910	-4.52
CEACAM7	0.04327	0.79910	4.50	TCTE1	0.02498	0.79910	-4.49
OAS1	0.00059	0.79910	4.45	RP1	0.01462	0.79910	-4.41
SCEL	0.00150	0.79910	4.30	CDHR4	0.04091	0.79910	-4.27
CLIC3	0.02465	0.79910	4.25	IQCG	0.04570	0.79910	-4.23
MX1	0.01545	0.79910	4.22	VWA3A	0.00991	0.79910	-4.21
SERPINB2	0.00257	0.79910	4.15	PIH1D2	0.04288	0.79910	-4.18
ELOVL6	0.01178	0.79910	3.88	DYDC2	0.03810	0.79910	-4.16
NCCRP1	0.01072	0.79910	3.84	DNAJB13	0.02564	0.79910	-4.15
CD68	0.00150	0.79910	3.84	ANPEP	0.02505	0.79910	-4.12
SPRR2F	0.01686	0.79910	3.81	NME9	0.02143	0.79910	-4.10
SAA1	0.00154	0.79910	3.47	SPATA18	0.03778	0.79910	-4.06
PGLYRP3	0.00066	0.79910	3.39	KLHL6	0.02467	0.79910	-4.03

Table 20: Top 30 upregulated (marked in red) and downregulated (marked in blue) genes derived from bulk transcriptome analysis 24 hours after ZnO (0.14 cm^2/cm^2) exposure of non-CLD cultures. Testing of differential gene expression was done by (paired) Limma T-Test with Benjamini-Hochberg Test (BH Test) for multiple testing correction. Background of the gene datasets (dabg) was detected and reduced using P-values < 5%. Datasets of regulated genes were defined by raw P-values < 5% by using a fold change (FC) gene expression filter ≥ 1.3.
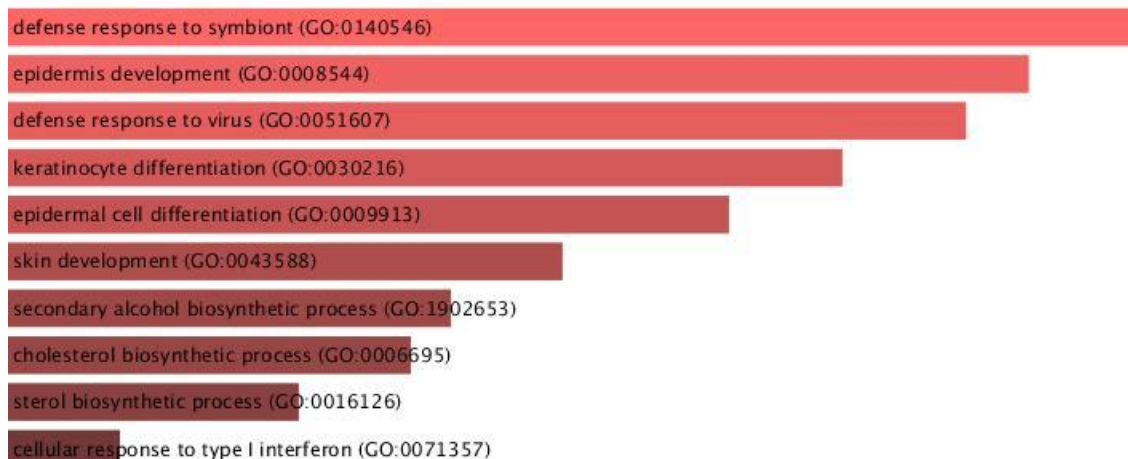
Figure 15: Top 10 significant *P*-values for Gene ontology (GO) terms derived from the upregulated genes (n=630) of the bulk transcriptome 24 hours after ZnO (0.14 cm^2/cm^2) exposure, reflecting a significant signaling of epithelial differentiation pathways in ZnO exposed non-CLD cultures. For each pathway the GO term derived from the GO biological Process 2021 specified in the online Enrichr database was attached. GO terms were sorted by *P*-value ranking.

Analogously, the exposure of COPD-IV pHBECs to moderate ZnO NPs reveals a gene cluster involved in epithelial differentiation ([TGM1, SPRR2E, SPRR2F, SPRR3, OVOL1, GRHL1, FABP5, KRT14, SPRR2A, SPRR2B, SPRR1A, SPRR1B, ZNF750, SPRR2D], GO:0009913, GO:0008544, GO:0030216) as well as regulation of cilium movement ([DNAI2, CFAP100, RSPH4A, CABYR, DNAAF1, TTC29, CFAP53, DNAI1], GO:0003341, GO:0003352). The gene enrichment score derived from the Ingenuity Pathway Analysis® in COPD-IV pHBECs exposed to ZnO is illustrated in **Figure 16**.
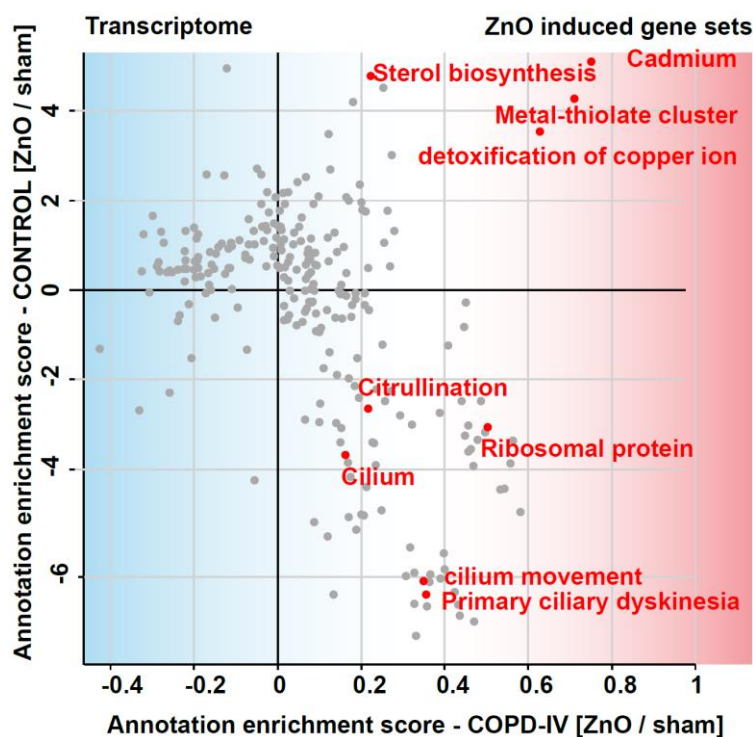
Figure 16: Gene enrichment score derived from the Ingenuity Pathway Analysis® of the bulk transcriptome in non-CLD vs COPD-IV cultures exposed to moderate ZnO doses (0.14 cm^2/cm^2), reflecting the overrepresentation of pathways involved in aberrant cilium organization and movement upon NP exposure in COPD-IV cultures. Gene enrichment datasets were comparatively analyzed by Perseus computational platform.

The top 30 upregulated differentially expressed genes in ZnO-exposed COPD-IV and the top 10 Gene Ontology terms are summarized in **Table 21** and **Figure 17**.

COPD-IV ZnO vs COPD-IV sham
Top 30 upregulated genes

Gene symbol	*P*-value	BH	FC≥1.3 p<0.05 dabg
SPRR3	0.00235	0.72945	5.09
SPRR2A	0.00029	0.72945	3.65
CRYAB	0.02931	0.72945	3.39
MT1H	0.00225	0.72945	2.65
IFI44L	0.00783	0.72945	2.48
C10orf107	0.02288	0.72945	2.46
PIFO	0.01900	0.72945	2.44
SPRR2D	0.00199	0.72945	2.31
SPRR1A	0.00011	0.61377	2.30
MUC13	0.02597	0.72945	2.26
TPPP3	0.02387	0.72945	2.25
C9orf24	0.01163	0.72945	2.25
LDLRAD1	0.03906	0.72945	2.24
MT1F	0.00290	0.72945	2.24
SPRR1B	0.00003	0.61377	2.20
OMG	0.00415	0.72945	2.16
IL1RN	0.01166	0.72945	2.12
CCL20	0.03275	0.72945	2.11
DTHD1	0.03782	0.72945	2.10
HIST1H2BM	0.00068	0.72945	2.10
UCHL1	0.01871	0.72945	2.09
S100A8	0.02611	0.72945	2.09
CCDC65	0.00711	0.72945	2.06
MT1M	0.00197	0.72945	2.05
C9orf116	0.02053	0.72945	2.02
Hsacirc004157	0.00009	0.61377	2.01
C20orf85	0.01406	0.72945	2.01
PI3	0.00958	0,72945	1.99
KCNE1	0.03993	0.72945	1.99
IQUB	0.02855	0.72945	1.99

COPD-IV ZnO vs COPD-IV sham
Top 30 downregulated genes

Gene symbol	*P*-value	BH	FC≥1.3 p<0.05 dabg
MAS1L	0.00138	0.72945	-1.78
HCST	0.01452	0.72945	-1.75
MEP1B	0.00549	0.72945	-1.75
CST6	0.01704	0.72945	-1.74
PIEZO1	0.00458	0.72945	-1.74
FAM101B	0.00935	0.72945	-1.73
TRDN	0.00166	0.72945	-1.72
hsa_circ0001338	0.03407	0.72945	-1.72
DIRC1	0.03098	0.72945	-1.72
AP4S1	0.00299	0.72945	-1.72
CYLC2	0.01381	0.72945	-1.72
SCUBE1	0.03151	0.72945	-1.71
SLC29A2	0.00119	0.72945	-1.71
LINC00482	0.00102	0.72945	-1.71
ROS1	0.01038	0.72945	-1.70
PLAT	0.03916	0.72945	-1.70
TSPAN2	0.00143	0.72945	-1.70
GTSF1L	0.00542	0.72945	-1.70
ABCC9	0.00164	0.72945	-1.69
QSOX2	0.00128	0.72945	-1.69
MARVELD2.j	0.00445	0.72945	-1.69
PVRL3	0.00152	0.72945	-1.68
IGFBP5	0.01110	0.72945	-1.68
RP11-35G9.5	0.01062	0.72945	-1.67
EPHA7	0.01056	0.72945	-1.67
APOE	0.01942	0.72945	-1.67
SEMA3G	0.00334	0.72945	-1.67
hsa_circ0003150	0.01126	0.72945	-1.66
CD5	0.00130	0.72945	-1.66
NETO1	0.00973	0.72945	-1.65

Table 21: Top 30 upregulated (marked in red) and downregulated (marked in blue) genes derived from bulk transcriptome analysis 24 hours after ZnO (0.14 cm^2/cm^2) exposure of COPD-IV cultures. Testing of differential gene expression was done by (paired) Limma T-Test with Benjamini-Hochberg Test (BH Test) for multiple testing correction. Background of the gene datasets (dabg) was detected and reduced using *P*-values < 5%. Datasets of regulated genes were defined by raw *P*-values < 5% by using a fold change (FC) gene expression filter ≥ 1.3.
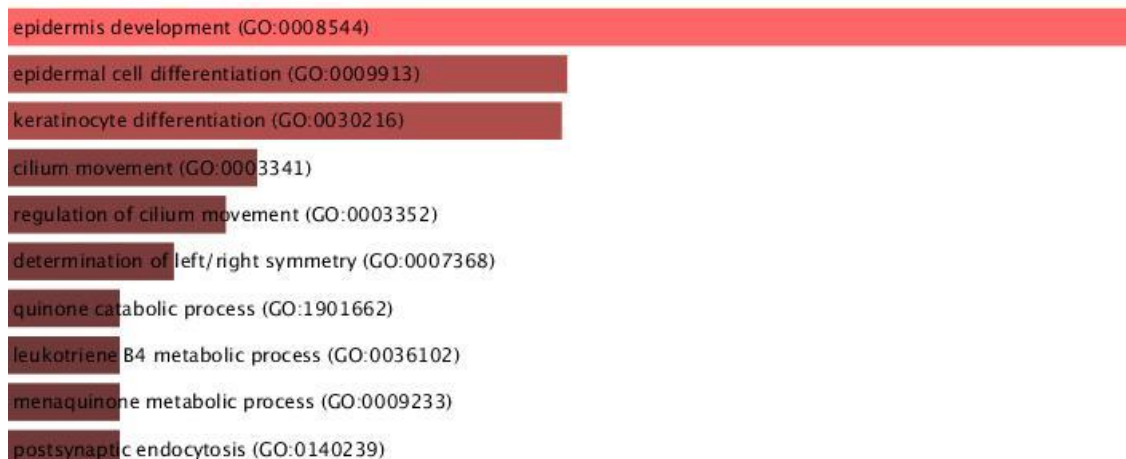
Figure 17: Top 10 significant *P*-values for Gene ontology (GO) terms derived from the upregulated genes (n=567) of the bulk transcriptome 24 hours after ZnO (0.14 cm^2/cm^2) exposure, reflecting a significant signaling of epithelial cell differentiation pathways and regulation of cilium movement in ZnO challenged COPD-IV cultures. For each pathway the GO term derived from the GO biological Process 2021 specified in the online Enrichr database was attached. GO terms were sorted by *P*-value ranking.

Secretome analysis

In accordance with the transcriptome data, secretome analysis revealed a downregulation of proteins involved in ciliary transport, assembly and movement in COPD-IV derived pHBECs upon exposure to moderate ZnO doses (**Table 22**).

In contrast, ZnO exposed non-CLD cultures were characterized by common RNA-based enzymatic processes (GO:0006396, GO:0000993, GO:0006397, GO:0003723), organelle organization- (GO:0006996), protein binding- (GO:0005515) and cellular component biogenesis processes (GO:0044085, GO:0071840).

No.	GO term	Secretome pathway enrichment analysis COPD-IV ZnO vs COPD-IV sham	*P*-value
0	GO:0006996	organelle organization	2.80E-13
1	GO:0044085	cellular component biogenesis	1.74E-11
2	GO:0071840	cellular component organization or biogenesis	5.19E-11
3	GO:0022607	cellular component assembly	7.32E-09
4	GO:0016043	cellular component organization	1.34E-08
5	GO:0051641	cellular localization	2.86E-08
6	**GO:0042073**	**intraciliary transport***	8.23E-08
7	GO:0033036	macromolecule localization	3.07E-07
8	GO:0031503	protein-containing complex localization	3.15E-07
9	GO:0003723	RNA binding	1.12E-06
10	GO:0070925	organelle assembly	2.13E-06

11	GO:0046907	intracellular transport	2.52E-06
12	GO:0030705	cytoskeleton-dependent intracellular transport	2.53E-06
13	**GO:0007017**	**microtubule-based process***	6.71E-06
14	GO:0032543	mitochondrial translation	8.86E-06
15	GO:0016071	mRNA metabolic process	1.04E-05
16	**GO:0010970**	**transport along microtubule***	1.25E-05
17	**GO:0060271**	**cilium assembly***	2.40E-05
18	**GO:0035735**	**intraciliary transport involved in cilium assembly***	2.55E-05
19	**GO:0099111**	**microtubule-based transport***	3.13E-05
20	**GO:0044782**	**cilium organization***	3.49E-05

Table 22: Pathway enrichments analysis derived from secretome data of COPD-IV cultures exposed 24 hours to moderate ZnO NPs (0.14 cm^2/cm^2), revealing significantly abundant proteins involved in cilium biosynthesis, organization and movement (highlighted in bold). * Pathways observed only in COPD-IV cultures exposed to ZnO and absent in non-CLD exposed cultures. GO terms were sorted by *P*-value ranking. Raw *P*-values < 5% were considered significant.

3.2.1.4 Ciliary beating frequency analysis

Figure 18: Analysis of distribution of ciliary beating frequencies (CBF, Hz) in non-CLD (n=2), COPD-II (n=2) and COPD-IV (n=2) cultures at baseline level (sham, **A**) and upon moderate ZnO (0.14 cm^2/cm^2) exposure (**B**), revealing significant disease-specific changes with a pathologic (biphasic) CBF spectrum at baseline level and a monophasic spectrum with increased CBF upon ZnO exposure in COPD-IV cultures. CBF was determined by using a modified ciliaFA protocol[3] upon calculation of average intensity in time and extraction of the highest signal frequencies by using a discrete fourier transform. For each condition, 3 videos (>10 s each) and the top 10 highest CBF were recorded. Comparative analysis of CBF was performed by Kolmogorov–Smirnov Test with *P*-values adjusted by Benjamini–Hochberg multiple testing correction.

Basically, the spectrum of CBF varies in healthy bronchial cultures between 7 and 16 Hz [81]. Accordingly, our non-CLD cultures present a physiologic distribution of CBF between 5 and 17 Hz. Analogously, unexposed COPD-II cultures presented a similar CBF distribution as non-CLD cultures, however the CBF spectrum was lower.

Unexposed COPD-IV cultures presented a pathologic biphasic CBF spectrum due to the presence of low-beating and high-beating MCC colonies. The distribution of CBF in unexposed COPD-IV cultures was significantly different in comparison to the physiologic pattern observed in unexposed non-CLD and COPD-II cultures.

Exposure to moderate ZnO NPs leads to a biphasic CBF distribution in non-CLD and COPD-II cultures due to the presence of hypermotile cilia with high frequencies (between 12 and 20 Hz), as illustrated in **Figure 18**. COPD-IV exposed cultures are characterized by a pathologic spectrum of beating frequencies with predominantly higher frequencies between 15 and 20 Hz, suggesting an aberrant NP-induced activation of MCC, which was also reflected in the transcriptome and secretome data of ZnO exposed COPD-IV cultures presented above.

3.2.2 pHBECs ALI culture exposure to LPS

3.2.2.1 Cytotoxicity, barrier integrity and viability (LDH release, TEER and WST-1)

Exposure to 1mg/ml LPS led to an unchanged LDH release, membrane integrity and viability in healthy, COPD-II und COPD-IV cultures. In addition, no significant changes in comparison to moderate ZnO exposure were observed. These findings suggest that LPS as inflammagenic pollutant does not affect pHBECs viability and barrier function at selected dose (**Figure 13**).
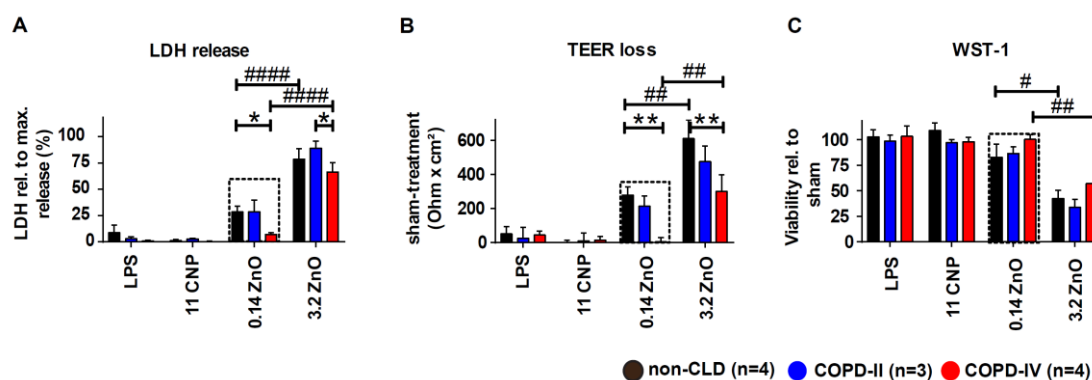
Figure 13: Analysis of membrane integrity (**A**), barrier integrity loss (**B**) and metabolic cell viability (**C**) of the pHBECs cultures derived from non-CLD, COPD-II and COPD-IV patients 24 hours after NP exposure using lactate dehydrogenase (LDH release) assay, transepithelial electrical resistance (TEER) and tetrazolium salt (WST-1) assay. Results were presented as mean ± SEM with *P*-values < 5% considered as statistically significant. Specific NPs- and disease-related effects were analyzed via two-way ANOVA with Dunett' post-hoc testing. * Significances within same NP exposure group, # significances within different disease states.

3.2.2.2 Immunoflorescence

Confocal IF stainings in healthy and COPD-II cultures revealed that relative frequency of MCC and SC was almost similar when comparing LPS exposed with unexposed pHBECs cultures (**Figure 14**). Moreover, LPS exposed COPD-II pHBECs were characterized by a similar expression of MUC5AC$^+$ cells (6.6±1.5%) and MCC (37.6±3.8%) when compared to the exposed healthy cultures (MUC5AC$^+$ cells 5.4±2.0%, MCC 37.6±7.3%), whereas COPD-IV cultures presented a decreased number of MCC (20.6±12.1%) and increased number of SC (MUC5AC$^+$ 13.1±2.2%, CC10$^+$ 21.5±3.3%).
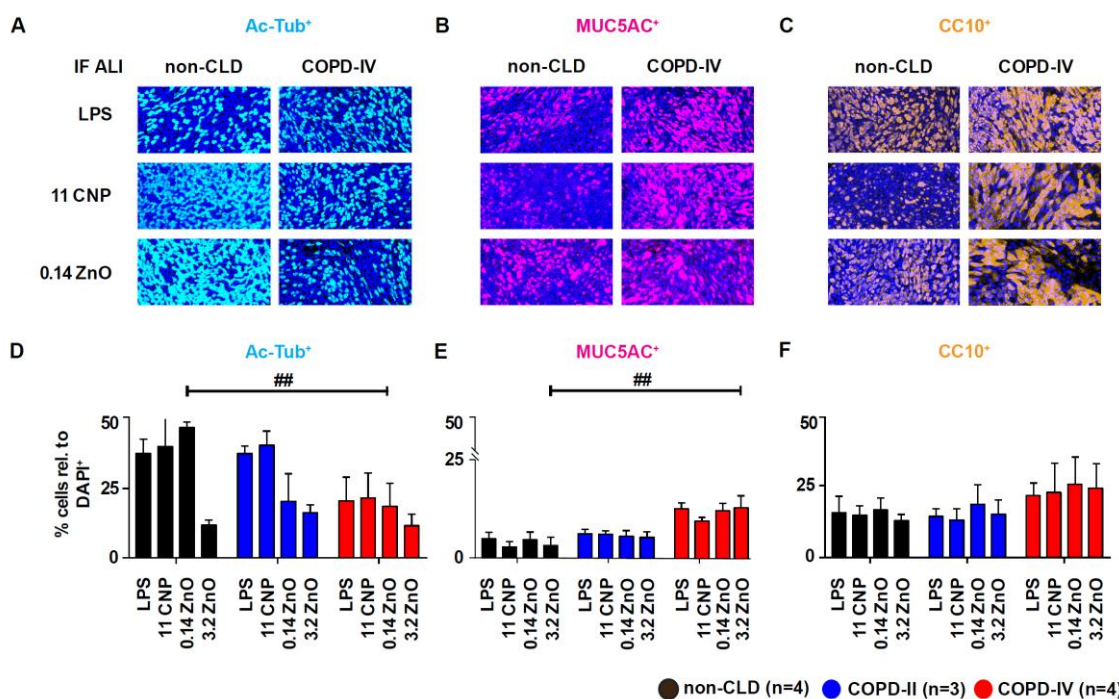
Figure 14: (A-C) Representative 3D IF and **(D-F)** quantification of confocal IF images of the NP exposed ALI cultures, reflecting an increased resilience of COPD-IV pHBECs associated with a hypersecretory oligo-ciliated cell phenotype (increased amount of secretory cells, decreased amount of multi-ciliated cells). Three images were quantified for each culture condition. Results were presented as mean ± SEM with *P*-values < 5% considered as statistically significant. Specific NPs- and disease-related effects were analyzed via two-way ANOVA with Dunett' post-hoc testing. $^\#$Significances within different disease states

3.2.2.3 Transcriptome and secretome analysis

Despite a reduced overall cell amount in COPD-IV cultures, common mechanisms upon LPS-exposure have been observed in both non-CLD and COPD-IV derived pHBECs. This aspect is mirrored in the upregulation of common inflammatory pathways (e.g. IL-17A) involved in cell differentiation towards a hypersecretory phenotype together with an aberrant regulation of cilium movement (hsa04657).

The main proinflammatory pathways upregulated upon LPS exposure in non-CLD exposed cultures derived from n=462 upregulated genes are illustrated in **Figure 19**.

Figure 19: Top 10 significant *P*-values for Gene ontology (GO) terms derived from the upregulated genes (n=462) of the bulk transcriptome 24 hours after LPS (1 mg/ml) exposure of non-CLD cultures, reflecting a significant signaling of proinflammatory pathways. For each pathway the GO term derived from the GO biological Process 2021 specified in the online Enrichr database was attached. GO terms were sorted by *P*-value ranking.

The top 30 upregulated and downregulated genes in the transcriptome analysis of the LPS exposed non-CLD cultures reflecting the above-mentioned pathways are illustrated in **Table 23**.

Non-CLD LPS vs non-CLD sham

Top 30 upregulated genes

Gene symbol	*P*-value	BH	FC≥1.3, p<0.05, dabg
SAA1	5.9E-11	1.1E-06	12.13
SAA2	1.0E-10	1.1E-06	11.80
SLC26A4	2.6E-08	0.00011	10.22
PI3	2.9E-10	2.1E-06	9.33
CCL20	1.2E-07	0.00031	6.47
UBD	4.5E-07	0.00089	5.74
FCGBP	2.0E-08	0.00010	5.40
LCN2	3.2E-07	0.00068	5.21
TNFAIP2	6.6E-08	0.00020	4.68
VNN2	6.4E-08	0.00020	4.66
SERPINA3	0.00001	0.00757	4.41
FCGBP	1.5E-07	0.00036	4.39
PDZK1IP1	6.9E-07	0.00123	3.52
CXCL6	2.0E-06	0.00308	3.35
ZG16B	1.3E-06	0.00220	3.31
CFB	3.2E-06	0.00461	3.11
ALPL	0.00001	0.00726	3.01

Non-CLD LPS vs non-CLD sham

Top 30 downregulated genes

Gene symbol	*P*-value	BH	FC≥1, p<0.05, dabg
SLC23A1	0.0000	0.0126	-2.82
MEIOB	0.0002	0.1674	-2.16
DPP4	0.0004	0.2142	-2.14
ANPEP	0.0004	0.2081	-2.09
GCOM1	0.0039	0.5639	-2.05
KBTBD3	0.0004	0.2081	-2.05
OTUD3	0.0011	0.3607	-2.00
ZNF91	0.0008	0.3045	-2.00
ADAM29	0.0006	0.2686	-1.97
TNFSF4	0.0069	0.6670	-1.96
LMO3	0.0007	0.2810	-1.96
ATP6V1B1	0.0018	0.4403	-1.92
SLC10A5	0.0012	0.3607	-1.92
CCDC93	0.0010	0.3510	-1.92
EFCAB6	0.0011	0.3607	-1.91
ERICH5	0.0012	0.3607	-1.89
ARHGAP11B	0.0160	0.8109	-1.88

SOD2	0.00001	0.01316	2.80	hsa_circ0002308	0.0046	0.5941	-1.87
DUOX2	0.00057	0.26860	2.79	DCLK1	0.0014	0.4136	-1.87
KYNU	0.00006	0.06274	2.78	FAM180A	0.0016	0.4287	-1.83
CXCL8	0.00004	0.04277	2.60	C1orf158eAug10	0.0022	0.5037	-1.82
CSF3	0.00010	0.08643	2.53	IFNA13	0.0074	0.6864	-1.81
SPRR2E	0.00013	0.10334	2.50	SETD7	0.0017	0.4329	-1.81
IRAK3	0.00004	0.04121	2.45	RP11-351M8.2	0.0023	0.5048	-1.80
BCL2A1	0.00028	0.17911	2.43	ABI3BP	0.0026	0.5306	-1.79
LTF	0,00015	0.11128	2.41	BEST1	0.0036	0.5586	-1.79
SPRR2A	0,00060	0.26860	2.40	FAM131B	0.0028	0.5406	-1.79
SPRR2D	0.00017	0.12903	2.33	IL17RD	0.0023	0.5037	-1.78
CRACR2	0.00008	0.07024	2.32	SUMO4	0.0022	0.5037	-1.78
DOC2B	0.00011	0.09491	2.28	FGF11	0.0029	0.5467	-1.78

Table 23: Top 30 upregulated (marked in red) and downregulated (marked in blue) genes derived from bulk transcriptome analysis 24 hours after LPS (1 mg/ml) exposure of non-CLD cultures. Testing of differential gene expression was done by (paired) Limma T-Test with Benjamini-Hochberg Test (BH Test) for multiple testing correction. Background of the gene datasets (dabg) was detected and reduced using *P*-values < 5%. Datasets of regulated genes were defined by raw *P*-values < 5% by using a fold change (FC) gene expression filter ≥ 1.3.

Analogously, the most frequently regulated pathways reported in COPD-IV cultures exposed to LPS, were linked to classical proinflammatory mechanisms involved in antimicrobial defense (**Figure 20**).
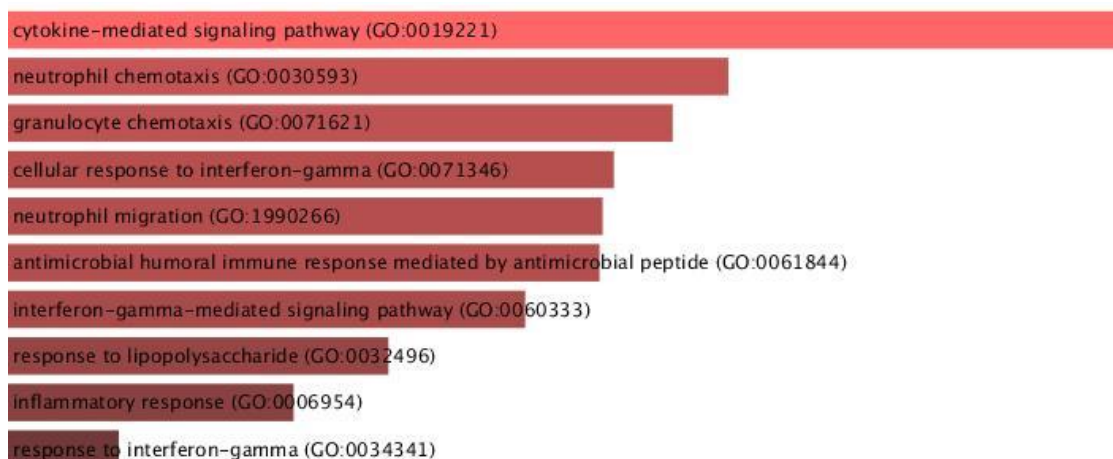
Figure 20: Top 10 significant *P*-values for Gene ontology (GO) terms derived from the upregulated genes (n=461) of the bulk transcriptome 24 hours after LPS (1 mg/ml) exposure of COPD-IV cultures, reflecting a significant signaling of classical proinflammatory pathways. For each pathway the GO term derived from the GO biological Process 2021 specified in the online Enrichr database was attached. GO terms were sorted by *P*-value ranking.

These findings were in line with the enrichment analysis of LPS-exposed COPD-IV cultures that revealed classical defense mechanisms triggered by proinflammatory pollutants (e.g. MHC class II complex, proteasome core complex, **Figure 21**).
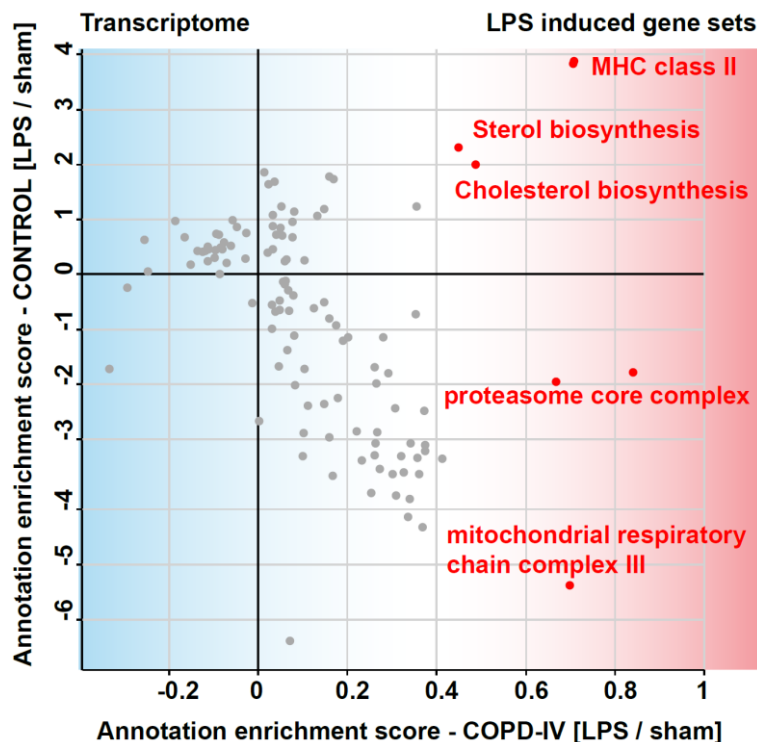
Figure 21: Gene enrichment score derived from the Ingenuity Pathway Analysis® of the bulk transcriptome in non-CLD vs COPD-IV cultures exposed to LPS (1 mg/ml), reflecting common proinflammatory innate immunity pathways upon LPS exposure in COPD-IV cultures. Gene enrichment datasets were comparatively analyzed by Perseus computational platform.

The top 30 upregulated and downregulated genes derived upon LPS exposure that highlight the above-mentioned pathways are illustrated in **Table 24**.

COPD-IV LPS vs COPD-IV sham
Top 30 upregulated genes

Gene symbol	*P*-value	BH	FC≥1.3, p<0.05, dabg
LC26A4	0.01628	0.68748	10.56
FCGBP	0.00811	0.68748	7.54
PI3	0.00321	0.67814	7.50
SAA1	0.00022	0.48676	7.36
CCL20	0.00489	0.68748	5.35
SAA2	0.00039	0.54374	5.06
FCGBP	0.01682	0.68748	5.06
CXCL6	0.00272	0.67814	5.03
UBD	0.00019	0.48676	5.00
ALPL	0.00552	0.68748	4.91
CXCL5	0.01710	0.68748	4.00
SERPINA3	0.00529	0.68748	3.89
LTF	0.00261	0.67814	3.89
DEFB4A	0.01470	0.68748	3.74
PDZK1IP1	0.00224	0.67814	3.65
S100A8	0.01655	0.68748	3.47
SOD2	0.00473	0.68748	3.36

COPD-IV LPS vs COPD-IV sham
Top 30 downregulated genes

Gene symbol	*P*-value	BH	FC≥1.3 p<0.05, dabg
KRT7	0.00213	0.67814	-1.56
GPR176	0.01275	0.68748	-1.55
PDGFA	0.04199	0.74422	-1.55
RASSF2	0.00198	0.67814	-1.55
KRT28	0.00359	0.67814	-1.55
hsa_circ_0001338	0.01618	0.68748	-1.54
ANLN.sAug10-u	0.02400	0.69745	-1.54
THOC6	0.00106	0.67442	-1.54
FANCM	0.01355	0.68748	-1.54
LHCGR	0.00198	0.67814	-1.53
CLCN1	0.00324	0.67814	-1.53
HCRTR1	0.00816	0.68748	-1.53
UNC13D	0.00166	0.67814	-1.53
ADARB1	0.01188	0.68748	-1.52
SCARA3	0.00576	0.68748	-1.52
FLYWCH1.o-Aug10	0.01326	0.68748	-1.52
ZNF780A	0.00877	0.68748	-1.52

SPRR2A	0.00378	0.67814	3.32	UNC13C	0.02391	0.69745	-1.52
DEFB4B	0.00376	0.67814	3.32	CILP	0.01166	0.68748	-1.52
MTNR1A	0.00433	0.68748	3.04	SLC2A14	0.00611	0.68748	-1.52
TNFSF15	0.00001	0.31224	2.94	NEMP2	0.01939	0.68748	-1.51
VNN2	0.00280	0.67814	2.89	hsa_circ0001204	0.00768	0.68748	-1.51
CEACAM7	0.02281	0.69745	2.86	OR4F6	0.01960	0.68748	-1.51
TNFAIP2	0.00040	0.54374	2.84	TRO	0.01403	0.68748	-1.51
TNIP3	0.00105	0.67442	2.79	LELP1	0.00341	0.67814	-1.51
SLC5A1	0.02965	0.72027	2.77	RP11-35G9.5	0.01102	0.68748	-1.51
ABCA13	0.01887	0.68748	2.77	PHYHD1	0.00490	0.68748	-1.50
IDO1	0.02387	0.69745	2.72	SULF1	0.00258	0.67814	-1.50
VNN3	0.00369	0.67814	2.60	C1orf100	0.00776	0.68748	-1.50
BIRC3	0.00179	0.67814	2.55	GTSF1L	0.01447	0.68748	-1.50

Table 24: Top 30 upregulated (marked in red) and downregulated (marked in blue) genes derived from bulk transcriptome analysis 24 hours after LPS (1 mg/ml) exposure of COPD-IV cultures. Testing of differential gene expression was done by (paired) Limma T-Test with Benjamini-Hochberg Test (BH Test) for multiple testing correction. Background of the gene datasets (dabg) was detected and reduced using P-values < 5%. Datasets of regulated genes were defined by raw P-values < 5% by using a fold change (FC) gene expression filter $\geq$ 1.3.

The abovementioned pathways and upstream regulators suggest that LPS challenge aggravated inflammatory responses in both non-CLD and COPD-IV cultures. These findings were mirrored in the upregulation of proinflammatory genes (e.g. chemokine family CXCL1/2/3/5/6/8, TNF and VNN3) as well as common protective genes (e.g. SLC26A4, FCGBP, SAA1/2, LTF, PI3SAA1, S100A8) involved in defense mechanisms against LPS-induced acute lung injury (**Figure 22**).
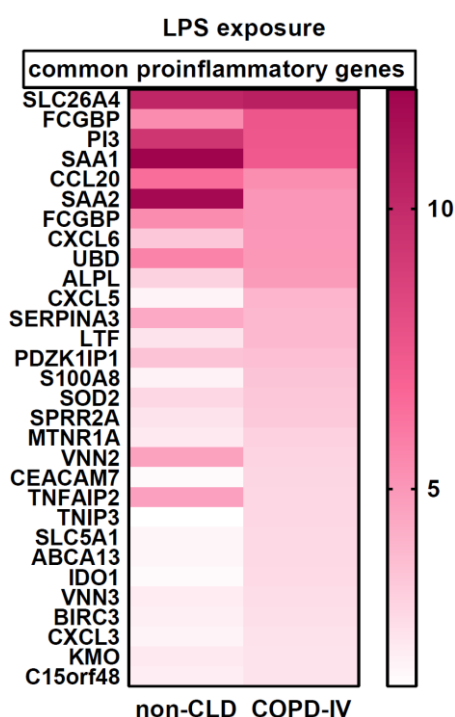
Figure 22: Heatmap illustrating the top 30 fold changes (FC) of the common, significantly upregulated genes derived from bulk transcriptome analysis of non-CLD and COPD-IV cultures 24 hours after LPS (1mg/ml) exposure. Significantly upregulated genes involved in nanoparticle clearance and protection against acute lung injury (FCGBP, SAA1, SAA2, LTF, PI3) are highlighted. Datasets of regulated genes were defined by raw P-values < 5% by using a fold change (FC) gene expression filter $\geq$ 1.3.

Besides the common proinflammatory pathways illustrated above, LPS-exposed COPD-IV cultures were characterized by activation of upstream regulators involved in epithelial apoptosis (GO:1904036, [IL10, IL13, NUPR1]), endothelial apoptosis (GO:0072577, [IL10, HIPK1]), hematopoiesis (GO:0030097, [IL10, CSF1R, CEBPE, HIPK1]) and macrophage proliferation

(GO:0120040, [CSF1R, IL33]). These pathways reflect potentially protective mechanisms of the diseased cultures upon LPS exposure and the interrelation between epithelial cell differentiation and hematopoiesis upon NP challenge (**Figure 23**).
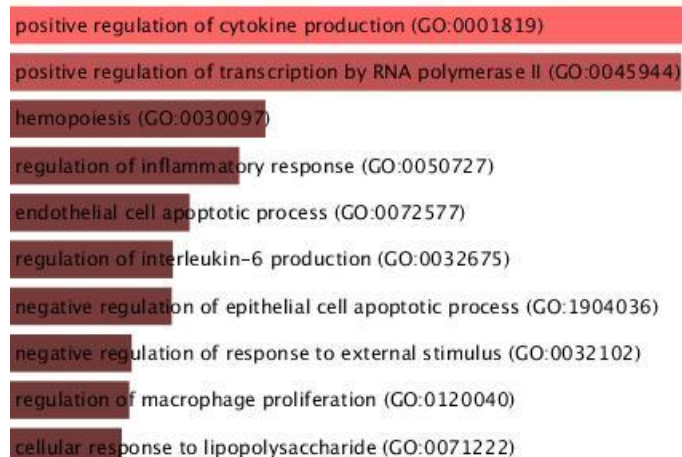
Figure 23: Top 10 significant *P*-values for Gene ontology (GO) terms derived from the upregulated genes (n=435) of the bulk transcriptome 24 hours after LPS (1 mg/ml) exposure in COPD-IV vs non-CLD cultures, reflecting potentially protective mechanisms of the diseased cultures upon LPS exposure. For each pathway the GO term derived from the GO biological Process 2021 specified in the online Enrichr database was attached. GO terms were sorted by *P*-value ranking.

Secretome analysis

Analogously to ZnO, LPS exposed cultures triggered common organelle organization- (GO:0006996), protein localization- (GO:0051641), cellular component organization- (GO:0071840, GO:0016043) as well as mitochondrial translation processes (GO:0032543).

An additional regulation of specific pathways for cilium organization (GO:0044782), assembly (GO:0060271) and movement (GO:0007018, GO:0099111, GO:0035735) was observed in LPS exposed COPD-IV cultures. This aspect reflects an aberrant MCC gene expression in accordance with the transcriptome analysis of ZnO exposed COPD-IV cultures (**Figure 16, 17**).

Thus, the aberrant inflammagenic expression of proteins involved in ciliary processes reflects an altered muco-ciliary machinery in LPS exposed COPD-IV cultures (**Table 25**).

No.	GO term	Secretome pathway enrichment analysis COPD-IV LPS vs COPD-IV sham	*P*-value
0	GO:0006996	organelle organization	2.03E-24
1	GO:0071840	cellular component organization or biogenesis	2.29E-17
2	GO:0016043	cellular component organization	5.23E-16
3	GO:0070925	organelle assembly	3.16E-14
4	**GO:0042073**	**intraciliary transport***	1.54E-13

5	**GO:0007017**	**microtubule-based process***	3.91E-13
6	**GO:0044782**	**cilium organization***	3.98E-13
7	**GO:0060271**	**cilium assembly***	4.19E-13
8	**GO:0007018**	**microtubule-based movement***	4.23E-13
9	**GO:0035735**	**intraciliary transport involved in cilium assembly***	5.14E-13
10	GO:0051641	cellular localization	8.16E-13
11	GO:0046907	intracellular transport	2.00E-12
12	**GO:0099111**	**microtubule-based transport***	2.69E-12
13	GO:0031503	protein-containing complex localization	1.23E-10
14	GO:0051649	establishment of localization in cell	2.67E-10
15	GO:0008104	protein localization	4.02E-10
16	GO:0032543	mitochondrial translation	5.99E-10
17	GO:0033036	macromolecule localization	1.23E-09
18	GO:0120031	plasma membrane bounded cell projection assembly	7.02E-09
19	GO:0044085	cellular component biogenesis	7.16E-09
20	GO:0140053	mitochondrial gene expression	7.48E-09

Table 25: Pathway enrichments analysis derived from secretome data of COPD-IV cultures exposed 24 hours to LPS (1 mg/ml), revealing significantly abundant proteins involved in cilium organization and movement (highlighted in bold). * Pathways observed only in COPD-IV cultures exposed to LPS and not found in the non-CLD exposed cultures. GO terms were sorted by *P*-value ranking. Raw *P*-values < 5% were considered significant.

3.2.2.4 Ciliary beating frequency analysis

While non-CLD and COPD-II cultures present a physiologic CBF distribution with frequencies between 5 and 17 Hz, COPD-IV cultures present a biphasic CBF spectrum based on low-beating and high-beating MCC colonies. This pattern was significantly different in comparison to the physiologic pattern observed in the unexposed non-CLD and COPD-II cultures.

Exposure to LPS provoked an identical CBF spectrum in non-CLD cultures, a slightly increased CBF spectrum in COPD-II and a pathologic biphasic CBF spectrum in COPD-IV cultures dominated by MCC colonies with low CBF.

The changes observed in the exposed COPD-IV cultures were significantly different in comparison to the exposed COPD-II cultures, reflecting an aberrant regulation of mucociliary machinery (e.g. cilium organization and movement, **Figure 24**).
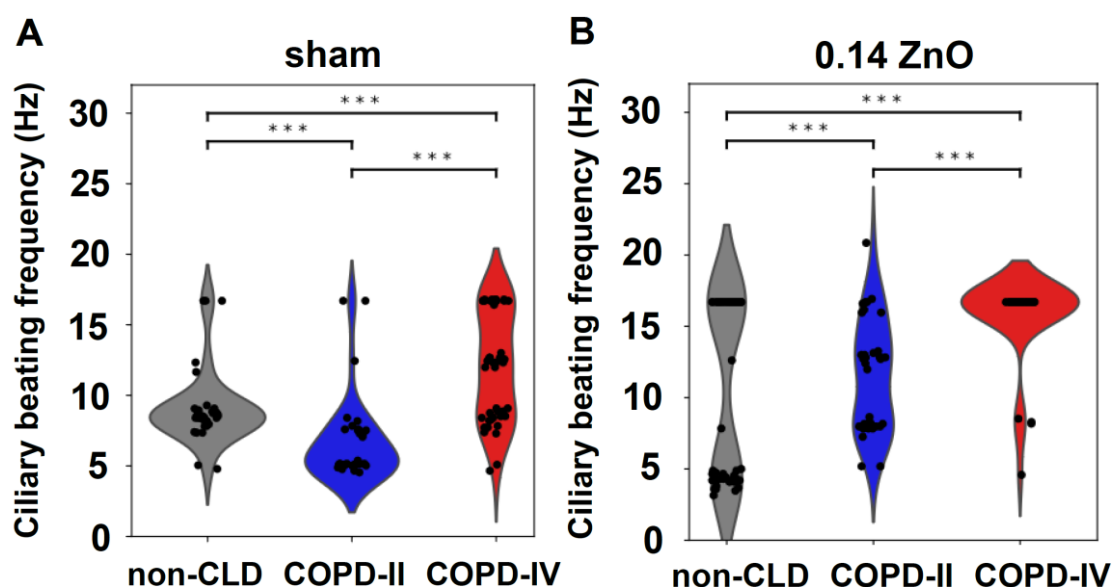
Figure 24: Analysis of distribution of ciliary beating frequencies (CBF, Hz) in non-CLD (n=2), COPD-II (n=2) and COPD-IV (n=2) cultures at baseline level (sham, **A**) and upon LPS (1mg/ml) exposure **(B)**, revealing disease specific changes with a similar (monophasic) CBF spectrum in non-CLD and COPD-II at baseline level and a pathologic biphasic CBF spectrum upon exposure to LPS in COPD-IV cultures. CBF was determined by using a modified ciliaFA protocol[3] upon calculation of average intensity in time and extraction of the highest signal frequencies by using a discrete fourier transform. For each condition, 3 videos (>10 s each) of the top 10 highest CBF were recorded. Comparative analysis of CBF was performed by Kolmogorov–Smirnov Test with *P*-values adjusted by Benjamini–Hochberg multiple testing correction.

3.2.3   pHBECs ALI culture exposure to CNP

3.2.3.1 Cytotoxicity, barrier integrity and viability (LDH release, TEER and WST-1)

Exposure to CNP (10.84 cm^2/cm^2) in healthy cultures, COPD-II und COPD-IV did not affect the LDH release (ΔLDH 1.2 (non-CLD); 2.7 (COPD-II); 0.1 (COPD-IV)), cell membrane integrity (ΔTEER loss 27 (non-CLD); 8.5 (COPD-II); 12.4 (COPD-IV) Ohm x cm^2) or cell viability (ΔWST-1 109 (non-CLD); 97 (COPD-II); 98 (COPD-IV)).

These changes were not significantly different when compared to the ZnO exposure. Taking the outlined findings upon LPS exposure into account, we conclude that the selected inflammagenic pollutans (LPS, CNP) did not affect the barrier function and viability of the exposed cells at selected doses (**Figure 13**).
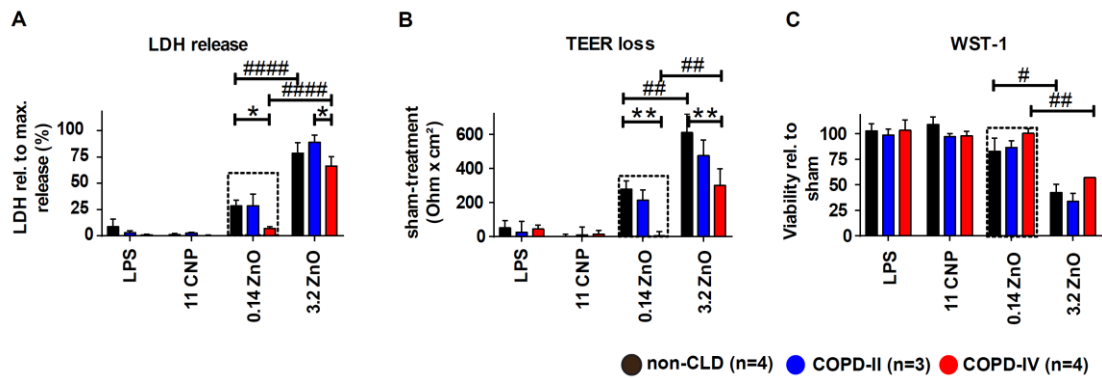
Figure 13: Analysis of membrane integrity **(A)**, barrier integrity loss **(B)** and metabolic cell viability **(C)** of the pHBECs cultures derived from non-CLD, COPD-II and COPD-IV patients 24 hours after NP exposure using lactate dehydrogenase (LDH release) assay, transepithelial electrical resistance (TEER) and tetrazolium salt (WST-1) assay. Results were presented as mean ± SEM with P-values < 5% considered as statistically significant. Specific NPs- and disease-related effects were analyzed via two-way ANOVA with Dunett' post-hoc testing. * Significances within same NP exposure group, # significances within different disease states.

3.2.3.2 Immunoflorescence

3D IF in CNP exposed COPD-II cultures revealed that relative frequency of MCC (Ac.-Tub[+]40.6%) as well as SC (MUC5AC^{+} 6.4%, CC10^{+} 13.1%) was almost similar with those reported in unexposed non-CLD cultures (Ac.-Tub[+] 50.7%, MUC5AC^{+}6.04 %, CC10^{+} 17.1%, **Figure 14**).
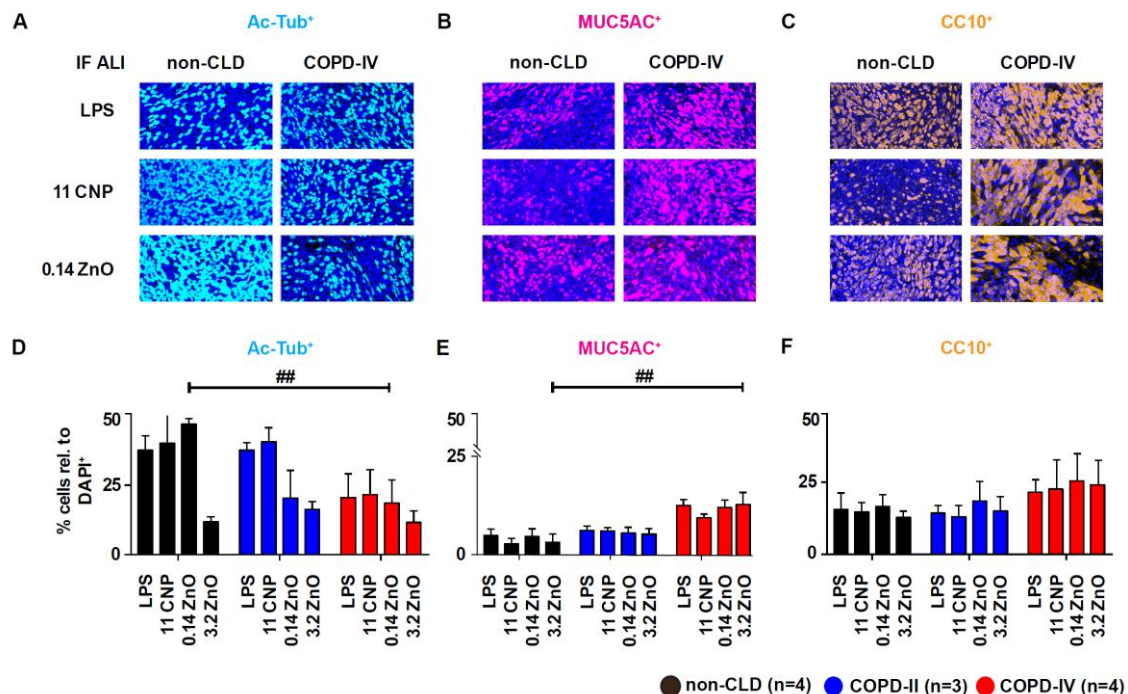
Figure 14: (A-C) Representative 3D IF and **(D-F)** quantification of confocal IF images of the NP exposed ALI cultures, reflecting an increased resilience of COPD-IV pHBECs associated with a hypersecretory oligo-ciliated cell phenotype (increased amount of secretory cells, decreased amount of multi-ciliated cells). Three images were quantified for each culture condition. Results were presented as mean ± SEM with P-values < 5% considered as statistically significant. Specific NPs- and disease-related effects were analyzed via two-way ANOVA with Dunett' post-hoc testing. #Significances within different disease states.

3.2.3.3 Transcriptome and secretome analysis

Transcriptome analysis of CNP exposed non-CLD cultures revealed an upregulated gene cluster involved in cell proliferation and ECM biosynthesis. These mechanisms are negatively regulated by significantly expressed upstream regulators (e.g. AURKB, E2F7, E2F8) that orchestrate cell division and cytokinesis.

In addition, CNP exposed non-CLD cultures were characterized by activation of genes involved in G2/M transition of mitotic cell cycle (GO:0000086, [PLK4, MELK, CENPJ, CDK1, CEP250, NEK2, CCNO, CEP78]), ECM biosynthesis (GO:0015012, [UGDH, XYLT2, HS2ST1]), as well as MCC differentiation (GO:1903251, [PLK4, CCNO]).

These findings suggest that non-CLD cultures are capable of cell proliferation and abnormal cell repair upon CNP exposure.

The top 30 upregulated and downregulated genes in the transcriptome analysis of the CNP exposed non-CLD cultures, involved in the above-mentioned processes are illustrated in **Table 26**.

Non-CLD CNP vs non-CLD sham
Top 30 upregulated genes

Non-CLD CNP vs non-CLD sham
Top 30 downregulated genes

Gene symbol	P-value	adjusted P-value	FC≥1.3 p<0.05 dabg	Gene symbol	P-value	adjusted P-value	FC≥1.3 p<0.05 dabg
ANPEP	0.04827	0.98263	3.38	SERPINB7	0.04686	0.98263	-5.02
CDK1	0.00371	0.98263	2.70	SLC7A5	0.02527	0.98263	-4.47
hsa_circ0001100	0.00178	0.98263	2.66	ASNS	0.02242	0.98263	-4.39
MELK	0.04042	0.98263	2.54	CYP24A1	0.00470	0.98263	-4.09
CPXM2	0.03858	0.98263	2.51	TMPRSS11A	0.04903	0.98263	-3.67
OLFM4	0.03716	0.98263	2.48	S100A7	0.00069	0.98263	-3.19
CDC20B	0.04391	0.98263	2.34	HAS3	0.04751	0.98263	-3.14
TF	0.01735	0.98263	2.32	hsa_circ0000352	0.04645	0.98263	-2.76
VMO1	0.02495	0.98263	2.23	NRP2	0.04277	0.98263	-2.47
CYR61	0.00379	0.98263	2.20	TNFAIP6	0.02256	0.98263	-2.42
SHCBP1	0.00098	0.98263	2.18	SPRR3	0.00322	0.98263	-2.41
ZNF608	0.01870	0.98263	2.17	MMP13	0.00572	0.98263	-2.27
TNS3	0.01784	0.98263	2.16	MFSD2A	0.03099	0.98263	-2.26
TGFBI	0.02117	0.98263	2.16	ARHGAP26	0.00987	0.98263	-2.25
SLC6A8	0.03925	0.98263	2.08	SPRR2D	0.01552	0.98263	-2.17
C4BPA	0.02997	0.98263	2.01	ST5.weAug10-	0.00274	0.98263	-2.08
TYMS	0.04546	0.98263	2.00	DUOX2	0.04523	0.98263	-2.06
TLR6	0.04391	0.98263	2.00	PSAT1	0.02623	0.98263	-2.05
TFCP2L1	0.02963	0.98263	1.99	hsa_circ0076913	0.01099	0.98263	-2.03
VNN2	0.00287	0.98263	1.97	PLK3	0.04150	0.98263	-2.02

CCDC171	0.00392	0.98263	1.96	PSMB10	0.04979	0.98263	-2.01
GPC6.eAug10-u	0.00775	0.98263	1.92	RASGEF1B	0.04048	0.98263	-2.01
TDRKH	0.00459	0.98263	1.91	ABCA12	0.03616	0.98263	-1.99
C14orf28	0.02604	0.98263	1.90	NCCRP1	0.01624	0.98263	-1.99
NEK2	0.00402	0.98263	1.90	DESI1	0.01290	0.98263	-1.99
SGCE	0.01894	0.98263	1.89	IGSF10	0.02356	0.98263	-1.98
PLK4	0.00453	0.98263	1.88	ID2	0.01696	0.98263	-1.96
RGMA	0.02942	0.98263	1.88	PDE4B	0.04953	0.98263	-1.96
CCNO	0.02677	0.98263	1.88	GLYATL2	0.01364	0.98263	-1.93
TMEM63C	0.04678	0.98263	1.88	RORA	0.01286	0.98263	-1.93

Table 26: Top 30 upregulated (marked in red) and downregulated (marked in blue) genes derived from bulk transcriptome analysis 24 hours after CNP (10.8 cm^2/cm^2) exposure of non-CLD cultures. Testing of differential gene expression was done by (paired) Limma T-Test with Benjamini-Hochberg Test (BH Test) for multiple testing correction. Background of the gene datasets (dabg) was detected and reduced using *P*-values < 5%. Datasets of regulated genes were defined by raw *P*-values < 5% by using a fold change (FC) gene expression filter ≥ 1.3.

The main pathways derived from the upregulated genes (n=237) in non-CLD cultures exposed to CNP are illustrated in **Figure 25**.
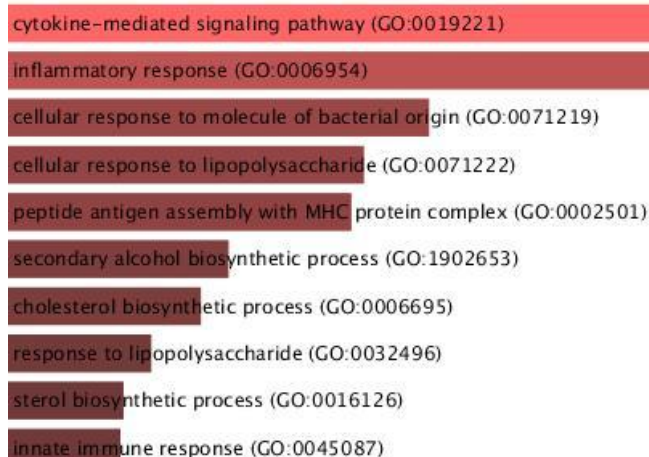

Figure 25: Top 10 significant *P*-values for Gene ontology (GO) terms derived from the upregulated genes (n=237) of the bulk transcriptome 24 hours after CNP (10.8 cm^2/cm^2) exposure in non-CLD cultures, reflecting the activation of cell proliferation and abnormal cell repair mechanisms (e.g. extracellular matrix remodeling) upon CNP exposure. For each pathway the GO term derived from the GO biological Process 2021 specified in the online Enrichr database was attached. GO terms were sorted by *P*-value ranking.

Analogously, CNP exposed COPD-IV cultures determine an aberrant activation of cilium assembly (GO:0060271, [TTC26, CFAP74, RSPH4A, DNAI2, DNAAF1, CCDC113, CCP110, FOXJ1, EHD3, RP1, RSPH1, NPHP1, DZIP1L, CCDC65, B9D2, BBOF1, CNGA4, ZMYND10]), organization (GO:0044782, [TTC26, DNAI2, TSGA10IP, DNAAF1, CCDC113, CCP110, FOXJ1, TTC29, CFAP126, IQCG, EHD3, CATIP, DZIP1L, RTTN, CCDC65, B9D2, CNGA4]) and movement (GO:0003351, [SPAG17, DNAAF1, NEK10, SPA17, CFAP53]).

These mechanisms are positively regulated by significantly expressed upstream regulators ([RFX3, FOXJ1]) that orchestrate the epithelial cell differentiation towards MCC (GO:0030858). The top 30 upregulated and downregulated genes in the transcriptome analysis of the CNP exposed COPD-IV cultures, involved in the above-mentioned processes are illustrated in **Table 27**.

COPD-IV CNP vs COPD-IV sham

Top 30 upregulated genes

Gene symbol	*P*-value	BH	FC≥1.3, p<0.05, dabg
DLGAP5	0.00037	0.79188	2.23
PIFO	0.01422	0.79188	1.95
CCDC65	0.00095	0.79188	1.90
FRMD4A	0.00180	0.79188	1.86
FAM111B	0.00048	0.79188	1.83
AGBL2	0.00177	0.79188	1.83
TMEM232	0.00903	0.79188	1.81
LDLRAD1	0.01245	0.79188	1.78
NUSAP1	0.00278	0.79188	1.76
PUS7	0.00044	0.79188	1.74
C9orf24	0.01357	0.79188	1.72
SERPINB11	0.01290	0.79188	1.72
CFAP99	0.00107	0.79188	1.72
DNAI2	0.00109	0.79188	1.71
HIST1H3G	0.01209	0.79188	1.69
CYP2F1	0.01279	0.79188	1.67
ZMYND12	0.01098	0.79188	1.67
SLC7A2	0.01477	0.79188	1.67
C20orf85	0.00315	0.79188	1.66
VWA3B	0.00162	0.79188	1.63
IQUB	0.00310	0.79188	1.63
RSPH1	0.01085	0.79188	1.63
CAPS	0.01316	0.79188	1.62
CYP2B6	0.00558	0.79188	1.62
ANLN	0.01504	0.79188	1.62
CENPF	0.00054	0.79188	1.61
RSPH4A	0.01394	0.79188	1.60
FOXM1	0.00224	0.79188	1.60
HLA-DQB1	0.00148	0.79188	1.59
IQCG	0.00668	0.79188	1.59

COPD-IV CNP vs COPD-IV sham

Top 30 downregulated genes

Gene symbol	*P*-value	BH	FC≥1.3, p<0.05, dabg
MT1L	0.02602	0.81578	-1.31
CXorf57	0.03745	0.82536	-1.31
AC208162.1	0.02007	0.81578	-1.31
ACBD5	0.02582	0.81578	-1.31
NUDT8	0.02212	0.81578	-1.31
INHA	0.02509	0.81578	-1.31
ZGLP1	0.02694	0.81578	-1.31
GRAMD2	0.01607	0.79713	-1.31
KCNQ5	0.02628	0.81578	-1.31
SAMD13	0.04854	0.83556	-1.31
ZNF197	0.02636	0.81578	-1.31
TBC1D26	0.04610	0.83556	-1.31
hsa_circ_0000454	0.02612	0.81578	-1.31
FGF19	0.03800	0.82536	-1.31
SLC15A3	0.01449	0.79188	-1.31
TMEM27	0.04472	0.83440	-1.31
ALG11	0.01429	0.79188	-1.31
ASB10	0.02231	0.81578	-1.31
SENP5.mAug10-	0.04088	0.82656	-1.31
TMEM9	0.01779	0.80642	-1.31
NDUFA10	0.02144	0.81578	-1.30
PORCN	0.03624	0.82536	-1.30
FSHB	0.04336	0.83235	-1.30
LYZL1	0.01815	0.80642	-1.30
GFOD2	0.03877	0.82536	-1.30
FOXRED1	0.03234	0.82536	-1.30
KRTAP9-9	0.01936	0.80642	-1.30
KCNA5	0.01857	0.80642	-1.30
F2R	0.03911	0.82536	-1.30
KRTAP19-7	0.04979	0.83556	-1.30

Table 27: Top 30 upregulated (marked in red) and downregulated (marked in blue) genes derived from bulk transcriptome analysis 24 hours after CNP (10.8 cm^2/cm^2) exposure of COPD-IV cultures. Testing of differential gene expression was done by (paired) Limma T-Test with Benjamini-Hochberg Test (BH Test) for multiple testing correction. Background of the gene datasets (dabg) was detected and reduced using *P*-values < 5%. Datasets of regulated genes were defined by raw *P*-values < 5% by using a fold change (FC) gene expression filter ≥ 1.3.

The most significantly expressed GO terms derived from the upregulated differentially expressed genes (n=403) in CNP exposed COPD-IV cultures revealed the activation of ciliary biosynthesis and kinetic processes as shown in **Figure 26**.

Figure 26: Top 10 significant *P*-values for Gene ontology (GO) terms derived from the upregulated genes (n=403) of the bulk transcriptome 24 hours after CNP (10.8 cm^2/cm^2) exposure in COPD-IV cultures, reflecting an aberrant activation of ciliary processes upon CNP exposure. For each pathway the GO term derived from the GO biological Process 2021 specified in the online Enrichr database was attached. GO terms were sorted by *P*-value ranking.

Secretome analysis

Exposure of COPD-IV cultures to CNP led to common organelle organization- (GO:0006996), protein localization- (GO:0008104), as well as mitochondrial translation (GO:0032543) processes. These unspecific and ubiquitously present intracellular mechanisms reflect the unchanged viability and barrier integrity of pHBECs in CNP exposed and unexposed COPD-IV cultures (**Table 28**).

No.	GO term	Secretome pathway enrichment analysis COPD-IV CNP vs COPD-IV sham	*P*-value
0	GO:0003723	RNA binding	8.81E-11
1	GO:0006996	organelle organization	1.49E-10
2	GO:0071840	cellular component organization or biogenesis	4.61E-10
3	GO:0051641	cellular localization	7.17E-10
4	GO:0006396	RNA processing	5.11E-09
5	GO:0006397	mRNA processing	8.07E-09
6	GO:0016043	cellular component organization	1.63E-08
7	GO:0033036	macromolecule localization	5.25E-08

8	GO:0008380	RNA splicing	7.43E-08
9	GO:0032543	mitochondrial translation	8.87E-08
10	GO:0016071	mRNA metabolic process	2.25E-07
11	GO:0000377	RNA splicing, via transesterification reactions with bulged adenosine as nucleophile	7.56E-07
12	GO:0000398	mRNA splicing, via spliceosome	7.56E-07
13	GO:0008104	protein localization	7.95E-07
14	GO:0006412	translation	8.02E-07
15	GO:0043604	amide biosynthetic process	9.41E-07
16	GO:0051649	establishment of localization in cell	9.62E-07
17	GO:0000375	RNA splicing, via transesterification reactions	9.84E-07
18	GO:0140053	mitochondrial gene expression	2.04E-06
19	GO:0043043	peptide biosynthetic process	3.97E-06
20	GO:0005515	protein binding	5.56E-06

Table 28: Pathway enrichments analysis derived from secretome data of COPD-IV cultures exposed 24 hours to CNP (10.8 cm^2/cm^2), revealing significantly abundant proteins involved in classical RNA binding and organelle organization mechanisms. GO terms were sorted by *P*-value ranking. Raw *P*-values < 5% were considered significant.

3.2.3.4 Ciliary beating frequency analysis

Reflecting the mechanisms that orchestrate the terminal cell differentiation towards MCC (GO:0030858) and the aberrant regulation of muco-ciliary machinery, a pronounced biphasic spectrum of CBF in COPD-IV cultures was observed (**Figure 27**). The pattern reflected a discoordinated ciliary activity in CNP exposed COPD-IV cultures, indirectly mirrored in the aberrant activation of ciliary processes observed at transcriptome level. These functional changes, however, were only present in end-stage COPD cultures, whereas COPD-II cultures did not suffer significant ciliary changes upon CNP exposure. The almost similar CBF patterns observed in the unexposed and exposed COPD-II cultures were in line with the unchanged cell composition, viability and barrier function upon CNP exposure.
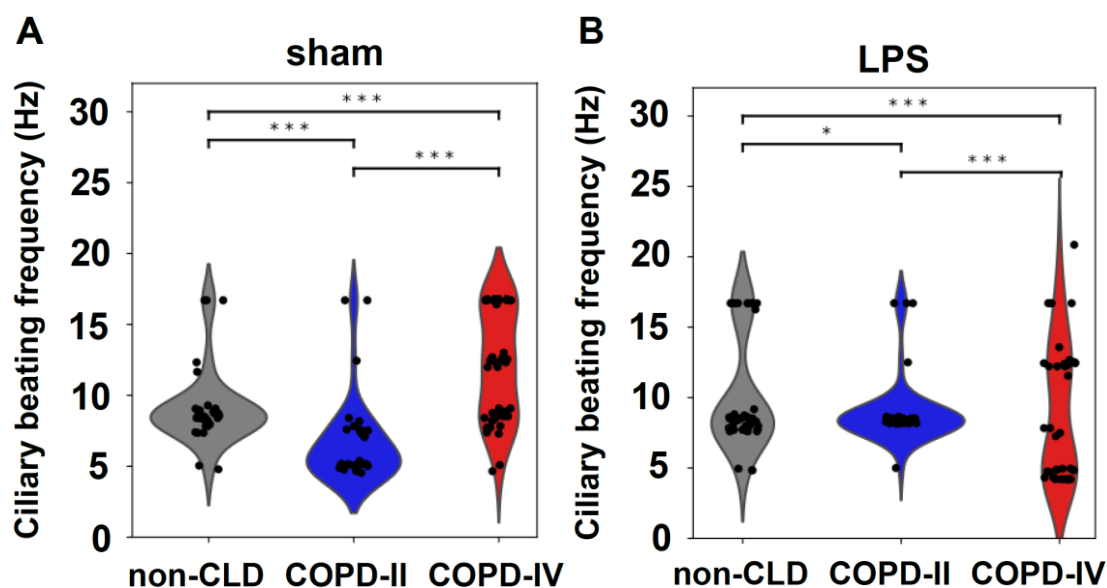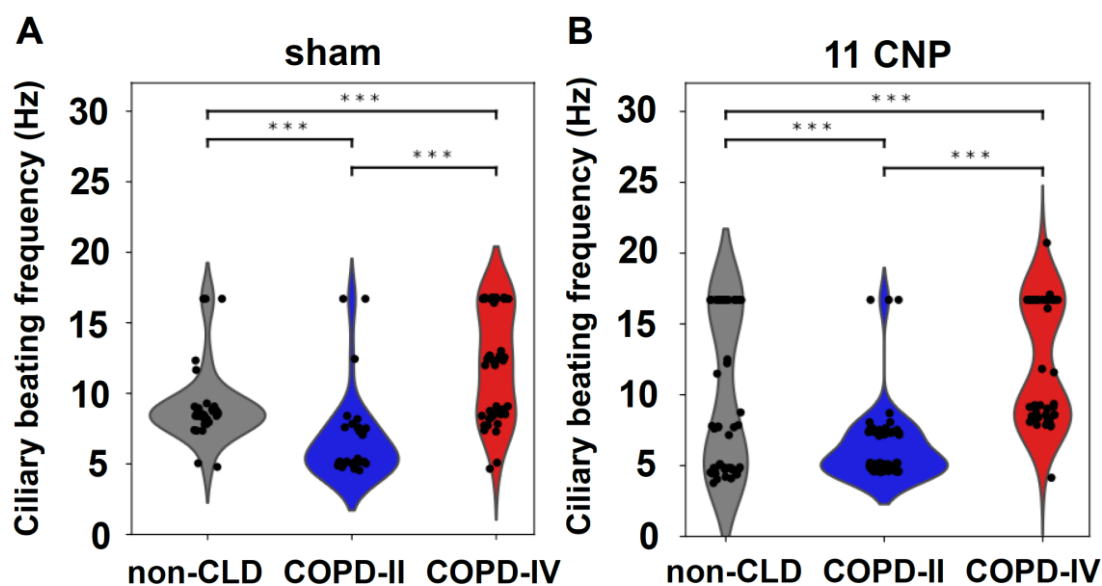
Figure 27: Analysis of distribution of ciliary beating frequencies (CBF, Hz) in non-CLD (n=2), COPD-II (n=2) and COPD-IV (n=2) cultures at baseline level (sham, **A**) and upon CNP ($10.8\ cm^2/cm^2$) exposure **(B)**, revealing disease specific changes with a similar (monophasic) CBF spectrum in non-CLD and COPD-II at baseline level and a pathologic biphasic CBF spectrum upon exposure to CNP in COPD-IV cultures. CBF was determined by using a modified ciliaFA protocol[3] upon calculation of average intensity in time and extraction of the highest signal frequencies by using a discrete fourier transform. For each condition, 3 videos (>10 s each) of the top 10 highest CBF were recorded. Comparative analysis of CBF was performed by Kolmogorov–Smirnov Test with *P*-values adjusted by Benjamini–Hochberg multiple testing correction.

3.2.4 Analysis of pHBECs ALI culture at baseline level

In order to investigate the effects of pollutant exposure on the proximal bronchial epithelium and address the resilience of COPD-IV derived cultures upon NP exposure, cell compositional and functional changes were weekly analyzed (ALId7, ALId14, ALId21, ALId28) via Transepithelial electrical resistance (TEER) and 3D confocal immunofluorescence (IF). The results were comparatively analyzed in non-CLD, COPD-II and COPD-IV cultures.

3.2.4.1 Cytotoxicity, barrier integrity and viability (LDH release, TEER and WST-1)

Non-CLD derived cultures were characterized by a continuously increasing epithelial barrier resistance until ALId28 (ΔTEER increase: 83.8 Ohm x cm^2/ week). On ALId28, non-CLD cultures achieved physiologic TEER values (808±259 Ohm x cm^2; **Figure 28**), in line with previously reported results for human tracheal/ bronchial epithelia (700-1200 Ohm x cm^2) or normal human bronchial epithelial cells (NHBE, 766±154 Ohm x cm^2) [4,124]. On ALId28, pHBECs cultures revealed a disease specific alteration of barrier resistance with slightly reduced TEER values (724±240 Ohm x cm^2) in COPD-II and low TEER values (472±125 Ohm x cm^2) in COPD-IV derived cultures, when compared to the non-CLD derived cultures (**Figure 28**).
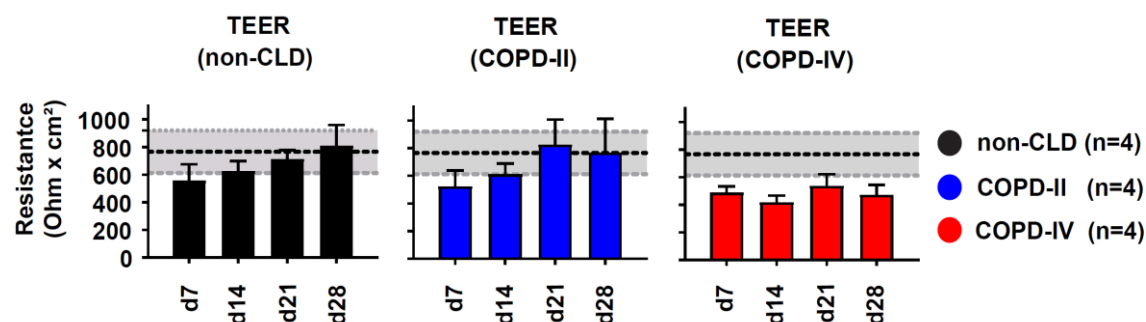
Figure 28: Comparative analysis of barrier integrity in non-CLD, COPD-II and COPD-IV derived cultures at baseline level during the whole timecourse of cell differentiation (ALId7-28) by transepithelial electrical resistance (TEER), reflecting a physiological barrier resistance in non-CLD and COPD-II cultures and a disease specific, decreased barrier integrity in COPD-IV cultures. 766±154 Ohm x cm^2 (marked gray dashed line) were considered physiological values for fully differentiated pHBECs at ALI according to Srinivasan et al.[4].

3.2.4.2 Immunofluorescence

The non-CLD derived pHBECs cultures were dominated by a physiologic number of MCC (Ac.-Tub$^+$: 52.9±1.2%) as well as SC (MUC5AC$^+$: 5.4±1% and CC10$^+$: 15±5.3%) on ALId28 (**Figure 29**). The cellular composition was in line with previously reported results for MCC (Ac.-Tub$^+$: 47-49%) [78,79] and SC (MUC5AC$^+$: 6-21%) [79,125]. During pHBECs differentiation, non-CLD cultures showed a 3-fold increase in total cell counts due to the tripling of MCC (Ac.-Tub$^+$ALId14: 17.89±5.1%, ALId28: 52.9±1.2%, **Figure 29**). MUC5AC$^+$ SC increased 2.5 times (ALId14) and reached maximum counts together with CC10$^+$ cells on ALId14 (MUC5AC$^+$:10.2±0.16%; CC10$^+$:17.3±0.7%), followed by a slight decrease until ALId28 (MUC5AC$^+$: 5.4±0.92%; CC10$^+$: 15.0±5.3%).
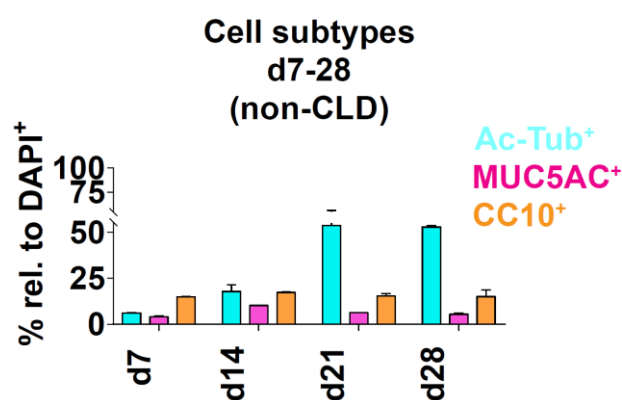
Figure 29: Quantification of confocal immunofluorescence images of the unexposed ALI cultures derived from one non-CLD patient during the whole timecourse of cell differentiation (ALId7-28), revealing a gradual, weekly increase in the number of multi-ciliated cells (Ac.-Tub$^+$) until ALId28 and a stable amount of secretory cells (MUC5AC$^+$ and CC10$^+$) between ALId14 and ALId28. Three images were quantified for each timepoint. Results were presented as mean ± SEM with P-values $< 5\%$ considered as statistically significant.

To mimic compositional similarities between pHBECs ALI cultures and human bronchial mucosa, a novel *ex vivo* ALI culture model based on native bronchial wall samples (Bronchial punches/ BP) was developed in our laboratory (**Figure 30**). BP present the native 3D tissue architecture of the proximal bronchi with all resident cell populations. BP can be cultured up to 4 days at ALI.
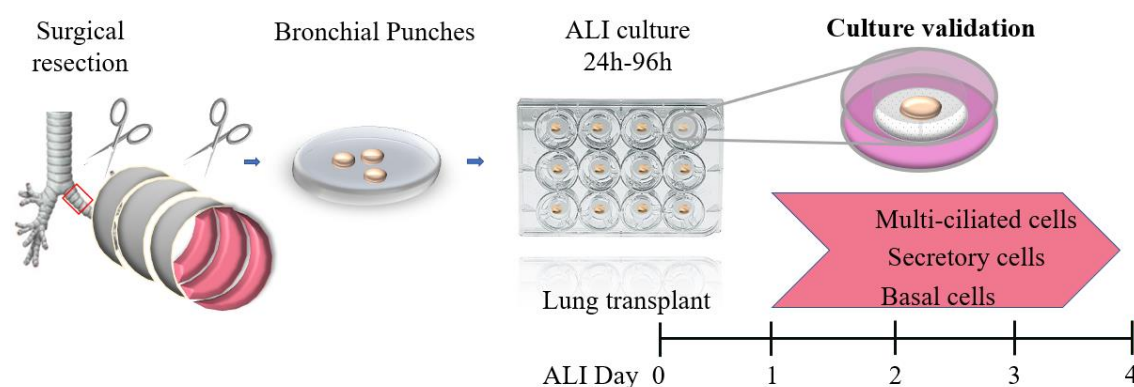
Figure 30: Schematic representation of the air liquid interface (ALI) *ex vivo* culture model based on native human bronchial punches (BPs). Upon lung transplantation, immediate dissection of bronchial wall pieces is followed by section of 4 mm BPs. Direct ALI culture on special filter membranes allows the contact of the cartilaginous part of BPs with the basal media and of the mucosa with the air. The ALI culture is maintained up to 4 days and used for the validation of terminal pHBECs differentiation *in vitro*.

Of note, end-differentiated non-CLD pHBECs ALI cultures presented striking similarities with the *ex vivo* cultured BPs characterized by multiple mucosa folds covered by homogenously distributed MCC and mucus producing SC (**Figure 31**).
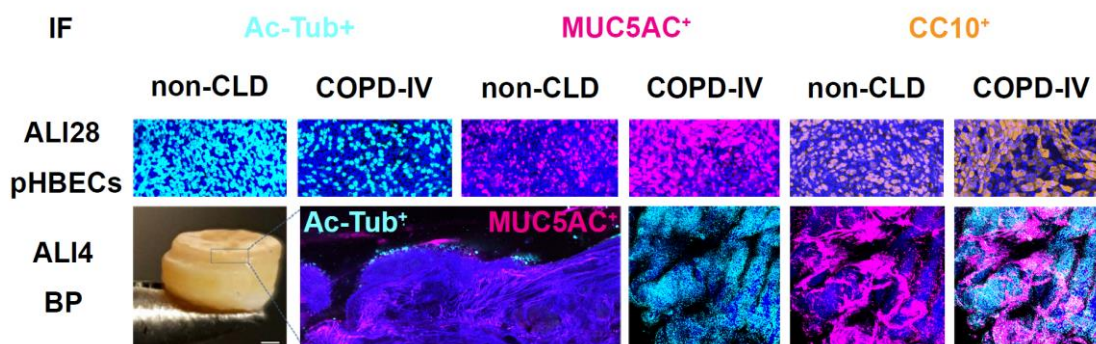
Figure 31: Comparative analysis of 3D confocal microscopy images of *in vitro* pHBECs cultures on ALId28 (upper 6 panels) and *ex vivo* cultured native bronchial wall tissue punches (BPs) on ALId4 after lung transplantation (lower 5 panels). Representative image of a 4 mm bronchial punch (left lower panel) derived from a non-CLD patient illustrating a bronchial pseudostratified epithelium with apical acetylated tubulin expression in multi-ciliated cells (Ac-Tub$^+$) and a thin mucus film (MUC5AC$^+$) on the top of the multi-ciliated cells. Submucosal autofluorescent elastin fibers in the lamina propria as well as mucous glands and DAPI$^+$ nuclei are stained in blue.

Cell composition of COPD-IV cultures revealed a 3-fold reduced amount of MCC (Ac.-Tub$^+$: 17.2±9.1%), as well as an increased amount of SC (MUC5AC$^+$: 14.5±5.1% and CC10$^+$: 26.9±10%), when compared to non-CLD cultures on ALId28 (**Figure 32**). In contrast to non-CLD cultures on ALId28, COPD-II cultures were characterized by a 1.2-fold decrease in MCC (Ac.-Tub$^+$: 42.7±3.4%) and an increase in SC (MUC5AC$^+$: 7.3±0.2% and CC10$^+$: 18.23±3.22%, **Figure 32**).
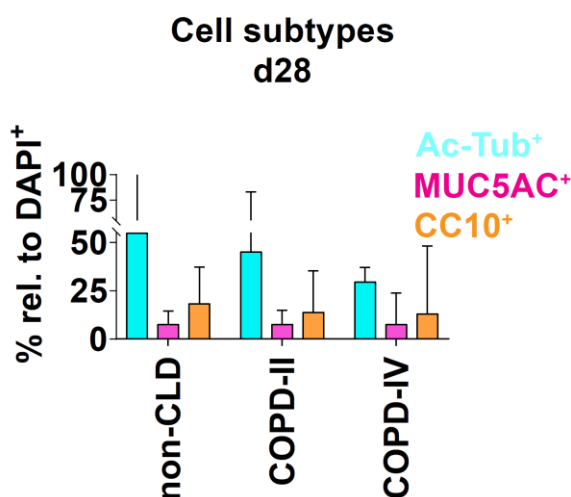
Figure 32: Quantification of confocal immunofluorescence (IF) images of the unexposed end-differentiated non-CLD (n=4), COPD-II (n=3) and COPD-IV cultures (n=4) on ALId28, revealing a 3-fold reduced amount of multi-ciliated cells (Ac.-Tub$^+$) and an increased amount of secretory (MUC5AC$^+$ and CC10$^+$ cells) in COPD-IV when compared to non-CLD cultures. Three images were quantified for each timepoint. Results were presented as mean ± SEM with *P*-values $< 5\%$ considered as statistically significant.

COPD-IV pHBECs cultures were characterized by an oligo-ciliated and hypersecretory phenotype that was validated by IF of native proximal human bronchus sections. This culture showed abundant colonies of enlarged SC (MUC5AC$^+$, CC10$^+$) producing a thick mucus film and low-numbered, misaligned MCC (**Figure 33**). Native human bronchus sections presented a significant increase in MUC5AC$^+$ cells in COPD-IV samples (average intensity related to DAPI$^+$ 50% (COPD-IV), 20% (non-CLD)) and an unchanged amount of CC10$^+$ SC (average intensity related to DAPI$^+$ 50% (COPD-IV), 47% (non-CLD)).

The amount of MCC was not significantly different in both cultures (average intensity related to DAPI$^+$ 10% (COPD-IV), 6% (non-CLD), **Figure 33**).
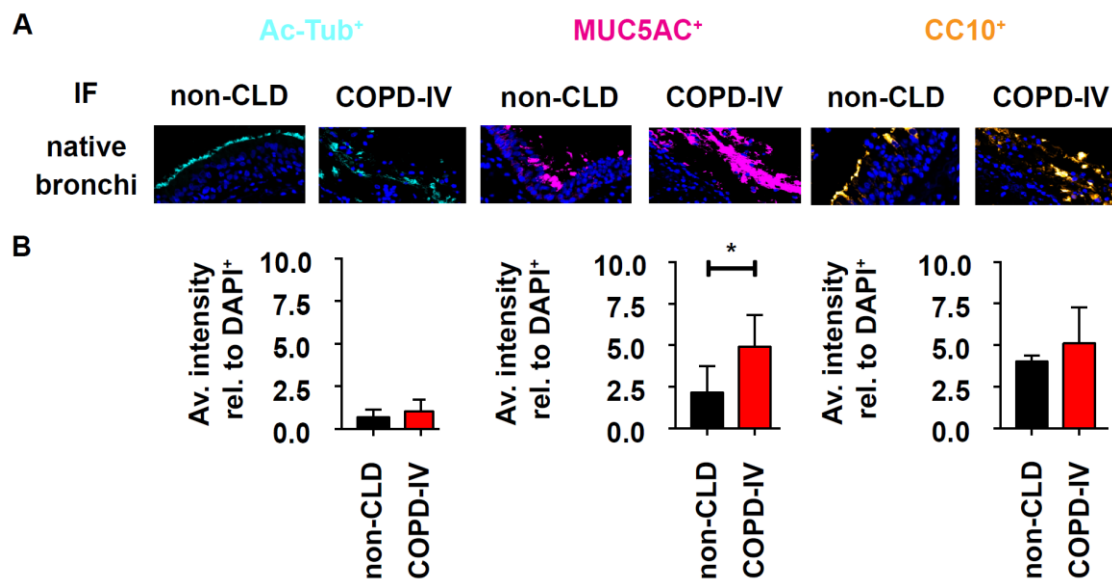
Figure 33: Comparative immunofluorescence stainings **(A)** and quantification **(B)** of non-CLD and COPD-IV native bronchi, revealing a misaligned bronchial epithelium with disorganized distribution of basal, secretory and multi-ciliated cells in COPD-IV when compared to non-CLD cultures **(A)**. A significantly increased amount of secretory (MUC5AC$^+$) cells in COPD-IV cultures and an almost unchanged amount of multi-ciliated (Ac-Tub$^+$) cells in both non-CLD and COPD-IV cultures defined the hypersecretory phenotype of COPD-IV cultures **(B)**.

COPD disease progression could be simulated upon chronic exposure of COPD-II cultures to cigarette smoke extract (CSE) at ALI. Accordingly, the amount of MCC decreased 1.4 and 1.6-fold upon CSE exposure, in comparison to the unexposed COPD-II and non-CLD derived cultures on ALId28 (Ac.-Tub$^+$: 50.7±3.0% (non-CLD), 42.7±3.4% (COPD-II unexposed), 31.5±1.5% (COPD-II CSE)). The amount of SC was not significantly affected upon CSE exposure (MUC5AC$^+$: 7.3±0.2% (COPD-II unexposed), 6.5±0.4% (COPD-II CSE), 14.5±5.1% (COPD-IV) and CC10$^+$: 18.2±3.2% (COPD-II unexposed), 11.6±1.7% (COPD-II CSE), 26.9±9.9% (COPD-IV), **Figure 34**).
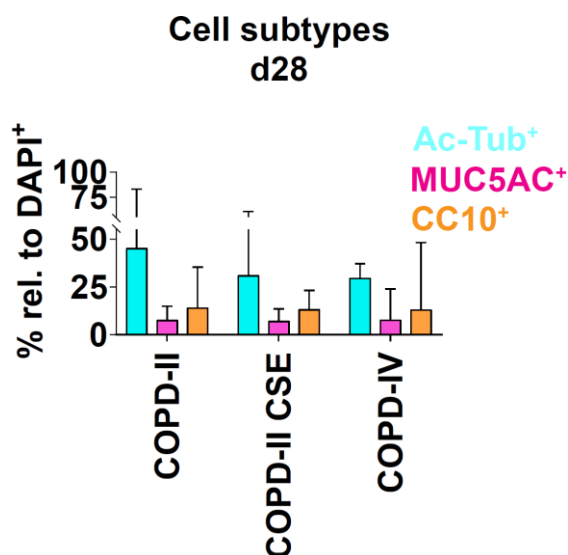
Figure 34: Quantification of confocal immunofluorescence (IF) images of the unexposed end-differentiated COPD-II (n=3) and COPD-IV cultures (n=4) in comparison to cigarette smoke exposed COPD-II cultures (COPD-II CSE, n=3) on ALId28. IF quantification reflects the hypersecretory and oligo-ciliated phenotype of COPD-IV cultures, as well as the CSE-induced disease progression from COPD-II to COPD-IV. Three images were quantified for each timepoint. Results were presented as mean ± SEM with *P*-values < 5% considered as statistically significant.

These compositional changes were mirrored in a reduced barrier integrity in COPD-II CSE cultures (457 ± 4 Ohm x cm^2) when compared to unexposed COPD-II cultures (724 ± 240 Ohm x cm^2).

In addition, COPD-II CSE cultures showed almost similar TEER values with COPD-IV cultures (458 ± 132 Ohm x cm^2, **Figure 35**) on ALId28, thus mimicking phenotype progression from COPD-II to COPD-IV.
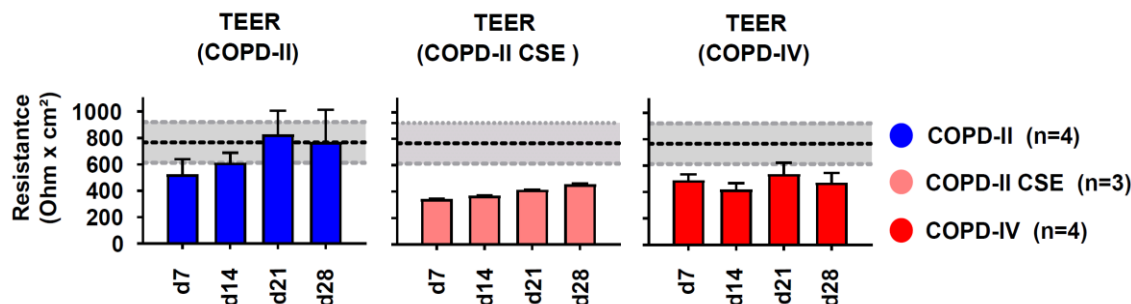
Figure 35: Analysis of barrier integrity in unexposed COPD-II and COPD-IV derived cultures in comparison to cigarette smoke exposed COPD-II cultures (COPD-II CSE) during the whole timecourse of cell differentiation (ALId7-28) by transepithelial electrical resistance (TEER), reflecting the CSE-induced phenotype progression from COPD-II to COPD-IV. 766 ± 154 Ohm x cm^2 (marked gray dashed line) were considered physiological values for fully differentiated pHBECs at ALI according to Srinivasan et al.[4].

3.2.4.3 Transcriptome and secretome analysis

Transcriptome analysis revealed a characteristic pattern underlying the observed cellular differentiation: at baseline level, COPD-IV cultures were characterized by overrepresentation of pathways that indicate the hypersecretory oligo-ciliated phenotype.

Accordingly, carbohydrate/ glycosaminoglycan metabolism (hsa-1630316, hsa-71387) and cellular secretion processes (GO:1901505, GO:0019200, GO:0030246; GO:1901135, GO:0032940, hsa00534, hsa1430728) were overrepresented in COPD-IV derived cultures. Moreover, genes involved in primary ciliogenesis and centrosome duplication (CNTROB, C1orf158, TUBE1, CCP110) were significantly down-regulated, reflecting the prosecretory cell fate and the impaired terminal differentiation into MCC. The aberrant SC-MCC axis differentiation is further explained by the down-regulation of PTEN signaling.

In addition, an overrepresentation of transmembrane carbohydrate (GO: 0045913, GO: 0010676, GO: 0043255) and lipid metabolic processes (GO: 0072367, GO: 0050995, GO: 0010888) at transcriptome level could explain the decreased membrane integrity observed in COPD-IV derived cultures.

Due to continuous environmental pollutants exposure, COPD-IV cultures are characterized by an increased pro-inflammatory pattern at baseline level, indicated by the activation of IL-17C, IL-1β, IFN-γ, IRF3, IL-1RN, NRF1 and TGF-β3.

These findings were in line with overrepresented innate immunity (GO:0045055, GO:0043312, GO:0002283), cell migration (GO:0030334, GO:0030335), as well as cell differentiation and remodeling processes.

.

The top 10 significant GO biological processes derived from the differentially upregulated genes in unexposed COPD-IV cultures are summarized in **Figure 36**.
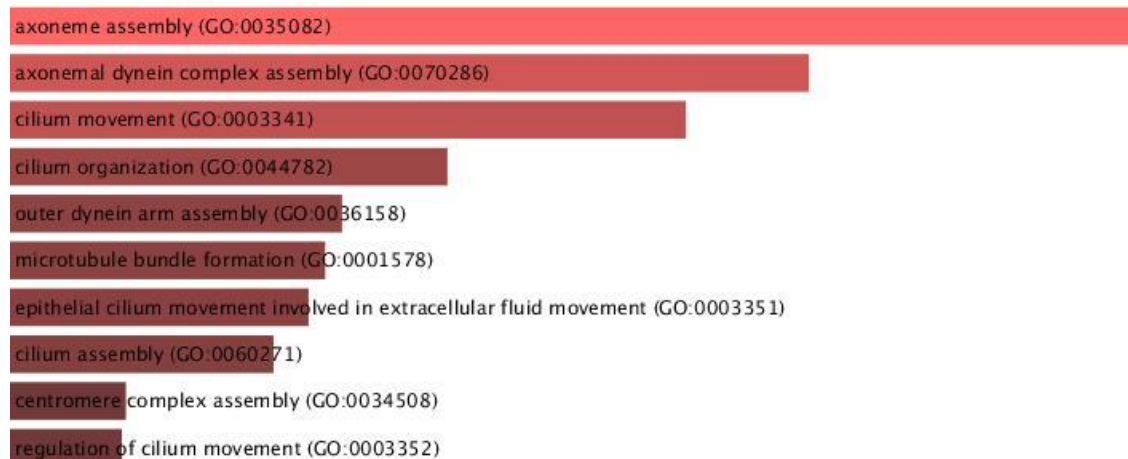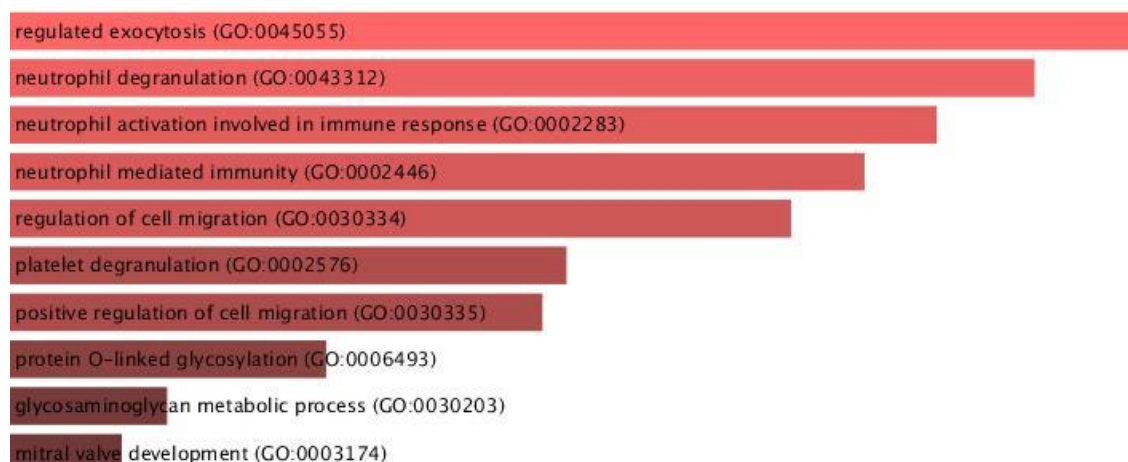

Figure 36: Top 10 significant *P*-values for Gene ontology (GO) terms derived from the upregulated genes (n=1201) of the bulk transcriptome in unexposed COPD-IV cultures when compared to the unexposed non-CLD cultures on ALId28, indicating the involvement of COPD–IV cultures in innate immunity, cell migration and ECM remodeling processes. For each pathway the GO term derived from the GO biological Process 2021 specified in the online Enrichr database was attached. GO terms were sorted by *P*-value ranking.

The top 30 differentially upregulated genes involved in the outlined pathways are summarized in **Table 29**.

COPD-IV sham vs non-CLD sham				COPD-IV sham vs non-CLD sham			
Top 30 upregulated genes				**Top 30 downregulated genes**			
Gene symbol	*P*-value	adjusted *P*-value	FC≥1.3 p<0.05 dabg	Gene symbol	*P*-value	adjusted *P*-value	FC≥1.3 p<0.05 dabg
MMP10	0.001246	0.249730	17.70	TMPRSS11A	0.000960	0.232902	-10.18
GPNMB	0.010931	0.349183	14.84	FAM111B	0.047117	0.511162	-6.16
MMP2	0.005735	0.308557	11.62	ABHD12B	0.000490	0.218723	-5.12
TAGLN	0.036665	0.484525	11.20	SERPINB10	0.006881	0.316721	-4.87
MSMB	0.046829	0.510031	10.80	C1orf194	0.022018	0.420149	-4.29
THBS1	0.015690	0.375572	10.53	TMPRSS11D	0.004583	0.305937	-3.97
GLIPR1	0.000728	0.228289	9.31	SPRR3	0.044273	0.503825	-3.90
MYL9	0.009484	0.338240	9.20	DNAJB13	0.015973	0.375572	-3.85
CAPN13	0.003081	0.286985	8.88	ANKK1	0.015115	0.371346	-3.85
COMP	0.028532	0.450889	7.99	C2orf40	0.020555	0.408978	-3.42
SERPINE1	0.003678	0.299613	7.88	OMG	0.038286	0.490823	-3.24
NID1	0.015885	0.375572	7.80	PCDH19	0.046543	0.508398	-3.09
CAMK2N	0.002266	0.278380	7.56	SERPINB1	0.001786	0.273109	-3.07
ITGB3	0.027316	0.445713	7.24	CWH43	0.048409	0.513418	-2.95
PMEPA1	0.031718	0.464349	6.79	GPD2	0.049690	0.516352	-2.90
SPARC	0.048559	0.513418	6.65	hsa_circ0003009	0.008816	0.338240	-2.88

PTHLH	0.048190	0.513363	6.02	NDUFA12	0.002981	0.286985	-2.87
SLC38A5	0.026014	0.439682	5.70	SLC13A2	0.000981	0.233902	-2.80
LIPG	0.045849	0.506896	5.67	COX7B	0.001497	0.265267	-2.78
KCNJ15	0.005557	0.308557	5.61	SPRR1A	0.004304	0.302050	-2.77
SUSD2	0.031369	0.461141	5.48	hsa_circ0000321	0.034458	0.475239	-2.67
PNLIPRP3	0.018917	0.396216	5.17	SPRR1B	0.024587	0.434374	-2.66
TGM2	0.004479	0.305937	5.05	DAPL1	0.026008	0.439682	-2.64
AKAP12	0.009903	0.340955	5.01	ECT2L	0.041034	0.496109	-2.63
GALNT14	0.038334	0.490852	4.88	CSTA	0.015189	0.371455	-2.48
CCNJL	0.006028	0.308557	4.88	PSMB10	0.002889	0.286985	-2.46
ALDH1A3	0.002550	0.278669	4.56	LSM8	0.026518	0.443305	-2.38
FYB	0.042711	0.499283	4.56	hsa_circ0000797	0.029007	0.451154	-2.28
ENC1	0.001169	0.241732	4.52	NOP16	0.024776	0.434529	-2.27

Table 29: Top 30 upregulated (marked in red) and downregulated (marked in blue) genes derived from bulk transcriptome analysis of unexposed COPD-IV cultures in comparison to the unexposed non-CLD cultures on ALId28. Testing of differential gene expression was done by (paired) Limma T-Test with Benjamini-Hochberg Test (BH Test) for multiple testing correction. Background of the gene datasets (dabg) was detected and reduced using P-values < 5%. Datasets of regulated genes were defined by raw P-values < 5% by using a fold change (FC) gene expression filter ≥ 1.3.

COPD-IV disease specific remodeling upon chronic pollutant exposure is reflected in the significant activation of profibrotic upstream regulators (e.g. FN1, TGFB1/2/3, ITGB6, HIF1, SMAD, EFN4, PTEN, XBP1 and FOXC1) known to drive extracellular matrix (ECM) production and EMT. The main upstream regulators responsible for these processes are summarized in **Table 30**.

Upstream Regulator	FC	z-score transformation	P-value
FN1	73.26	2.07	2.74E-03
EDN1	7.86	3.56	2.99E-02
TGFB2	4.34	2.23	1.29E-02
ITGB6	2.8	1.95	8.91E-03
TGFB3	2.26	3.34	9.64E-06
TIMP3	2.23	-2.12	4.82E-02
APOE	2.07	-3.03	1.42E-02
GLIS2	1.7	-2.22	1.15E-02
TEAD2	1.68	3	4.79E-03
PIK3R1	1.68	1.94	1.18E-03

NEDD9	1.64	1.89	3.31E-02
HIF1A	1.59	3.82	2.50E-03
SYVN1	1.58	4.24	4.79E-04
SP1	1.56	4.24	4.60E-02
HTT	1.56	3.49	5.42E-04
CAB39L	1.55	-3.74	6.42E-07
AGT	1.52	3.64	1.99E-02
PTPN3	1.52	2.2	2.72E-02
SMAD7	1.51	-3.27	2.06E-03
FOXC1	1.49	2.37	9.95E-03
PTEN	1.48	1.88	3.79E-03
EFNA4	1.46	-2.65	4.72E-02
TGFB1	1.45	5.88	1.04E-07
XBP1	1.44	4.59	1.72E-04
CLDN7	1.41	-1.92	9.01E-03

Table 30: Bulk transcriptome analysis in unexposed COPD-IV vs non-CLD cultures on ALId28 with focus on significantly expressed upstream regulators derived from Ingenuity Pathway Analysis®, revealing a significant activation of extracellular matrix remodeling (ECM) and epithelial-to-mesenchymal transition (EMT) processes in COPD-IV cultures. Datasets of regulated genes were defined by raw P-values < 5% by using a fold change (FC) gene expression filter ≥ 1.3 and a z-score transformation > 2 or < -2 (z-score > 2 = activation; z-score < -2 = inactivation).

ECM remodeling implies an early and late biosynthesis of ECM components (e.g. chondroitin-, dermatan- or heparan sulfate). A summary of the ECM processes depicted by Ingenuity Pathway Analysis® is summarized in **Table 31**.

Ingenuity Pathway Analysis® (baseline COPD-IV vs non-CLD)	-log (*P*-value)	z-score transformation
EIF2 Signaling*,#	12.3	-4.12
Oxidative Phosphorylation	6.14	-5.00
Chondroitin Sulfate Biosynthesis*,#	2.98	3.46

Dermatan Sulfate Biosynthesis*,#	2.77	3.46
Chondroitin Sulfate Biosynthesis (Late Stages) *,#	2.48	3.16
Triacylglycerol Biosynthesis	2.44	2.33
Dermatan Sulfate Biosynthesis (Late Stages) *,#	2.09	3.00
Heparan Sulfate Biosynthesis*,#	1.94	3.05
Regulation of Actin-based Motility by Rho	1.87	2.89
Sirtuin Signaling Pathway	1.71	2.89
Superpathway of Inositol Phosphate	1.70	2.04
Actin Cytoskeleton Signaling*,#	1.69	2.99
Choline Biosynthesis III	1.61	2.00
Heparan Sulfate Biosynthesis (Late Stages) *,#	1.49	2.71
Leukocyte Extravasation Signaling	1.46	2.18
PTEN Signaling*,#	1.46	-2.00

Table 31: Ingenuity Pathway Analysis® of bulk transcriptome in unexposed COPD-IV vs non-CLD cultures showing an overactivation of ECM and EMT processes in COPD-IV cultures. * Extracellular matrix remodeling (ECM), # Epithelial-to-mesenchymal transition (EMT). Datasets of regulated genes were defined by raw *P*-values < 5% and -log(*P*-value) > 1.3 by using a fold change (FC) gene expression filter ≥ 1.3 and a z-score transformation > 2 or < -2 (z-score > 2 = activation; z-score < -2 = inactivation).

Secretome analysis

The activation of ECM processes at transcriptome level in unexposed COPD-IV cultures was also reported at secretome level (GO:0030198, GO:0043062). In addition, unspecific intracellular processes in COPD-IV cultures included ubiquitous organelle organization (GO: 0006996), protein synthesis (GO:0043043), as well as transport (GO:0006810, GO: 0015031), targeting (GO:0006605), binding (GO:0006807) and proteolysis processes (GO: 0006508). The binding processes involved different components of cell membrane: proteins (GO:0005515), enzymes (GO:0019899) and integrins (GO:0005178).

The top 20 GO terms that define the unexposed COPD-IV culture at secretome level are summarized in **Table 32**.

No.	GO term	Secretome pathway enrichment analysis Baseline COPD-IV vs non-CLD	*P*-value
0	GO:0071840	cellular component organization or biogenesis	6,06E+07
1	GO:0006996	organelle organization	2,60E+08
2	GO:0051641	cellular localization	3,43E+08
3	GO:0032543	mitochondrial translation	7,90E+08
4	GO:0016043	cellular component organization	8,69E+08
5	GO:0033036	macromolecule localization	1,75E+09
6	GO:0006396	RNA processing	2,54E+10
7	GO:0140053	mitochondrial gene expression	3,21E+09
8	GO:1901566	organonitrogen compound biosynthetic process	3,71E+10
9	GO:0043604	amide biosynthetic process	1,22E+11
10	GO:0006414	translational elongation	1,40E+11
11	GO:0006397	mRNA processing	7,40E+09
12	GO:0008380	RNA splicing	9,55E+10
13	GO:0008104	protein localization	0.0001
14	GO:0070125	mitochondrial translational elongation	0.0002
15	GO:0070126	mitochondrial translational termination	0.0002
16	GO:0044267	cellular protein metabolic process	0.0004
17	GO:1901564	organonitrogen compound metabolic process	0.0004
18	GO:0043603	cellular amide metabolic process	0.0005
19	GO:0019538	protein metabolic process	0.0006
20	GO:0003723	RNA binding	0.0008

Table 32: Pathway enrichments analysis derived from secretome data of unexposed COPD-IV vs non-CLD cultures at baseline level, revealing significantly abundant proteins involved in classical RNA binding and organelle organization processes. GO terms were sorted by *P*-value ranking. Raw *P*-values < 5% were considered significant.

3.2.4.4 Ciliary beating frequency analysis

The unexposed non-CLD cultures present a physiologic CBF distribution between 5 and 17 Hz, in accordance with previous studies (CBF 7-16 Hz) [81]. Unexposed COPD-II cultures presented a similar CBF distribution as non-CLD cultures, with a significantly lower CBF spectrum. In contrast, unexposed COPD-IV cultures were characterized by a pathologic biphasic CBF spectrum due to the presence of discoordinated low beating and high beating MCC colonies.

The CBF distribution in unexposed COPD-IV cultures was significantly different in comparison to the physiologic pattern observed in unexposed non-CLD and COPD-II cultures (**Figure 37**).
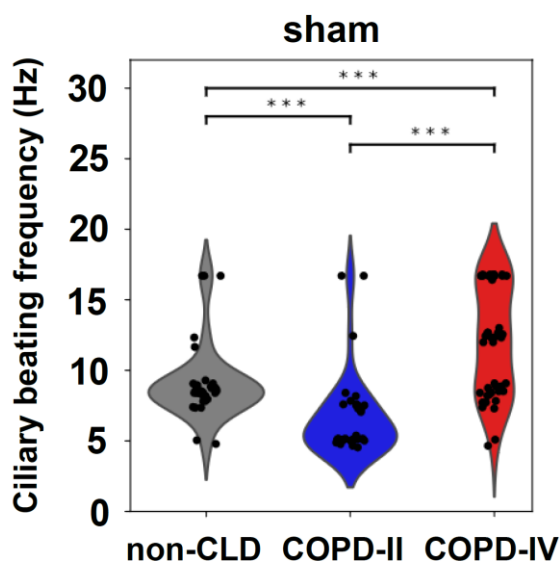
Figure 37: Analysis of distribution of ciliary beating frequencies (CBF, Hz) in non-CLD (n=2), COPD-II (n=2) and COPD-IV (n=2) cultures at baseline level (sham) on ALId28, revealing significantly different disease specific changes with a similar (monophasic) CBF spectrum in non-CLD and COPD-II cultures and a pathologic biphasic CBF spectrum in COPD-IV cultures. CBF spectrum of COPD-II cultures is significantly lower in comparison to the non-CLD CBF. The biphasic CBF spectrum of COPD-IV cultures reveals the presence of discoordinated low beating and high beating multiciliated cells colonies. CBF was determined by using a modified ciliaFA protocol[3] upon calculation of average intensity in time and extraction of the highest signal frequencies by using a discrete fourier transform. For each condition, 3 videos (>10 s each) of the top 10 highest CBF were recorded. Comparative analysis of CBF was performed by Kolmogorov–Smirnov Test with *P*-values adjusted by Benjamini–Hochberg multiple testing correction.

3.2.4.5 Single cell RNA-seq drop-seq analysis

To comprehensively analyze the dynamics of the pHBECs differentiation, longitudinal single cell RNA-seq analysis was performed during the whole timecourse of pHBECs differentiation. Briefly, pHBECs cell suspensions from 7 different timepoints (ALId0, 3, 5, 7, 14, 21 and 28) from n=2 non-CLD and n=2 COPD-IV patients were collected (**Figure 38**).
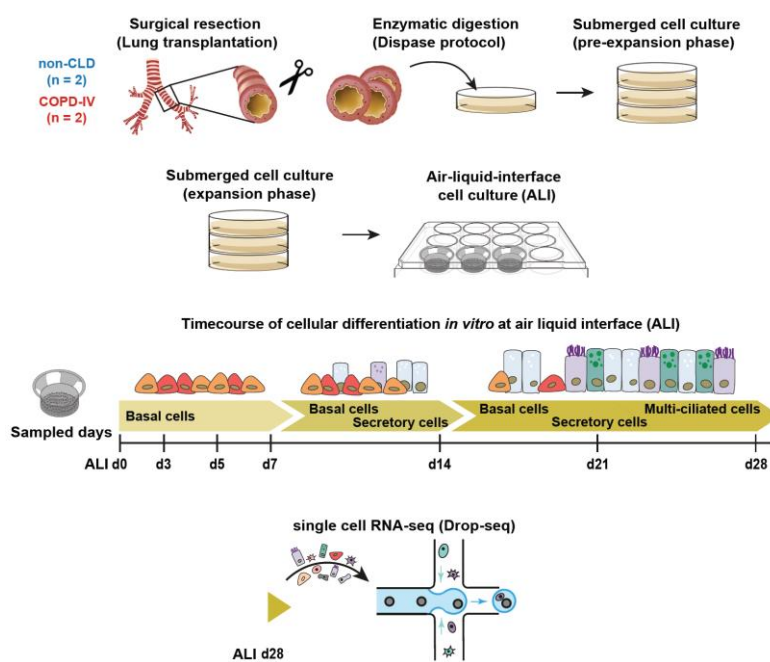
Figure 38: Experimental approach and timecourse of longitudinal single cell RNA-seq drop-seq analysis: native bronchial tissue samples derived from n=2 non-CLD and n=2 COPD-IV patients were immediately processed upon lung transplantation. Primary human bronchial epithelial cells (pHBECs) isolated upon enzymatic digestion are cultured under submerged conditions and seeded on transwell inserts in order to establish the ALI culture. Upon airlift, pHBECs cell suspensions are sampled on 7 different timepoints at ALI (d0, 3, 5, 7, 14, 21 and 28) and prepared for single cell RNA-seq drop-seq analysis according to a modified protocol by Angelidis et al. [5].

Two-dimensional representation of the single cell transcriptional clusters was designed by using the Uniform Manifold Approximation and Projection (UMAP) method in order to provide data related to cell subtypes and disease state (**Figure 39**). Based on previously published specific cell canonical markers, particular clusters for BC (KRT5$^+$/ TRP63$^+$), sBC (SERPINB4$^+$), secretory GC (SCGB3A1$^+$) and MCC (FOXJ1$^+$) on airlift day (ALId0) have been identified.
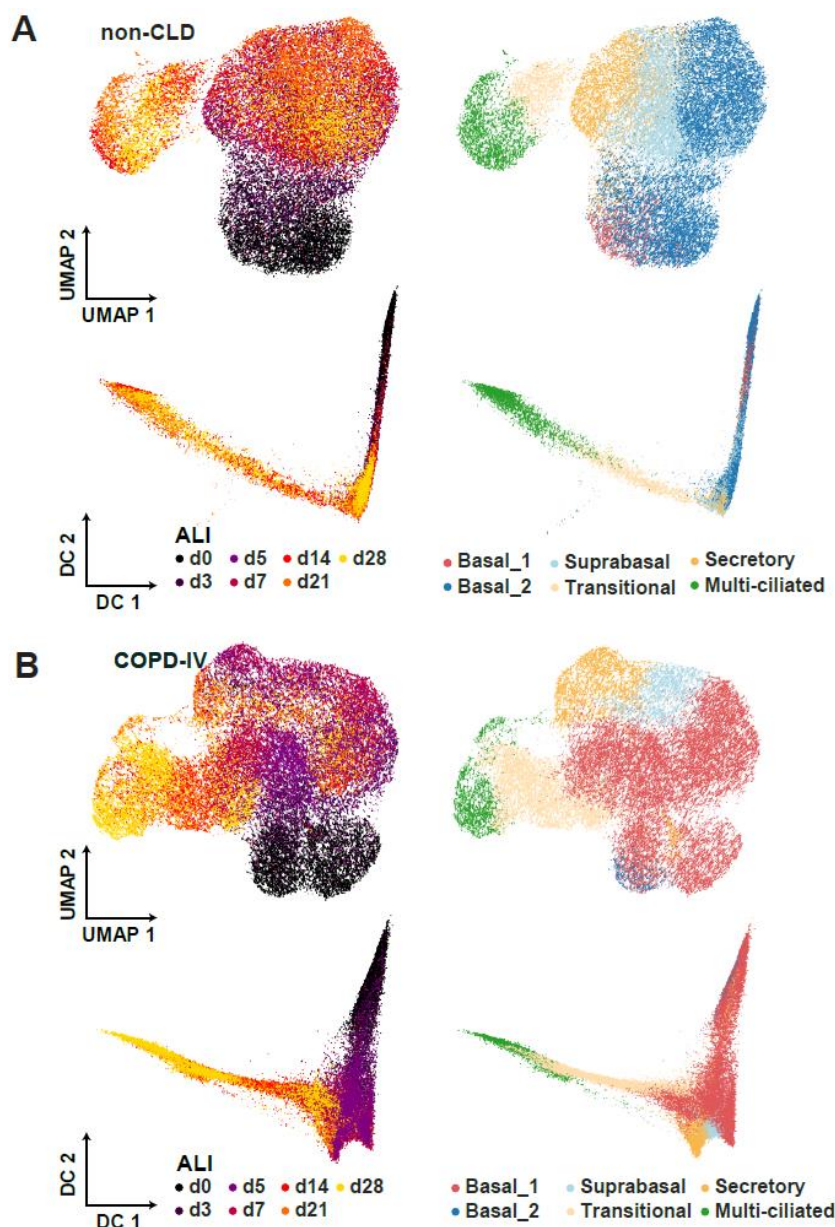
Figure 39: Longitudinal single cell RNA-seq analysis with focus on the **(A, B)** Uniform Manifold Approximation and Projection (UMAP) and diffusion map (DC) embeddings for different timepoints of sampling and cell type subpopulations in both non-CLD **(A)** and COPD-IV cultures **(B)**. For both cultures the cell trajectory between ALId0 and d28 was presented. Accordingly basal cells are progenitors for suprabasal and secretory cells (ALId0-7). Mature secretory cells (ALId14) give rise to transitional cells (intermediate pre-ciliated cells, ALId14-21), which give rise to end-differentiated multi-ciliated cells (ALId21-28). COPD-IV cultures are characterized by an elevated number of secretory and transitional pre-ciliated cells (lower branch of cell trajectory/ DC1), that induce an impaired terminal differentiation into multi-ciliated cells.

In addition, an intermediate cell state characterized by co-expression of secretory and MCC marker genes has been observed during the whole time of cell differentiation. This transitional cell state indicates that SC give rise to MCC during differentiation process, in accordance with the current model of human airway lineage hierarchy [2]. Accordingly, the transitional cells were localized on UMAP diffusion map between secretory and MCC populations (**Figure 39**). Specific gene clusters of the independent cell populations of the bronchial epithelium were systematically compared with those previously published in the single cell atlas of the healthy human airways[2]. These clusters were correlated with the reported marker genes of the *in vivo* cultures via matchScore method. By using this approach, our pHBECs culture accurately defined *in vivo*-like cell subtypes in both non-CLD and COPD-IV derived cultures (**Figure 40**).
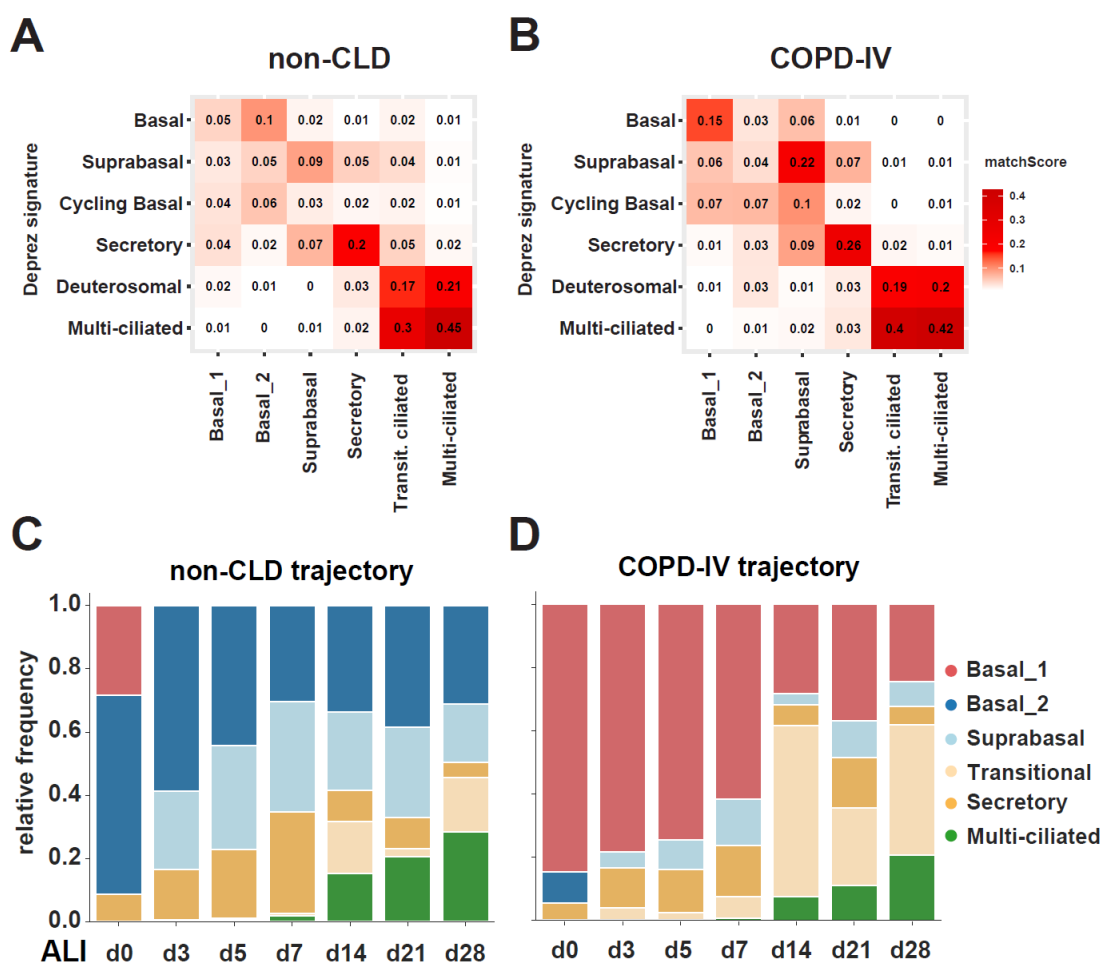
Figure 40: Longitudinal single cell RNA-seq analysis with focus on the altered cell differentiation in COPD-IV cultures in comparison to the non-CLD cultures. For all sampling timepoints, longitudinal single cell RNA-seq drop-seq analysis was correlated with previous gene datasets that characterize the pHBECs subpopulations [2]. (**A, B**) The matchScore coefficients for non-CLD and COPD-IV derived cultures indicate the transcriptional similarity for all pHBECs cell subpopulations based on the previous reference dataset [2]. (**C, D**) Relative frequency of the pHBECs subpopulations during the whole time of differentiation in non-CLD (**C**) and COPD-IV (**D**) cultures, showing a higher amount of transitional pre-ciliated cells and a low amount of multi-ciliated cells in COPD-IV cultures, in the context of an impaired terminal cell differentiation.

Interestingly, two independent BC subtypes were identified (basal_1, basal_ 2) with a good overlap within health status and a strong shift between non-CLD and COPD-IV cultures at ALI (**Figure 40**). We observed a mixture of these states on ALId0, with basal_1 state predominantly observed in COPD-IV cultures and basal_2 state in non-CLD controls. This mixture was present during whole time of ALI culture until ALId28. The pHBECs differentiation axis was characterized by the appearance of sBC and SC in the early phase of cell differentiation on ALId3-7, followed by the differentiation of SC into MCC from ALId14 onwards (**Figure 40**). Interestingly, the outlined cell differentiation axis was respected in both non-CLD and COPD-IV cultures. In particular, COPD-IV cultures were characterized by an accumulation of transitional cells and reduced amount of end-differentiated MCC, suggesting an altered terminal cell differentiation potential in diseased cultures (**Figure 40**).

To analyze the cell proliferation process, single cell RNA analysis for specific cell subpopulations using proliferation markers (e.g. $MKI67^+$, $TOP2A^+$) was performed. Accordingly, COPD-IV cultures were characterized by an increased amount of proliferating BC and sBC with a peak on ALId21 (**Figure 41**). The amount of proliferating MCC in COPD-IV cultures was lower in comparison to the non-CLD cultures.
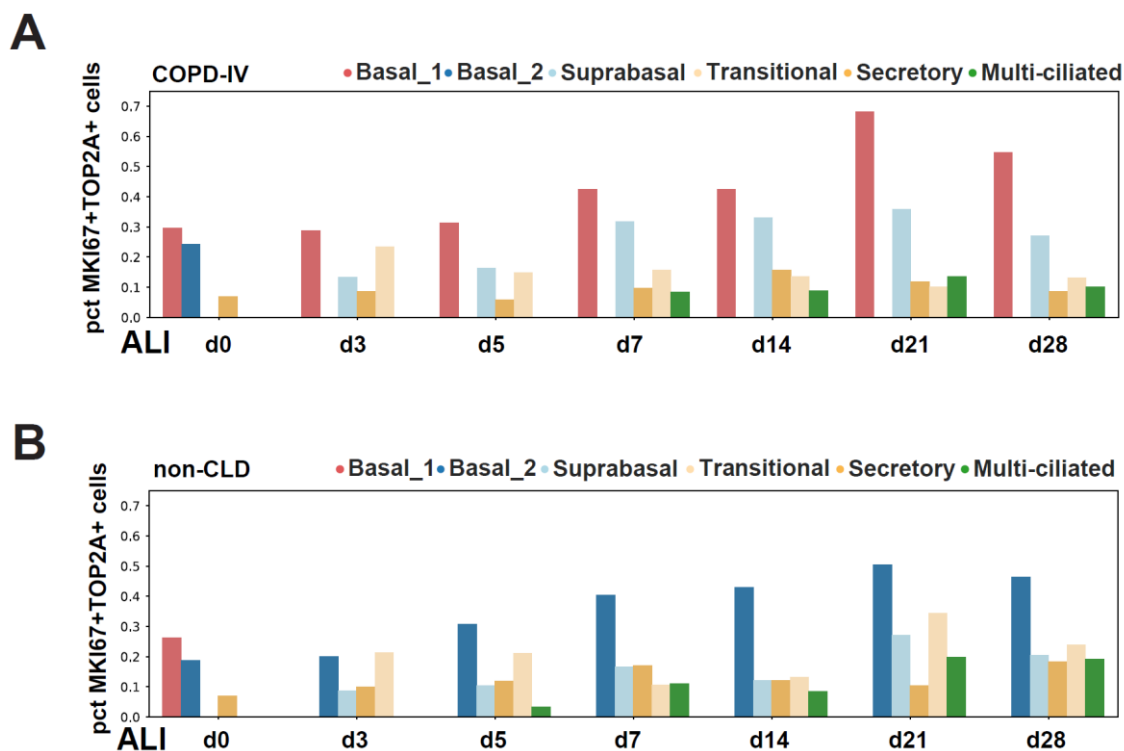
Figure 41: Longitudinal single cell RNA-seq analysis with focus on the quantification of the proliferating cells ($MKI67^+$, $TOP2A^+$) reported for the particular cell subpopulations during the whole time of differentiation (ALId0, 3, 5, 7, 14, 21 and 28) in both non-CLD and COPD-IV cultures: COPD-IV cultures revealed an increased amount of proliferating basal and suprabasal cells with a peak on ALId21, as well as a lower amount of proliferating multi-ciliated cells **(A)** when compared to non-CLD cultures **(B)**. Non-CLD cultures were characterized by an increased amount of proliferating transitional cells, explaining the higher amount of multi-ciliated cells when compared to COPD-IV cultures.

In the next step, a comprehensive analysis of differential gene markers for BC on ALId0 and for all cell subpopulations on ALId28 was performed (**Figure 42**).
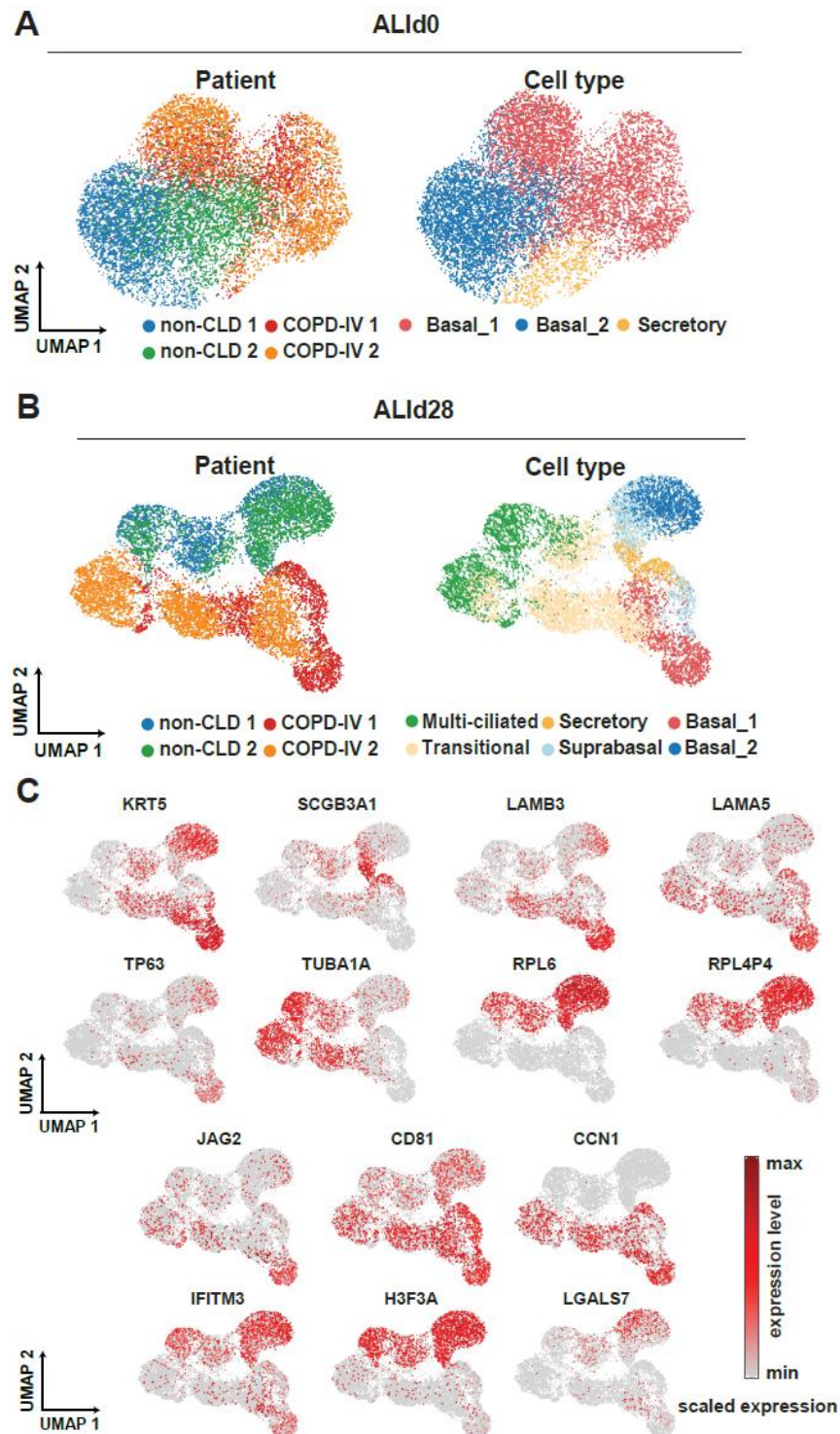
Figure 42: Longitudinal single cell RNA-seq analysis with focus on the comparative Uniform Manifold Approximation and Projection (UMAP) representations for pHBECs on ALId0 **(A)** and ALId28 **(B)** derived from both non-CLD and COPD-IV cultures. On ALId0 two independent basal cell populations (basal_1 in COPD-IV and basal_2 in non-CLD) were identified. On ALId28 end-differentiated cultures were dominated by secretory, transitional and multi-ciliated cells. **(C)** Feature plots illustrating the UMAP representations for specific marker genes that define the two basal cell populations on ALId28 (basal_1 – KRT5^{+}, LAMB3^{+} and basal_2- RPLP[+]).

The presence of BC populations was validated via IF stainings of native bronchi in both healthy and diseased patients. The average intensity of basal_1 cells (KRT$^+$ and LAMB3$^+$) was significantly higher in COPD-IV bronchi. In contrast, the average intensity of basal_2 cells (RPLP1$^+$) was significantly higher in non-CLD bronchi (**Figure 43**).
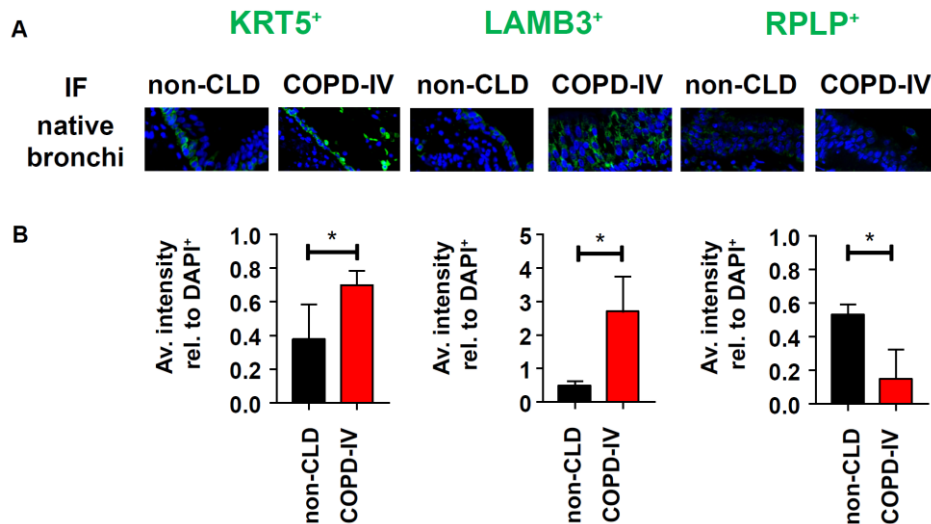
Figure 43: Immunofluorescence stainings **(A)** and quantification **(B)** of non-CLD and COPD-IV native bronchi, revealing a misaligned bronchial epithelium with disorganized basal cells in COPD-IV when compared to non-CLD cultures **(A)**. Whereas basal cells_1 were predominately present in COPD-IV (increased average intensity for KRT$^+$ and LAMB3$^+$), basal cells_2 were the main cell population of the non-CLD cultures (increased average intensity for RPLP1$^+$) **(B)**.

Differentially expressed genes for basal_1 and basal_2 cell subtypes were analyzed on both ALId0 and ALId28. A heatmap illustrating the differentially expressed genes that characterize the BC on ALId0 and ALId28 is presented in **Figure 44.** These gene clusters were involved in survival mechanisms towards injury in COPD-IV cultures.
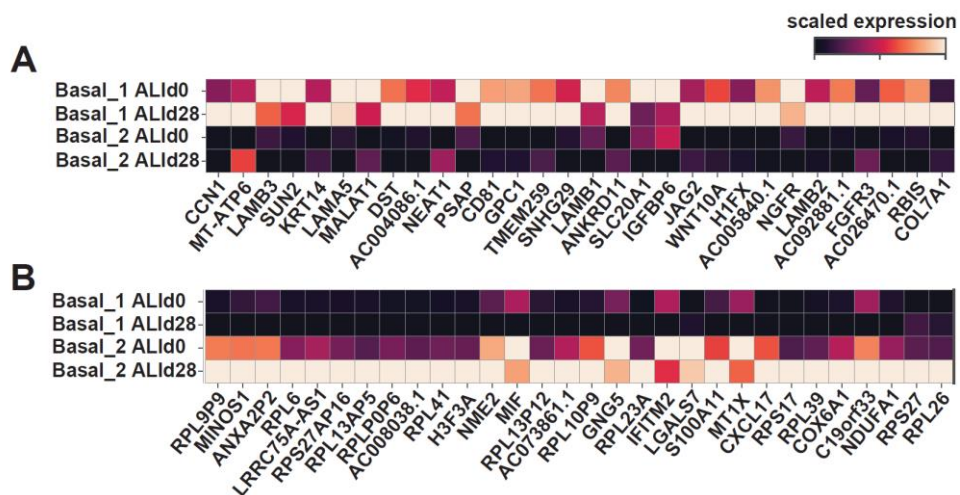
Figure 44: Longitudinal single cell RNA-seq analysis with focus on the top 30 significantly **(A)** up-regulated and **(B)** down-regulated differentially expressed genes (DEG) that define the basal_1 and basal_2 populations on ALId0 and ALId28 in both non-CLD and COPD-IV cultures. Upregulated DEG in COPD-IV cultures are associated with a secretory differentiation, ECM remodeling processes and pro-survival mechanisms.

Enrichment analysis revealed that COPD-IV specific basal_1 cells were characterized by increased levels of ECM components, together with overrepresented Wnt and Notch signaling pathways as resulted from the Gene ontology processes (**Figure 45**).
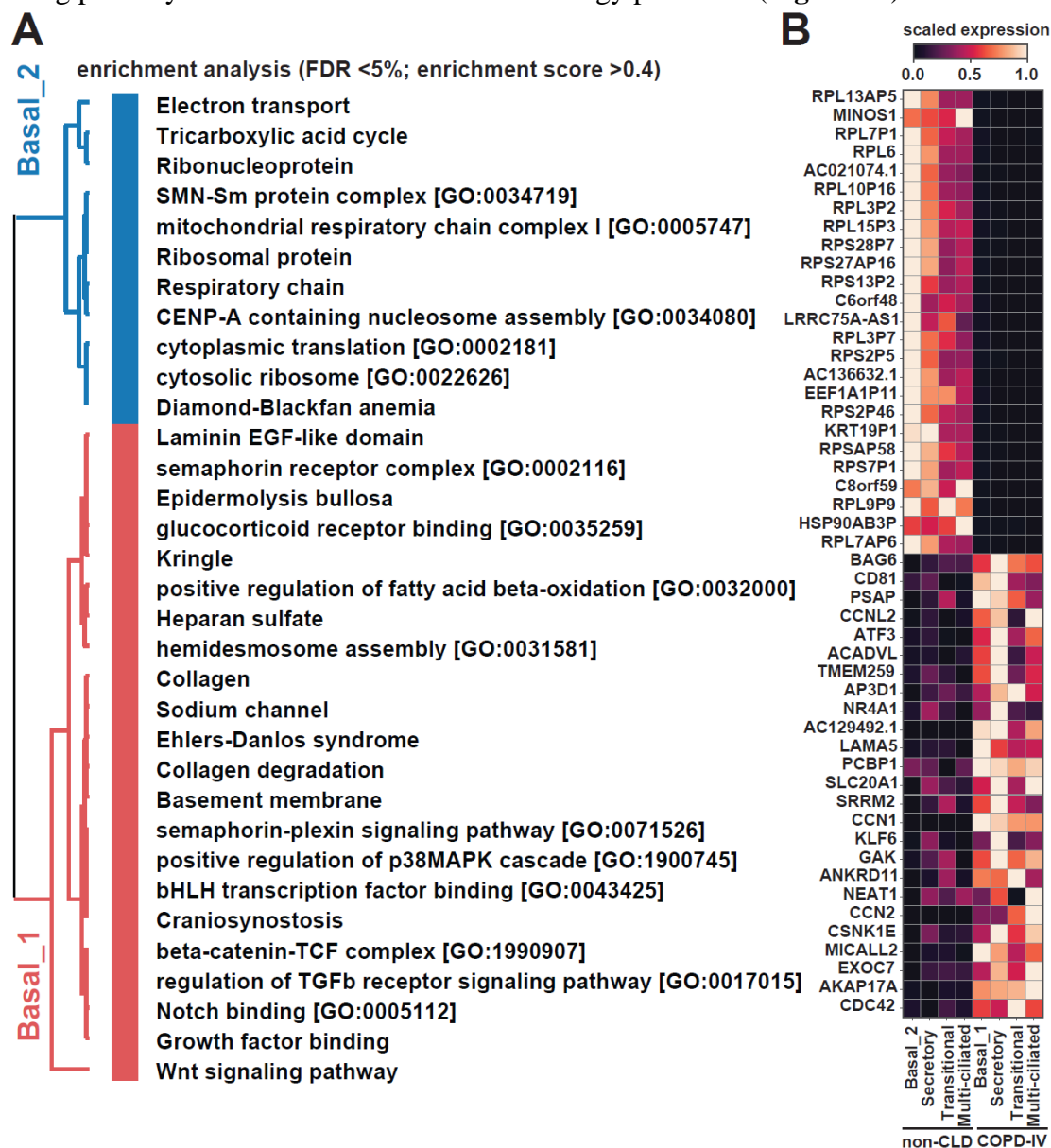
Figure 45: Longitudinal single cell RNA-seq analysis with focus on (**A**) the significantly enriched GO terms for basal_1 and basal_2 cells (FDR < 5%) and (**B**) the top 25 up- or downregulated genes for all cell types from both non-CLD and COPD-IV cultures on ALId28. Enrichment analysis of basal_1 cells revealed an overrepresentation of pathways involved in extracellular matrix (ECM) remodeling, as well as cell regeneration and repair mechanisms in COPD-IV (e.g. Notch and Wnt). Upregulated differentially expressed genes in COPD-IV are associated with a secretory differentiation, ECM remodeling and prosurvival mechanisms.

These findings were in line with transcriptome data, that confirmed the transcription of ECM components in COPD-IV pHBECs (i.e. dermatan/ chondroitin/ and heparan sulfate), when compared to non-CLD cultures. Airway remodeling processes in COPD-IV pHBECs were activated by Wnt pathway. The main canonical pathways derived from the Ingenuity Pathway Analysis® of bulk transcriptome in diseased and healthy cultures are summarized in **Table 33**.

Ingenuity Pathway Analysis® (baseline COPD-IV vs non-CLD)	-log (*P*-value)	Molecules
EIF2 Signaling	12.3	AGO1, BCL2, CCND1, EIF2AK3, EIF2AK4, NKX6-2
mTOR Signaling	5.25	ATG13, EIF3F, GPLD1, HMOX1, MAPKAP1, PDGFC
Regulation of eIF4 and p70S6K Signaling	3.34	AGO1, EIF3F, ITGA3, MAPK14, PIK3CA, PPP2R2C
Chondroitin Sulfate Biosynthesis	2.98	B3GAT3, CHPF, CHST12, CHST15, CHST5, HS2ST1
Dermatan Sulfate Biosynthesis	2.77	B3GAT3, CHPF, CHST12, CHST15, CHST5, HS2ST1
Chondroitin Sulfate Biosynthesis (Late Stages)	2.48	CHPF, CHST12, CHST15, CHST5, HS2ST1, HS3ST1
Triacylglycerol Biosynthesis	2.44	AGPAT3, DGAT1, ELOVL1, GPAT2, GPAT4, MBOAT7
RAN Signaling	2.1	CSE1L, KPNA4, KPNA6, RAN, RANBP1
Dermatan Sulfate Biosynthesis (Late Stages)	2.09	CHST12, CHST15, CHST5, HS2ST1, HS3ST1, HS3ST3A1
Tight Junction Signaling	1.96	CLDN1, CLDN10, CLDN12, CLDN4, CLDN7, CPSF1
Heparan Sulfate Biosynthesis	1.94	B3GAT3, CHST12, CHST15, EXT2, HS2ST1, HS3ST1
Regulation of Actin-based Motility by Rho	1.87	ARPC1B, GSN, ITGA3, LIMK1, RHOBTB2, RHOJ
Wnt/β-catenin Signaling	1.82	SOX4, TGFB3, WNT10B, WNT5A, WNT7B, WNT9B
CDP-diacylglycerol Biosynthesis I	1.79	AGPAT3, GPAT2, GPAT4, MBOAT7, TAZ
Sirtuin Signaling Pathway	1.71	ABCA1, ADAM10, ATG101, ATG13, ATG16L1
Actin Cytoskeleton Signaling	1.69	ACTN1, ARHGEF4, ARPC1B, CD14, F2R, ITGA3
Inhibition of Matrix Metalloproteases	1.54	ADAM10, ADAM12, MMP10, MMP14, MMP15, MMP2
Heparan Sulfate Biosynthesis (Late Stages)	1.49	CHST12, CHST15, CHST5, HS2ST1, HS3ST1, HS3ST3A1
Human Embryonic Stem Cell Pluripotency (Wnt)	1.49	ACVR1, BMP1, TGFBR2, WNT10B, WNT5A, WNT7B
PTEN Signaling	1.46	BCL2, CCND1, IGF1R, ITGA3, RAP2A, TGFBR2

Table 33: Ingenuity Pathway Analysis® derived from bulk transcriptome analysis of unexposed COPD-IV vs non-CLD cultures on ALId28 showing the overrepresentation of pathways involved in extracellular matrix remodeling (ECM) and epithelial-to-mesenchymal transition (EMT) that reflect airway remodeling processes in COPD-IV derived cultures when compared to non-CLD cultures. At baseline level these processes are partially regulated by Wnt signaling pathway. For each regulated pathways the statistical significance (-log(*P*-value)) and the representative genes were summarized. Datasets of regulated genes were defined by raw *P*-values < 5% and -log(*P*-value) > 1.3 by using a fold change (FC) gene expression filter ≥ 1.3.

Analogously, exposure to ZnO NPs activated ECM remodeling and Notch signaling in COPD-IV cultures. The main canonical pathways derived from the Ingenuity Pathway Analysis® in ZnO exposed cultures are summarized in **Table 34**.

Ingenuity Pathway Analysis® (ZnO exposed COPD-IV vs non-CLD)	-log (*P*-value)	Molecules
Cell Cycle Regulation by BTG	2.16	CCNE1, E2F8, PPP2R3A
Notch Signaling	2.13	APH1A, DTX1, NOTCH3
Th1 Pathway	2.03	APH1A, HLA-DQB1, ICAM1, NOTCH3, TNFSF11
Cyclins and Cell Cycle Regulation	1.98	CCNE1, CDKN2C, E2F8, PPP2R3A
Dermatan Sulfate Biosynthesis (Late Stages)	1.9	HS3ST6, SULT1A1, SULT1A2
Chondroitin Sulfate Biosynthesis (Late Stages)	1.85	HS3ST6, SULT1A1, SULT1A2
Chondroitin Sulfate Biosynthesis	1.68	HS3ST6, SULT1A1, SULT1A2
Dermatan Sulfate Biosynthesis	1.62	HS3ST6, SULT1A1, SULT1A2
Tumoricidal Function of liver NK Cells	1.58	ICAM1, SRGN
CDK5 Signaling	1.56	ADCY6, CACNA1A, MAPK7, PPP2R3A
Estrogen-mediated S-phase Entry	1.52	CCNE1, E2F8
S-adenosyl-L-methionine Biosynthesis	1.51	MAT2A
Cell Cycle: G1/S Checkpoint Regulation	1.47	CCNE1, CDKN2C, E2F8
Th1 and Th2 Activation Pathway	1.45	APH1A, HLA-DQB1, ICAM1, NOTCH3, TNFSF11
Dopamine Degradation	1.4	SULT1A1, SULT1A2
ERK5 Signaling	1.39	BAD, MAPK7, NTRK1
Heparan Sulfate Biosynthesis (Late Stages)	1.34	HS3ST6, SULT1A1, SULT1A2
p70S6K Signaling	1.32	BAD, F2R, PDPK1, PPP2R3A
Dopamine Receptor Signaling	1.32	ADCY6, PPP2R3A, SLC18A2
Th2 Pathway	1.25	APH1A, HLA-DQB1, ICAM1, NOTCH3

Table 34: Ingenuity Pathway Analysis® derived from bulk transcriptome analysis of ZnO (0.14 cm^2/cm^2) exposed COPD-IV vs non-CLD cultures on ALId28 showing the overrepresentation of pathways involved in extracellular matrix remodeling (ECM) and epithelial-to-mesenchymal transition (EMT) in ZnO challenged COPD-IV cultures when compared to non-CLD cultures. These processes are partially regulated by Notch signaling pathway. For each regulated pathway statistical significance (-log(*P*-value)) and representative genes were summarized. Datasets of regulated genes were defined by raw *P*-values < 5% and -log(*P*-value) > 1.3 by using a fold change (FC) gene expression filter ≥ 1.3.

In strong contrast, basal_2 cells, predominately observed in non-CLD cultures, presented an increased expression level of ribonucleoprotein and mitochondrial respiratory complexes involved in the tricarboxylic acid cycle (**Figure 46**). In addition, gene expression profiles of basal_1 and basal_2 cells suggested potential epigenetic differences in COPD-IV vs non-CLD cultures. Specifically, the presence of variant histone H3 (H3F3A) as epigenetic imprint of transcriptionally active chromatin was almost exclusively observed in non-CLD cultures in basal_2 cells as well as secretory and MCC[126].

In the next step, differential gene expression was systematically performed in both non-CLD and COPD-IV cultures in order to point out the particular gene clusters that characterize the studied cell subtypes. These changes were present on gene set level and pathway enrichment analysis.

Specifically, the expression of the cytosolic ribosomal machinery found in non-CLD cultures was preserved in all cell types and all timepoints during the cell differentiation (**Figure 46**).
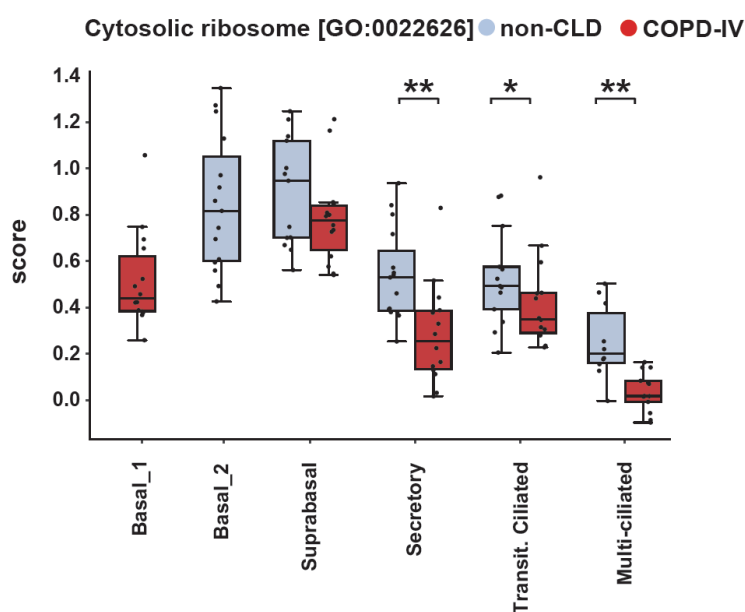
Figure 46: Longitudinal single cell RNA-seq analysis with focus on the gene signatures that define the GO term "cytosolic ribosome" in both non-CLD and COPD-IV cultures on ALId28, indicating an increased expression level of the ribonucleoprotein involved in the tricarboxylic acid cycle in non-CLD specific basal_2 cells. These findings were preserved for all cell types and at all timepoints during the cell differentiation process. For each GO term, datasets of regulated genes were defined by adjusted P-value < 0.05. Comparisons between groups were performed by using Wilcoxon rank-sum test and Bonferroni multiple testing correction (* adjusted P-value < 0.05, ** adjusted P-value < 0.005).
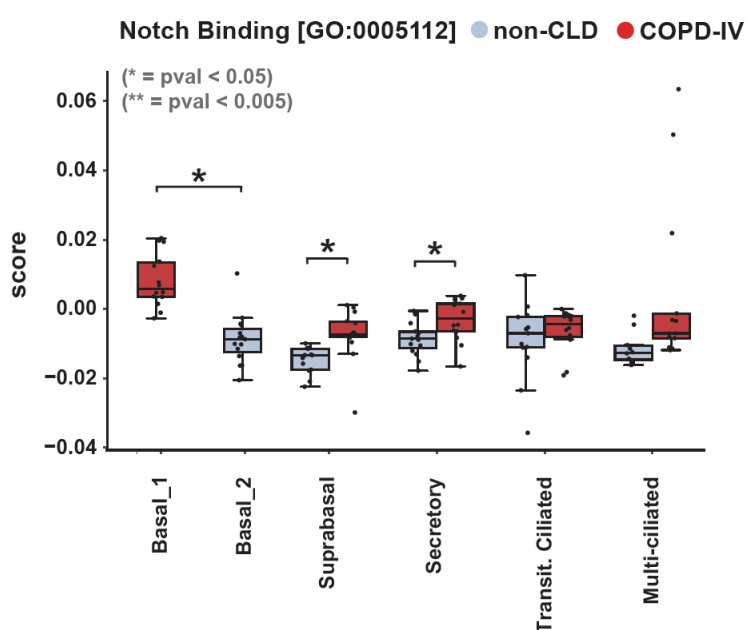
In strong contrast, the increased gene expression level for Notch pathway in COPD-IV (i.e. notch-ligand Jagged-2 (JAG2)) was conserved from basal stem cells (basal_1) to the secretory cells (**Figure 47**).

Figure 47: Longitudinal single cell RNA-seq analysis with focus on the gene signatures that define the GO term "Notch binding" in both non-CLD and COPD-IV cultures on ALId28, indicating an increased expression level of the Notch signaling pathway involved in cell differentiation, regeneration and repair mechanisms in COPD-IV specific basal_1 cells. These findings were preserved for all cell types and at all timepoints during the cell differentiation process in COPD-IV cultures. For each GO term, datasets of regulated genes were defined by adjusted P-value < 0.05. Comparisons between groups were performed by using Wilcoxon rank-sum test and Bonferroni multiple testing correction (* adjusted P-value < 0.05, ** adjusted P-value < 0.005).

Specifically, Notch pathway was involved in the SC-MCC axis differentiation by down-regulating the MCC genes and thus facilitating a hypersecretory phenotype[127]. The involvement of Notch pathway in the differentiation axis of COPD-IV cultures starting with ALId14 onwards was in line with the reported transcriptome data.

The gene expression level involved in the Notch pathway was further analyzed upon moderate ZnO (0.14 cm^2/cm^2) exposure in both COPD-IV and non-CLD cultures. Accordingly, Notch signaling pathway was predominantly observed in ZnO exposed COPD-IV cultures, indicating that ZnO activates genes involved in pHBECs renewal and repair thus facilitating secretory cell survival[128].

In addition, the interaction between Notch and TGF beta signaling indicates another survival strategy of the SC upon NP exposure[127].

Of note, Wnt pathway was significantly activated in both basal_1 cells and SC of the COPD-IV cultures (**Figure 48**), in line with the outlined transcriptome data.
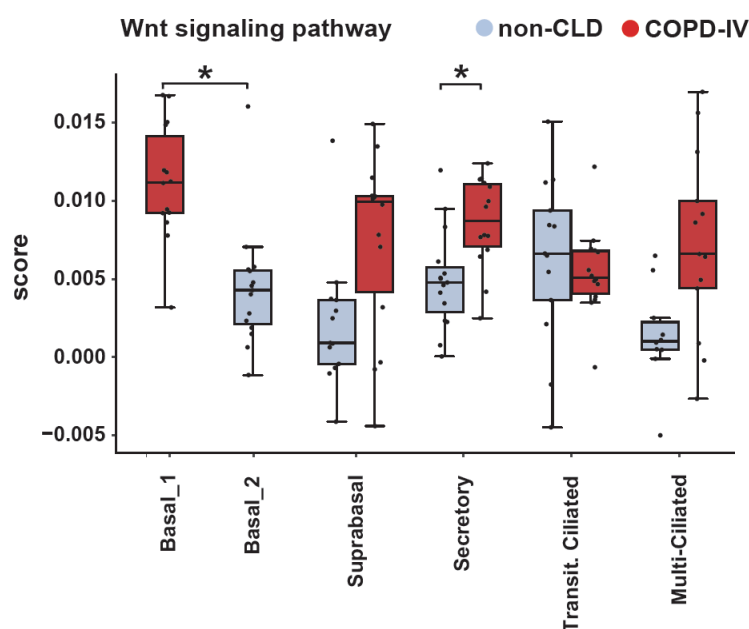
Figure 48: Longitudinal single cell RNA-seq analysis with focus on the gene signatures that define the GO term "Wnt signaling pathway" in both non-CLD and COPD-IV cultures on ALId28, indicating an increased expression level of the Wnt signaling pathway involved in cell differentiation and regeneration in COPD-IV specific basal_1 cells. These findings were preserved for all cell types and at all timepoints during the cell differentiation process in COPD-IV cultures. For each GO term, datasets of regulated genes were defined by adjusted *P*-value < 0.05. Comparisons between groups were performed by using Wilcoxon rank-sum test and Bonferroni multiple testing correction (* adjusted *P*-value < 0.05, ** adjusted *P*-value < 0.005).

Briefly, gene markers involved in Wnt pathway signaling (i.e. SOX4, SOX8, TGFB3, TGFBR2, TLE1, WNT10B/ 5A/ 7B / 9B) were significantly enriched in COPD-IV cultures at baseline level[129,130].

Exposure to moderate ZnO NP activated Wnt and TGFB pathway components (i.e. AKT3, ALPL, IL1F10, IL1RAPL2, IL1RN, IL36G, LEF1, NAIP, SFRP4, SMAD9, TNFRSF1B, TNFSF11, WIF1, WNT5A, WNT5B) that silence the terminal differentiation of transitional cells into MCC, as previously reported [131,132].

3.3 Results summary

Given the transcriptional similarity between the single cell RNA-seq analysis and the air-way single cell atlas[2], as well as between the pHBECs ALI cultures and the native bronchial tissue samples, following considerations could be stated:

i)   MCC was the dominant cell subtype in the non-CLD cultures being significantly lower represented in COPD-IV cultures (lowest amount in the early phases of cell differentiation, ALId0-14).

ii)   SC signature was higher in COPD-IV cultures, reflecting the oligo-ciliated and hypersecretory phenotype of COPD-IV cultures that was validated by transcriptome and IF analysis. This phenotype was also reported for particular gene markers for MCC (TUBA1A$^+$), secretory CC (SCGB1A1$^+$) or secretory GC (MUC5B$^+$) at different timepoints during cell differentiation.

iii) The two particular BC gene signatures (basal_1, basal_2) persisted during the course of cell differentiation in both non-CLD and COPD-IV cultures. The presence of BC populations was validated via IF of native bronchi from healthy and diseased patients. The average intensity of basal_1 cells (KRT$^+$, LAMB3$^+$) was significantly higher in COPD-IV bronchi and of basal_2 cells (RPLP1$^+$) in non-CLD bronchi.

iv)   Non-CLD cultures were characterized by a gradual increase in the secretory and MCC gene signatures until ALId28, in accordance with IF quantification of non-CLD cultures. These gene signatures were inversely regulated in COPD-IV cultures and were validated by IF stainings of the native human bronchi in both healthy and diseased cultures. Accordingly, a significant increase in MUC5AC$^+$ SC, together with an unchanged amount of CC10$^+$ SC and MCC in COPD-IV cultures were observed.

With regards to the NP exposure following considerations could be stated:

i)   Inflammagenic pollutants (LPS and CNP) did not affect the barrier integrity, electrical membrane resistance, viability and relative frequency of pHBECs at ALI at selected doses, 24 hours upon exposure.

ii)   ZnO induced a concentration-dependent and disease-specific response with an preserved barrier integrity, electrical membrane resistance and cell viability in NP exposed COPD-IV derived cultures. ZnO did not significantly affect the relative cell frequency of COPD-IV derived cultures.

In conclusion, the particular BC signature in COPD-IV cultures led to an impaired terminal differentiation of secretory GC into MCC. The greater functional resilience of COPD-IV cultures towards environmental NP might be explained by the unsuccessful drive to induce trans-differentiation of the SC into MCC and the hypersecretory oligo-ciliated phenotype characterized by a high amount of resilient SC and a small amount of vulnerable MCC.

4.   Discussion

4.1   Study design and experimental approach

The respiratory epithelium is continuously challenged to a variety of toxic environmental pollutants that largely impacts on lung health. Although the causality between COPD and air pollution has been extensively described [45,133,134], the resulted injury at the level of bronchial epithelium remains a still insufficiently characterized topic. Given the lack of mechanistic toxicologic studies, our study aimed to analyze compositional and functional changes of the human bronchial epithelium upon NP exposure.

To address this topic, we:

i) established a physiological long-term 3D ALI culture using pHBECs from diseased (COPD-II and -IV) and healthy patients

ii) exposed the enddifferentiated ALI cultures to relevant environmental pollutants by using the pre-clinical, highly standardized VITROCELL® CLOUD 12 exposure system in order to highlight particular post-exposure changes and repair mechanisms

iii) described for the first time particular features in non-CLD and COPD-IV bronchial epithelium with focus on the distinct BC populations regulating the SC-MCC differentiation axis and muco-ciliary machinery of the bronchial epithelium.

By the use of this unique setting, our project realistically mimicked the effects of environmental pollution on the proximal airways in both healthy and diseased patients.

Preliminary findings on the impaired SC-MCC differentiation axis were reported in asthma [135,136] and cystic fibrosis [137,138], but remained insufficiently characterized in end-stage COPD. Thus, our study adds valuable data regarding the altered SC-MCC axis differentiation of the human bronchial epithelium at baseline level and upon environmental NP exposure, facilitating a better understanding of COPD disease pathomechanisms with potential preventive and therapeutic implications.

4.2   Exposure setting

Environmental exposure effects at the level of human airways were previously addressed by using cigarette smoke extract or different NP families. Cigarette smoke exposure[139,140] and NP exposure[141,141–143] of human airway epithelium were previously performed under submerged or ALI conditions. ALI exposure systems are preferred over the unphysiological submerged cultures, due to the more realistic simulation of the air liquid interface and physiological NP application route. Besides different ALI exposure systems, the VITROCELL®CLOUD technology (VITROCELL® CLOUD 12, VITROCELL Systems, Waldkirch, Germany) used in our study enabled a homogenous distribution of the NP on the whole surface of the ALI transwells[143,144].

By the use of these unique exposure settings, our study combined for the first time a realistic, long-term biomimetic 3D pHBECs culture model at ALI with a preclinical, highly standardized NP cell exposure system. This experimental approach was comparatively applied in healthy and end-stage lung disease patients to assess the pathophysiologic changes that take place at the level of human bronchial epithelium upon environmental toxin exposure. The pathophysiologic changes post-exposure observed in COPD-

IV cultures were outlined in functional (TEER, WST-1, LDH release, transcriptome and secretome) and compositional (IF, single cell) analyses.

Our study made use of two inflammagenic pollutants (LPS, CNP) and two different doses of a cytotoxic environmental pollutant (ZnO). Even though LPS and CNP were used as ubiquitous particles present in the environmental air of highly industrialized cities, their accumulation on respiratory system might provoke a dose dependent infectious (LPS, *Pseudomonas aeruginosa*[145,146]) or non-infectious (carbon NP[147]) acute airway injury.

4.2.1 ZnO exposure

Upon moderate ZnO exposure, cell composition in COPD-IV was stable, with an unchanged amount of viable SC in the presence of a very low amount of apoptotic cells, as resulted via LDH release assay. These findings indicate a decreased secretory cell vulnerability at baseline level and upon NP exposure. Interestingly, ZnO NP were able to penetrate the thicker mucus film of the muco-ciliary escalator in COPD-IV, translocate into the cells, and provoke cell toxicity. Intracellular translocation of ZnO NP previously described by Xia et al. [148] was demonstrated in our study by the upregulation of metallothioneins involved in mineral ion homeostasis. These effects were stronger in COPD-IV due to the impaired ciliary beating of MCC and inefficient muco-ciliary clearance. Furthermore, moderate ZnO exposure provokes lysosomal damage, autophagy, excessive OS as well as cell death in accordance with previous studies[149,150]. These findings are accompanied by an overrepresentation of OS pathways (e.g. Notch-signaling) in ZnO-exposed COPD-IV cultures in comparison to the non-CLD cultures.

ZnO exposure induced a dose-dependent reduction of barrier function, cell membrane integrity and viability in both non-CLD and COPD-IV patients. Comparable results were reported upon titanium dioxide (TiO_2) exposure [151,152]. One potential explanation might be the particular exposure vulnerability for different cell populations of the bronchial epithelium. Leibrock et al. addressed this aspect by comparing immortalized squamous type-II cells (A549 cells) with human primary airway epithelial cells (huAEC). Accordingly, the squamous epithelium was found to be more resilient in comparison to the huAEC. In strong contrast, huAEC were found to be more susceptible for cytotoxic effects upon NP exposure [141].

Of note, the susceptibility of MCC towards cell injury was observed upon viral infection. Specifically, MCC have been identified as main targets for pathogenic viruses like SARS-CoV-2, Influenza or Rhinovirus[153,154]. Our results could suggest an increased NP-related vulnerability of MCC (when compared to the SC) accompanied by a pathologic CBF spectrum and aberrant muco-ciliary machinery.

4.2.2 CNP and LPS exposure

Even though CNP dose was 4-fold higher in comparison to ZnO dose, CNP NPs did not affect the barrier integrity and viability of the pHBECs cultures. These findings were in line with previous reports on Calu-3 ALI cultures in animal models [155,156] being explained by the higher surface-specific inflammogenicity of ZnO NPs when compared to the CNP NPs [157,158]. A second explanation is the more effective mucus penetration of ZnO NPs

when compared to CNP NPs, reflected in the overexpression of metallothioneines upon ZnO exposure.

Interestingly, a repetitive CNP exposure did not additionally affect the cell barrier integrity and viability in comparison to a single CNP exposure. These results were contradicted by previous studies based on repetitive exposures with diesel exhaust particles, that affected cell composition and epithelial function in a dose dependent manner [159,160].

Similarly, nebulized LPS particles are capable to induce inflammatory effects at the level of bronchial epithelium, with comparable responses in both non-CLD and COPD cultures. However, LPS is capable to induce concentration-dependent effects (e.g. inflammation, oxidative stress[161] and apoptosis[162]) not addressed in our study. Interestingly, both non-CLD and COPD cultures were characterized by transcriptional activation of similar proinflammatory gene clusters (e.g. FCGBP, PI3, SAA1, CXCL3/5/6, S100A8). These findings suggest that LPS exposed COPD-IV pHBECs are capable to activate proinflammatory defense responses without affecting cell viability, integrity and barrier resistance, thus reflecting the epithelial resilience of the diseased bronchial epithelium.

4.3   COPD-IV phenotype in the context of chronic toxin exposure

Bronchial epithelium continuously suffers adaptive changes upon environmental toxin exposure. Accordingly, a gradual decrease of cell barrier resistance, viability and membrane integrity was observed at baseline level and upon NP exposure in both non-CLD and COPD cultures.

Interestingly, the present study showed that chronic toxin exposure (e.g. CSE) facilitates COPD disease progression. COPD-II CSE pHBECs showed decreased cell barrier integrity values, that were comparable to those seen in COPD-IV cultures. Accordingly, confocal IF stainings revealed an almost similar cell composition pattern in COPD-II CSE cultures when compared to COPD-IV cultures. Specifically, CSE exposure led to a predominant presence of SC, in accordance with the hypersecretory and oligo-ciliated phenotype seen in COPD-IV cultures. These findings were in line with previous studies that characterize compositional changes upon CSE in COPD cultures [107,163–166]. Altogether, our study simulated COPD disease progression at ALI and highlighted cell compositional similarities in COPD-IV and COPD-II derived cultures treated with CSE, in line with previous studies on COPD development and progression [107,112,167,168].

COPD-IV bronchial epithelium was characterized in the present study by GC expansion and a low amount of MCC, together defining the oligo-ciliated hypersecretory phenotype. Consecutively, GC proliferation and apical mucus accumulation could explain the increased resilience of COPD-IV pHBECs against environmental pollutants. These compositional changes post-exposure were in line with data on bronchial epithelial cells upon viral infection [169,170]. Our findings complement the previous data on COPD patients exposed to fine environmental pollutants [171] with cell compositional analysis and single cell trajectories. The cellular composition of our non-CLD cultures was in line with previous results for MCC (47-49%) [78,79] and SC (6-21%) [79,125]. Since MCC are the main cell population of the healthy human bronchial epithelium [107,112], the oligo-ciliated pattern reported in COPD-IV was correlated with an altered differentiation of MCC[172], an aberrant muco-ciliary machinery[172], a pathologic CBF spectrum[173,174 175,176], a reduced cell barrier

integrity[177] and an impaired muco-ciliary clearance [78,172,135,136,178]. In addition, the low number of MCC in COPD bronchi[175] could be the result of an altered SC-MCC differentiation upon chronic use of inhalative and systemic corticosteroids. Moreover, COPD phenotype correlates with a deficient muco-ciliary escalator [175], and thus with abnormal defense responses against environmental pollutants [172]. In particular, an altered muco-ciliary escalator facilitates the accumulation of environmental pro-oxidative toxins (i.e. CNP), with an increased risk of secondary malignant transformation [179,180].

Based on these considerations, we hypothesized that the hypersecretory oligo-ciliated phenotype originates in a skewed SC-MCC differentiation axis characterized by an exhausted pHBECs regeneration, altered trajectory towards SC and impaired differentiation into functional MCC [181,182].

To realistically characterize the compositional changes of the diseased bronchial epithelium at ALI, a novel *ex vivo* culture model based on native bronchial wall tissue samples was developed in our laboratory. This model was based on the previous protocol described by Scott et al., who cultured murine tracheal explants by preserving cell integrity, barrier resistance and tissue architecture[183]. In addition, our model allowed a physiologic ALI culture with preserved native 3D tissue architecture of the airways up to 4 days (vs. only 1 day according to Scott et al.). This model can be used for 3D ALI culture validation and as starting point for further toxicological studies. Our data revealed striking similarities in the cell distribution and morphology between the *ex vivo* cultured BPs and the pHBECs *in vitro* ALI cultures. However, the disadvantages of this model remain the limited culture lifetime and the high risk for culture contamination.

Of note, COPD tissue resilience might be also explained by the squamous cell metaplasia and cell dysplasia, which are common histological features reported in both end-stage COPD and lung cancer [182,184]. Many studies considered end-stage COPD as precancerous state that enhances field carcinogenesis [185,186]. Moreover, lung cancer is considered an "epigenetic continuum" resulted from sustained DNA methylation processes in COPD[187,188]. Since cancer tissue is associated with high resilience and survival, we speculate that functional and compositional alterations observed in COPD-IV could be associated with increased cell survival and resilience upon environmental challenges.

The compositional changes outlined above were further reflected in the transcriptome analysis of the studied cultures. Accordingly, 4 potential explanations for the increased tissue resilience towards environmental NP can be discussed at transcriptome level:

First, pro-survival strategies upon NP exposure found in COPD-IV but not in healthy ALI cultures were mirrored in the differential transcriptional regulation of SPDEF, FOXO1, IL-17C, PPRC1, RELA, LAMC1, IRF3, NRF1, SMAD2/4 and SMARCA4. These genes facilitate cell differentiation towards a hypersecretory phenotype and a deficient terminal differentiation into MCC[169,189]. The hypersecretory phenotype in COPD-IV cultures was activated by NF-$_k$B pathway and regulated by IL-1 and IL-17, in accordance with previous studies [190], indicating the role of IL-17 pathway in the secretory fate of bronchial cell differentiation. Thus, these pathways could explain the increased post-expositional survival of SC in comparison to the more vulnerable MCC.

Second, NP exposure provokes a strong proinflammatory cell response. Specifically, IL-17 and IL-1β-mediated inflammasome facilitates an expansion of the secretory GC that enhance mucus hypersecretion [189,191,192], as protective mechanism against NP exposure.

Third, NP exposure affects the oxidative-antioxidative balance of the cells[193,194]. Protective antioxidative mechanisms reported in the unexposed COPD-IV cultures are reflected in the differential upregulation of OS genes on both transcriptome analysis (HMOX1, EPHX3, TIMP3) and single cell analysis (EPHX1, GSS). The antioxidative effects are also present during phago-, endo- and efferocytosis processes regulated by THBS1, ITGB3, MFGE8, SCARB1, CD36, AXL and FCN2 genes. These processes were previously found to affect cellular resilience and cell survival [195,196].

Forth, transcriptome analysis revealed an overrepresentation of genes involved in ECM and EMT in unexposed COPD-IV cultures when compared to the non-CLD cultures. While ECM facilitates an altered BC differentiation[71] with consecutive goblet cell hyperplasia[197–199], EMT induces squamous cell metaplasia as precancerous disease state [200]. The involvement of ECM und EMT processes in COPD-IV cell differentiation, previously reported by Hedström et al. and He et al. [201,202] indirectly suggests the presence of a distinct cell differentiation pattern at the level of diseased human bronchial epithelium.

4.4 Basal cell trajectories

In order to identify compositional differences of the studied ALI cultures, single cell RNA-seq analysis was performed on 7 different timepoints during cell differentiation. It is known that proximal bronchial epithelium originates in the primary bronchial epithelial cells. Besides their role in cell-cell interactions, metabolism and host defense against infectious [203–206] or non-infectious environmental stimuli [207–209], pHBECs dictate the proliferation and regeneration mechanisms at the level of bronchial epithelium. The present study revealed for the first time two distinct basal cells populations (basal_1, basal_2) for COPD-IV and non-CLD cultures, respectively. Of note, basal_1 cells represents the main cell population of COPD-IV cultures and were present only in a small amount in non-CLD cultures. Conversely, basal_2 cells represented the main cell population of non-CLD cultures being a minority in COPD-IV cultures. Interestingly, distribution of basal_1 and basal_2 cells revealed a strong shift between COPD-IV and non-CLD cultures that persisted during differentiation and increased until ALId28. On ALId28, COPD-IV cultures showed only basal_1 cells, whereas non-CLD cultures only basal_2 cells. These novel findings reflect a particular cell differentiation pattern in COPD-IV in comparison to non-CLD cultures.

Basically, BC differentiate into sBC, which dictate the cell fate of the SC-MCC differentiation axis. Thus, altered BC could affect the SC-MCC differentiation towards hypersecretory phenotype at the expense of the more vulnerable MCC. Our results are in line with previous reports on lung cell atlas[1,2] with SC being considered precursors for MCC. Based on this finding, we correlated the quantification of IF stainings with the analysis of gene kinetics for both secretory and MCC. Accordingly, SC peaked on ALId14 followed by a stable amount until ALId28. Furthermore, ALId14 marked not only the highest amount of the SC, but also the beginning of MCC proliferation that continued until ALId28, in line with the cell trajectory described by Garcia et al.[1]. Interestingly, analysis of cell distribution during cell differentiation showed a more increased amount of BC, secretory and transitional cells in COPD-IV cultures in comparison to non-CLD cultures, in line with the previously described basal cell trajectory[166]. The abnormal basal cell

differentiation is reflected in the aberrant transcriptional activation of genes involved in muco-ciliary machinery that indicates a proliferation failure of the MCC. This aspect was also observed in the single cell analysis revealing an increased number of transitional cells in the late culture phases (ALId21-d28), which were not able to terminally differentiate into functional MCC.

4.5 Main findings of the study (graphical abstract)

The present study revealed a hypersecretory and oligo-ciliated phenotype in COPD-IV cultures as a result of an altered SC-MCC differentiation axis. This skewed SC-MCC differentiation axis in COPD-IV cultures originates in a distinct BC population characterized by particular gene signatures and cell trajectory.

The SC expansion, mucus hypersecretion and low amount of vulnerable MCC are adaptive mechanisms that explain the increased resilience of COPD-IV cultures towards environmental pollutants. The post-exposure resilience of COPD-IV SC could be explained by prosurvival antioxidative mechanisms and ECM remodeling processes.

The main findings of the study are summarized in **Figure 49**.
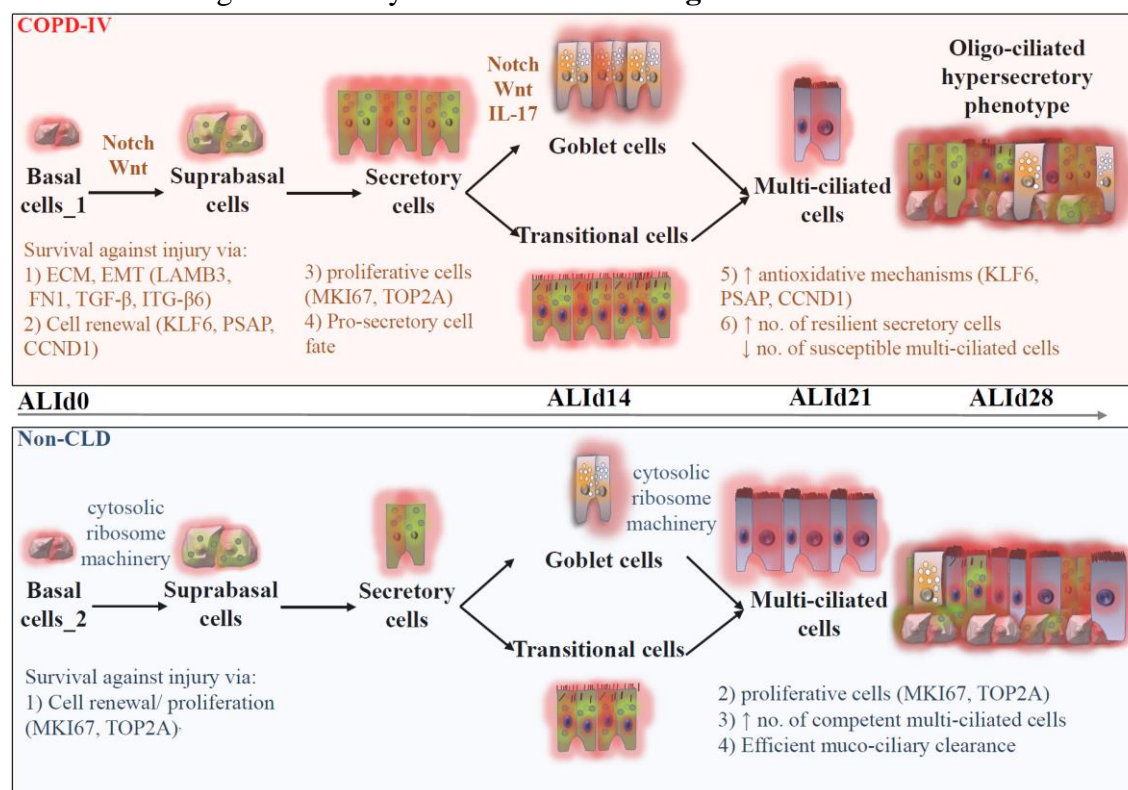
Figure 49: Results summary of the study with focus on the particular pHBECs differentiation trajectories and survival mechanisms against environmental NP injury. COPD-IV derived cultures originate from basal cell_1 that give rise to suprabasal cells, an increased amount of secretory and transitional cells, as well as a decreased amount of multi-ciliated cells. Potential survival mechanisms upon injury in COPD-IV cultures account ECM, EMT processes, Notch, Wnt and IL-17 mediated secretory cell proliferation, as well as strong antioxidative mechanisms of secretory cells. In contrast, non-CLD derived cultures are characterized by the presence of basal cells_2 cells as precursors for suprabasal, secretory and transitional cells that ultimately give rise to an increased amount of multi-ciliated cells. Non-CLD cultures are characterized by an intact cytosolic ribosome machinery as well as a strong repair and proliferation potential of basal cells into terminal competent multi-ciliated cells, that ultimately facilitate an efficient muco-ciliary clearance. ECM - Extracellular matrix remodeling, EMT - Epithelial-to-mesenchymal transition

4.6 Limitation of the study

Our study is based on a low number of cultures derived from n=4 non-CLD, n=3 COPD-II and n=6 COPD-IV patients. This aspect might explain the results heterogeneity and the reduced number of significant findings in transcriptome and single cell data analysis.

Our study used two different cell isolation protocols to derive ALI cultures: Pronase E® protocol (for IF, transcriptome and secretome analysis) and Dispase® protocol (for single cell analysis). This aspect might explain the differences in cell distribution when comparing IF quantification and single cell data.

The chronic administration of local and systemic corticosteroids in COPD-IV patients prior to lung transplantation, as well as supplementation of ALI basal media with hydrocortisone, might bias the inflammatory and oxidative stress responses of the cells upon NP exposure.

4.7 Conclusion

Our results indicate that the predominance of SC in the proximal bronchi of patients suffering from COPD-IV leads to a greater functional resilience towards environmental NP exposure underlined by particular BC populations and the unsuccessful drive to induce trans-differentiation of the SC into competent MCC.

5.   Future directions

Air pollution is a major risk factor for patients suffering from chronic respiratory diseases, as it drives episodes of disease exacerbation and leads ultimately to disease progression. For this reason, it is of critical importance to identify preventive and therapeutic strategies that counteract AECOPD and consecutively disease progression. To achieve these goals, the understanding of cell composition and functional changes at the level of bronchial epithelium upon NP exposure is a mandatory step.

Taking the 3Rs principle (Replacement, Reduction and Refinement) into account, and the urgent need for realistic and physiologic biomimetic systems that simulate the *in vivo* environmental pollutants exposure, following aspects should be discussed and applied in future projects:

a) Cultures of pHBECs in a realistic microenvironment mimicking the human native bronchial epithelium at ALI. For this goal, co-culture models with human hematopoietic cells and fibroblasts should be taken into consideration. Moreover, human organoids or lung-on-a-chip models represent further tools that could improve culture and treatment conditions.

b) Highly standardized cell exposure systems with more than 12 transwells slots could offer a simultaneous exposure for many culture conditions at the same time. This improvement is important to reduce the results heterogeneity.

c) Novel, elastic porous membranes should replace the silicone-based membranes previously used on conventional ALI culture models. These changes could improve the cultivation of primary cells, the passage of transcellular pollutants, as well as the analysis of drug kinetics from the basolateral side of the cells into the basal media.

d) The use of highly standardized cell exposure systems for the delivery of aerosolized drugs to analyze the pharmacokinetics and deposition efficiency of novel drugs that have not been previously tested in an aerosolized/ nebulized form. Thus, the drug nebulization route might help better understand the functional post-exposure changes at the level of the bronchial epithelium.

e) The above-mentioned aspects (a-d) applied for *in vitro* models should be also investigated *ex vivo*, by using native human BPs cultured at ALI on optimized porous membranes.

All these improvements could facilitate more realistic culture models with nearly physiological toxin exposure and drug delivery conditions for toxicological studies that can inform further preventive and therapeutic strategies in COPD.

6. References

1 Ruiz García S, Deprez M, Lebrigand K, et al. Novel dynamics of human mucociliary differentiation revealed by single-cell RNA sequencing of nasal epithelial cultures. *Development*. 2019;146(20). doi:10.1242/dev.177428.

2 Deprez M, Zaragosi L-E, Truchi M, et al. A Single-Cell Atlas of the Human Healthy Airways. *Am J Respir Crit Care Med*. 2020;202(12):1636-1645. doi:10.1164/rccm.201911-2199OC.

3 Smith CM, Djakow J, Free RC, et al. ciliaFA: a research tool for automated, high-throughput measurement of ciliary beat frequency using freely available software. *Cilia*. 2012;1:14. doi:10.1186/2046-2530-1-14.

4 Srinivasan B, Kolli AR, Esch MB, Abaci HE, Shuler ML, Hickman JJ. TEER measurement techniques for in vitro barrier model systems. *J Lab Autom*. 2015;20(2):107-126. doi:10.1177/2211068214561025.

5 Angelidis I, Simon LM, Fernandez IE, et al. An atlas of the aging lung mapped by single cell transcriptomics and deep tissue proteomics. *Nat Commun*. 2019;10(1):963. doi:10.1038/s41467-019-08831-9.

6 Paolicelli G, Luca A de, Jose SS, et al. Using Lung Organoids to Investigate Epithelial Barrier Complexity and IL-17 Signaling During Respiratory Infection. *Front Immunol*. 2019;10:323. doi:10.3389/fimmu.2019.00323.

7 Ambroz F, Macdonald TJ, Martis V, Parkin IP. Evaluation of the BET Theory for the Characterization of Meso and Microporous MOFs. *Small Methods*. 2018;2(11):1800173. doi:10.1002/smtd.201800173.

8 Haider M, Shafqat MN, Zafar M. Impact of air pollution on severe acute exacerbation of COPD. *Int J Chron Obstruct Pulmon Dis*. 2018;13:2101-2103. doi:10.2147/COPD.S170691.

9 Marino E, Caruso M, Campagna D, Polosa R. Impact of air quality on lung health: myth or reality? *Ther Adv Chronic Dis*. 2015;6(5):286-298. doi:10.1177/2040622315587256.

10 Hamanaka RB, Mutlu GM. Particulate Matter Air Pollution: Effects on the Cardiovascular System. *Front Endocrinol (Lausanne)*. 2018;9. doi:10.3389/fendo.2018.00680.

11 Thurston GD, Kipen H, Annesi-Maesano I, et al. A joint ERS/ATS policy statement: what constitutes an adverse health effect of air pollution? An analytical framework. *Eur Respir J*. 2017;49(1). doi:10.1183/13993003.00419-2016.

12 Xu X, Ha SU, Basnet R. A Review of Epidemiological Research on Adverse Neurological Effects of Exposure to Ambient Air Pollution. *Front Public Health*. 2016;4. doi:10.3389/fpubh.2016.00157.

13 Khan A, Plana-Ripoll O, Antonsen S, et al. Environmental pollution is associated with increased risk of psychiatric disorders in the US and Denmark. *PLoS Biol*. 2019;17(8). doi:10.1371/journal.pbio.3000353.

14 Orru H, Ebi KL, Forsberg B. The Interplay of Climate Change and Air Pollution on Health. *Curr Environ Health Rep*. 2017;4(4):504-513. doi:10.1007/s40572-017-0168-6.

15 Schraufnagel DE, Balmes JR, Cowl CT, et al. Air Pollution and Noncommunicable Diseases: A Review by the Forum of International Respiratory Societies' Environmental Committee, Part 2: Air Pollution and Organ Systems. *Chest*. 2019;155(2):417-426. doi:10.1016/j.chest.2018.10.041.

16 Fazzo L, Carere M, Tisano F, et al. Cancer incidence in Priolo, Sicily: a spatial approach for estimation of industrial air pollution impact. *Geospat Health*. 2016;11(1):320. doi:10.4081/gh.2016.320.

17 Khomenko S, Cirach M, Pereira-Barboza E, et al. Premature mortality due to air pollution in European cities: a health impact assessment. *The Lancet Planetary Health*. 2021;5(3):e121-e134. doi:10.1016/S2542-5196(20)30272-2.

18   Johannson KA, Balmes JR, Collard HR. Air pollution exposure: a novel environmental risk factor for interstitial lung disease? *Chest*. 2015;147(4):1161-1167. doi:10.1378/chest.14-1299.

19   Andersen ZJ, Bønnelykke K, Hvidberg M, et al. Long-term exposure to air pollution and asthma hospitalisations in older adults: a cohort study. *Thorax*. 2012;67(1):6-11. doi:10.1136/thoraxjnl-2011-200711.

20   Shimizu K, Yoshii Y, Morozumi M, et al. Pathogens in COPD exacerbations identified by comprehensive real-time PCR plus older methods. *Int J Chron Obstruct Pulmon Dis*. 2015;10:2009-2016. doi:10.2147/COPD.S82752.

21   Hiller A-M, Piitulainen E, Jehpsson L, Tanash H. Decline in FEV1 and hospitalized exacerbations in individuals with severe alpha-1 antitrypsin deficiency. *Int J Chron Obstruct Pulmon Dis*. 2019;14:1075-1083. doi:10.2147/COPD.S195847.

22   Vestbo J, Edwards LD, Scanlon PD, et al. Changes in forced expiratory volume in 1 second over time in COPD. *N Engl J Med*. 2011;365(13):1184-1192. doi:10.1056/NEJMoa1105482.

23   Hamra GB, Guha N, Cohen A, et al. Outdoor particulate matter exposure and lung cancer: a systematic review and meta-analysis. *Environ Health Perspect*. 2014;122(9):906-911. doi:10.1289/ehp/1408092.

24   Chirino YI, Sánchez-Pérez Y, Osornio-Vargas ÁR, Rosas I, García-Cuellar CM. Sampling and composition of airborne particulate matter (PM10) from two locations of Mexico City. *Data Brief*. 2015;4:353-356. doi:10.1016/j.dib.2015.06.017.

25   van den Heuvel R, Den Hond E, Govarts E, et al. Identification of PM10 characteristics involved in cellular responses in human bronchial epithelial cells (Beas-2B). *Environ Res*. 2016;149:48-56. doi:10.1016/j.envres.2016.04.029.

26   Hawley B, Schaeffer J, Poole JA, Dooley GP, Reynolds S, Volckens J. Differential response of human nasal and bronchial epithelial cells upon exposure to size-fractionated dairy dust. *J Toxicol Environ Health Part A*. 2015;78(9):583-594. doi:10.1080/15287394.2015.1015699.

27   Loxham M, Morgan-Walsh RJ, Cooper MJ, et al. The Effects on Bronchial Epithelial Mucociliary Cultures of Coarse, Fine, and Ultrafine Particulate Matter From an Underground Railway Station. *Toxicol Sci*. 2015;145(1):98-107. doi:10.1093/toxsci/kfv034.

28   Cho C-C, Hsieh W-Y, Tsai C-H, Chen C-Y, Chang H-F, Lin C-S. In Vitro and In Vivo Experimental Studies of PM2.5 on Disease Progression. *Int J Environ Res Public Health*. 2018;15(7). doi:10.3390/ijerph15071380.

29   Li Y, Wang P, Hu C, et al. Protein corona of airborne nanoscale PM2.5 induces aberrant proliferation of human lung fibroblasts based on a 3D organotypic culture. *Sci Rep*. 2018;8(1):1939. doi:10.1038/s41598-018-20445-7.

30   Mühlfeld C, Rothen-Rutishauser B, Blank F, Vanhecke D, Ochs M, Gehr P. Interactions of nanoparticles with pulmonary structures and cellular responses. *Am J Physiol Lung Cell Mol Physiol*. 2008;294(5):L817-29. doi:10.1152/ajplung.00442.2007.

31   Jachak A, Lai SK, Hida K, et al. Transport of metal oxide nanoparticles and single-walled carbon nanotubes in human mucus. *Nanotoxicology*. 2012;6(6):614-622. doi:10.3109/17435390.2011.598244.

32   Loxham M, Davies DE, Blume C. Epithelial function and dysfunction in asthma. *Clin Exp Allergy*. 2014;44(11):1299-1313. doi:10.1111/cea.12309.

33   Lelieveld J, Pozzer A, Pöschl U, Fnais M, Haines A, Münzel T. Loss of life expectancy from air pollution compared to other risk factors: a worldwide perspective. *Cardiovasc Res*. 2020;116(11):1910-1917. doi:10.1093/cvr/cvaa025.

34   Garshick E. Effects of short- and long-term exposures to ambient air pollution on COPD. *Eur Respir J*. 2014;44(3):558-561. doi:10.1183/09031936.00108814.

35   Lagorio S, Forastiere F, Pistelli R, et al. Air pollution and lung function among susceptible adult subjects: a panel study. *Environ Health*. 2006;5:11. doi:10.1186/1476-069X-5-11.

36   Yue W, Tong L, Liu X, et al. Short term Pm2.5 exposure caused a robust lung inflammation, vascular remodeling, and exacerbated transition from left ventricular failure to right ventricular hypertrophy. *Redox Biol*. 2019;22:101161. doi:10.1016/j.redox.2019.101161.

37   Shah ASV, Lee KK, McAllister DA, et al. Short term exposure to air pollution and stroke: systematic review and meta-analysis. *BMJ*. 2015;350:h1295. doi:10.1136/bmj.h1295.

38   Chan SMH, Selemidis S, Bozinovski S, Vlahos R. Pathobiological mechanisms underlying metabolic syndrome (MetS) in chronic obstructive pulmonary disease (COPD): clinical significance and thera-peutic strategies. *Pharmacol Ther*. 2019;198:160-188. doi:10.1016/j.pharmthera.2019.02.013.

39   Divo M, Celli BR. Multimorbidity in Patients with Chronic Obstructive Pulmonary Disease. *Clin Chest Med*. 2020;41(3):405-419. doi:10.1016/j.ccm.2020.06.002.

40   Gu J, Shi Y, Zhu Y, et al. Ambient air pollution and cause-specific risk of hospital admission in China: A nationwide time-series study. *PLoS Med*. 2020;17(8):e1003188. doi:10.1371/jour-nal.pmed.1003188.

41   Bi J, Barry V, Weil EJ, Chang HH, Ebelt S. Short-term exposure to fine particulate air pollution and emergency department visits for kidney diseases in the Atlanta metropolitan area. *Environ Epidemiol*. 2021;5(4):e164. doi:10.1097/EE9.0000000000000164.

42   Zeft AS, Prahalad S, Schneider R, et al. Systemic onset juvenile idiopathic arthritis and exposure to fine particulate air pollution. *Clin Exp Rheumatol*. 2016;34(5):946-952. Published September 1, 2016.

43   Fongsodsri K, Chamnanchanunt S, Desakorn V, et al. Particulate Matter 2.5 and Hematological Dis-orders From Dust to Diseases: A Systematic Review of Available Evidence. *Front Med (Lausanne)*. 2021;8:692008. doi:10.3389/fmed.2021.692008.

44   Duan R-R, Hao K, Yang T. Air pollution and chronic obstructive pulmonary disease. *Chronic Dis Transl Med*. 2020;6(4):260-269. doi:10.1016/j.cdtm.2020.05.004.

45   Jiang X-Q, Mei X-D, Di Feng. Air pollution and chronic airway diseases: what should people know and do? *J Thorac Dis*. 2016;8(1):E31-40. doi:10.3978/j.issn.2072-1439.2015.11.50.

46   López-Campos JL, Tan W, Soriano JB. Global burden of COPD. *Respirology*. 2016;21(1):14-23. doi:10.1111/resp.12660.

47   Ko FW, Chan KP, Hui DS, et al. Acute exacerbation of COPD. *Respirology*. 2016;21(7):1152-1165. doi:10.1111/resp.12780.

48   Lorenz J, Bals R, Dreher M, et al. Expertentreffen COPD: Exazerbation der COPD. *Pneumologie*. 2017;71(5):269-289. doi:10.1055/s-0043-106559.

49   Thabut G, Mal H. Outcomes after lung transplantation. *J Thorac Dis*. 2017;9(8):2684-2691. doi:10.21037/jtd.2017.07.85.

50   Buist AS, McBurnie MA, Vollmer WM, et al. International variation in the prevalence of COPD (the BOLD Study): a population-based prevalence study. *Lancet*. 2007;370(9589):741-750. doi:10.1016/S0140-6736(07)61377-4.

51   Li J, Sun S, Tang R, et al. Major air pollutants and risk of COPD exacerbations: a systematic review and meta-analysis. *Int J Chron Obstruct Pulmon Dis*. 2016;11:3079-3091. doi:10.2147/COPD.S122282.

52   Marçôa R, Rodrigues DM, Dias M, et al. Classification of Chronic Obstructive Pulmonary Disease (COPD) according to the new Global Initiative for Chronic Obstructive Lung Disease (GOLD) 2017: Comparison with GOLD 2011. *COPD*. 2018;15(1):21-26. doi:10.1080/15412555.2017.1394285.

53   Mirza S, Clay RD, Koslow MA, Scanlon PD. COPD Guidelines: A Review of the 2018 GOLD Report. *Mayo Clin Proc*. 2018;93(10):1488-1502. doi:10.1016/j.mayocp.2018.05.026.

54   Singh D. Pharmacological treatment for COPD; GOLD 2017 changes direction. *Br J Clin Pharmacol*. 2017;83(5):935-937. doi:10.1111/bcp.13212.

55   Lopez-Campos JL, Marquez-Martin E, Soriano JB. The role of air pollution in COPD and implications for therapy. *Expert Rev Respir Med*. 2016;10(8):849-859. doi:10.1080/17476348.2016.1191356.

56   Bai J-W, Chen X-X, Liu S, Yu L, Xu J-F. Smoking cessation affects the natural history of COPD. *Int J Chron Obstruct Pulmon Dis*. 2017;12:3323-3328. doi:10.2147/COPD.S150243.

57   Tønnesen P. Smoking cessation and COPD. *Eur Respir Rev*. 2013;22(127):37-43. doi:10.1183/09059180.00007212.

58   Dolovich MB, Ahrens RC, Hess DR, et al. Device selection and outcomes of aerosol therapy: Evidence-based guidelines: American College of Chest Physicians/American College of Asthma, Allergy, and Immunology. *Chest*. 2005;127(1):335-371. doi:10.1378/chest.127.1.335.

59   Rau JL. The inhalation of drugs: advantages and problems. *Respir Care*. 2005;50(3):367-382.

60   Yang L, Gradl R, Dierolf M, et al. Multimodal Precision Imaging of Pulmonary Nanoparticle Delivery in Mice: Dynamics of Application, Spatial Distribution, and Dosimetry. *Small*. 2019;15(49):e1904112. doi:10.1002/smll.201904112.

61   Hikichi M, Mizumura K, Maruoka S, Gon Y. Pathogenesis of chronic obstructive pulmonary disease (COPD) induced by cigarette smoke. *J Thorac Dis*. 2019;11(Suppl 17):S2129-S2140. doi:10.21037/jtd.2019.10.43.

62   MacNee W. Pathogenesis of chronic obstructive pulmonary disease. *Proc Am Thorac Soc*. 2005;2(4):258-66; discussion 290-1. doi:10.1513/pats.200504-045SR.

63   Agustí A, Hogg JC. Update on the Pathogenesis of COPD. Reply. *N Engl J Med*. 2019;381(25):2484. doi:10.1056/NEJMc1914437.

64   Morales-Hernández A, Nacarino-Palma A, Moreno-Marín N, et al. Lung regeneration after toxic injury is improved in absence of dioxin receptor. *Stem Cell Res*. 2017;25:61-71. doi:10.1016/j.scr.2017.10.009.

65   Mette SA, Pilewski J, Buck CA, Albelda SM. Distribution of integrin cell adhesion receptors on normal bronchial epithelial cells and lung cancer cells in vitro and in vivo. *Am J Respir Cell Mol Biol*. 1993;8(5):562-572. doi:10.1165/ajrcmb/8.5.562.

66   Gao W, Li L, Wang Y, et al. Bronchial epithelial cells: The key effector cells in the pathogenesis of chronic obstructive pulmonary disease? *Respirology*. 2015;20(5):722-729. doi:10.1111/resp.12542.

67   Kozu Y, Gon Y, Maruoka S, et al. Protocadherin-1 is a glucocorticoid-responsive critical regulator of airway epithelial barrier function. *BMC Pulm Med*. 2015;15:80. doi:10.1186/s12890-015-0078-z.

68   Kubo T, Wawrzyniak P, Morita H, et al. CpG-DNA enhances the tight junction integrity of the bronchial epithelial cell barrier. *J Allergy Clin Immunol*. 2015;136(5):1413-6.e1-8. doi:10.1016/j.jaci.2015.05.006.

69   Su Y, Yao H, Wang H, et al. IL-27 enhances innate immunity of human pulmonary fibroblasts and epithelial cells through upregulation of TLR4 expression. *Am J Physiol Lung Cell Mol Physiol*. 2016;310(2):L133-41. doi:10.1152/ajplung.00307.2015.

70   Rock JR, Randell SH, Hogan BLM. Airway basal stem cells: a perspective on their roles in epithelial homeostasis and remodeling. *Dis Model Mech*. 2010;3(9-10):545-556. doi:10.1242/dmm.006031.

71   Ghosh M, Miller YE, Nakachi I, et al. Exhaustion of Airway Basal Progenitor Cells in Early and Established Chronic Obstructive Pulmonary Disease. *Am J Respir Crit Care Med*. 2018;197(7):885-896. doi:10.1164/rccm.201704-0667OC.

72   Tadokoro T, Wang Y, Barak LS, Bai Y, Randell SH, Hogan BLM. IL-6/STAT3 promotes regeneration of airway ciliated cells from basal stem cells. *Proc Natl Acad Sci U S A*. 2014;111(35):E3641-9. doi:10.1073/pnas.1409781111.

73   Haddad A, Gaudet M, Plesa M, et al. Neutrophils from severe asthmatic patients induce epithelial to mesenchymal transition in healthy bronchial epithelial cells. *Respir Res*. 2019;20(1):234. doi:10.1186/s12931-019-1186-8.

74   Xu Q, Fang L, Chen B, et al. Radon induced mitochondrial dysfunction in human bronchial epithelial cells and epithelial-mesenchymal transition with long-term exposure. *Toxicol Res (Camb)*. 2019;8(1):90-100. doi:10.1039/c8tx00181b.

75   Pratheeshkumar P, Son Y-O, Divya SP, Wang L, Zhang Z, Shi X. Oncogenic transformation of human lung bronchial epithelial cells induced by arsenic involves ROS-dependent activation of STAT3-miR-21-PDCD4 mechanism. *Sci Rep*. 2016;6:37227. doi:10.1038/srep37227.

76   Vaz M, Hwang SY, Kagiampakis I, et al. Chronic Cigarette Smoke-Induced Epigenomic Changes Precede Sensitization of Bronchial Epithelial Cells to Single-Step Transformation by KRAS Mutations. *Cancer Cell*. 2017;32(3):360-376.e6. doi:10.1016/j.ccell.2017.08.006.

77   Boers JE, Ambergen AW, Thunnissen FB. Number and proliferation of basal and parabasal cells in normal human airway epithelium. *Am J Respir Crit Care Med*. 1998;157(6 Pt 1):2000-2006. doi:10.1164/ajrccm.157.6.9707011.

78   Tilley AE, Walters MS, Shaykhiev R, Crystal RG. Cilia dysfunction in lung disease. *Annu Rev Physiol*. 2015;77:379-406. doi:10.1146/annurev-physiol-021014-071931.

79   Raman T, O'Connor TP, Hackett NR, et al. Quality control in microarray assessment of gene expression in human airway epithelium. *BMC Genomics*. 2009;10:493. doi:10.1186/1471-2164-10-493.

80   Yager J, Chen TM, Dulfano MJ. Measurement of frequency of ciliary beats of human respiratory epithelium. *Chest*. 1978;73(5):627-633. doi:10.1378/chest.73.5.627.

81   Jing JC, Chen JJ, Chou L, Wong BJF, Chen Z. Visualization and Detection of Ciliary Beating Pattern and Frequency in the Upper Airway using Phase Resolved Doppler Optical Coherence Tomography. *Sci Rep*. 2017;7(1):8522. doi:10.1038/s41598-017-08968-x.

82   Jackson PK, Attardi LD. p73 and FoxJ1: Programming Multiciliated Epithelia. *Trends Cell Biol*. 2016;26(4):239-240. doi:10.1016/j.tcb.2016.03.001.

83   Mukherjee I, Roy S, Chakrabarti S. Identification of Important Effector Proteins in the FOXJ1 Transcriptional Network Associated With Ciliogenesis and Ciliary Function. *Front Genet*. 2019;10:23. doi:10.3389/fgene.2019.00023.

84   Seeley ES, Nachury MV. The perennial organelle: assembly and disassembly of the primary cilium. *J Cell Sci*. 2010;123(Pt 4):511-518. doi:10.1242/jcs.061093.

85   Goto H, Inaba H, Inagaki M. Mechanisms of ciliogenesis suppression in dividing cells. *Cell Mol Life Sci*. 2017;74(5):881-890. doi:10.1007/s00018-016-2369-9.

86   Bustamante-Marin XM, Ostrowski LE. Cilia and Mucociliary Clearance. *Cold Spring Harb Perspect Biol*. 2017;9(4). doi:10.1101/cshperspect.a028241.

87   Whitsett JA. Airway Epithelial Differentiation and Mucociliary Clearance. *Ann Am Thorac Soc*. 2018;15(Suppl 3):S143-S148. doi:10.1513/AnnalsATS.201802-128AW.

88   Schmid A, Sailland J, Novak L, Baumlin N, Fregien N, Salathe M. Modulation of Wnt signaling is essential for the differentiation of ciliated epithelial cells in human airways. *FEBS Lett*. 2017;591(21):3493-3506. doi:10.1002/1873-3468.12851.

89   Rawlins EL, Ostrowski LE, Randell SH, Hogan BLM. Lung development and repair: contribution of the ciliated lineage. *Proc Natl Acad Sci U S A*. 2007;104(2):410-417. doi:10.1073/pnas.0610770104.

90   Park K-S, Wells JM, Zorn AM, et al. Transdifferentiation of ciliated cells during repair of the respiratory epithelium. *Am J Respir Cell Mol Biol*. 2006;34(2):151-157. doi:10.1165/rcmb.2005-0332OC.

91   Wu C-J, Chen L-C, Huang W-C, Chuang C-L, Kuo M-L. Alleviation of lung inflammatory responses by adeno-associated virus 2/9 vector carrying CC10 in OVA-sensitized mice. *Hum Gene Ther*. 2013;24(1):48-57. doi:10.1089/hum.2012.039.

92   Long X-B, Hu S, Wang N, Zhen H-T, Cui Y-H, Liu Z. Clara cell 10-kDa protein gene transfection inhibits NF-κB activity in airway epithelial cells. *PLoS ONE*. 2012;7(4):e35960. doi:10.1371/journal.pone.0035960.

93   Shijubo N, Honda Y, Itoh Y, et al. BAL surfactant protein A and Clara cell 10-kDa protein levels in healthy subjects. *Lung*. 1998;176(4):257-265. doi:10.1007/pl00007608.

94   Singh G, Katyal SL. Clara cells and Clara cell 10 kD protein (CC10). *Am J Respir Cell Mol Biol*. 1997;17(2):141-143. doi:10.1165/ajrcmb.17.2.f138.

95   Cui Y-H, Wang Y-Y, Liu Z. Transdifferentiation of Clara cell 10-kDa protein secreting cells in experimental allergic rhinitis. *Am J Rhinol Allergy*. 2011;25(3):145-151. doi:10.2500/ajra.2011.25.3596.

96   Szabo E, Goheer A, Witschi H, Linnoila RI. Overexpression of CC10 modifies neoplastic potential in lung cancer cells. *Cell Growth Differ*. 1998;9(6):475-485.

97   Rogers DF. Airway goblet cells: responsive and adaptable front-line defenders. *Eur Respir J*. 1994;7(9):1690-1706.

98   Knoop KA, Newberry RD. Goblet cells: multifaceted players in immunity at mucosal surfaces. *Mucosal Immunol*. 2018;11(6):1551-1557. doi:10.1038/s41385-018-0039-y.

99   Ma J, Rubin BK, Voynow JA. Mucins, Mucus, and Goblet Cells. *Chest*. 2018;154(1):169-176. doi:10.1016/j.chest.2017.11.008.

100   Tanabe T, Rubin BK. Airway Goblet Cells Secrete Pro-Inflammatory Cytokines, Chemokines, and Growth Factors. *Chest*. 2016;149(3):714-720. doi:10.1378/chest.15-0947.

101   Plasschaert LW, Žilionis R, Choo-Wing R, et al. A single-cell atlas of the airway epithelium reveals the CFTR-rich pulmonary ionocyte. *Nature*. 2018;560(7718):377-381. doi:10.1038/s41586-018-0394-6.

102   Li X, Zheng M, Pu J, et al. Identification of abnormally expressed lncRNAs induced by PM2.5 in human bronchial epithelial cells. *Biosci Rep*. 2018;38(5). doi:10.1042/BSR20171577.

103   Keenan CR, Mok JS, Harris T, Xia Y, Salem S, Stewart AG. Bronchial epithelial cells are rendered insensitive to glucocorticoid transactivation by transforming growth factor-β1. *Respir Res*. 2014;15:55. doi:10.1186/1465-9921-15-55.

104   Sasaki M, Kishimoto M, Itakura Y, et al. Air-liquid interphase culture confers SARS-CoV-2 susceptibility to A549 alveolar epithelial cells. *Biochem Biophys Res Commun*. 2021;577:146-151. doi:10.1016/j.bbrc.2021.09.015.

105   Xu X, Wang H, Liu S, et al. TP53-dependent autophagy links the ATR-CHEK1 axis activation to proinflammatory VEGFA production in human bronchial epithelial cells exposed to fine particulate matter (PM2.5). *Autophagy*. 2016;12(10):1832-1848. doi:10.1080/15548627.2016.1204496.

106 Zhu X-M, Wang Q, Xing W-W, et al. PM2.5 induces autophagy-mediated cell death via NOS2 signaling in human bronchial epithelium cells. *Int J Biol Sci*. 2018;14(5):557-564. doi:10.7150/ijbs.24546.

107 Schamberger AC, Staab-Weijnitz CA, Mise-Racek N, Eickelberg O. Cigarette smoke alters primary human bronchial epithelial cell differentiation at the air-liquid interface. *Sci Rep*. 2015;5:8163. doi:10.1038/srep08163.

108 He R-W, Braakhuis HM, Vandebriel RJ, et al. Optimization of an air-liquid interface in vitro cell co-culture model to estimate the hazard of aerosol exposures. *Journal of Aerosol Science*. 2021;153:105703. doi:10.1016/j.jaerosci.2020.105703.

109 Pinkston R, Zaman H, Hossain E, Penn AL, Noël A. Cell-specific toxicity of short-term JUUL aerosol exposure to human bronchial epithelial cells and murine macrophages exposed at the air-liquid interface. *Respir Res*. 2020;21(1):269. doi:10.1186/s12931-020-01539-1.

110 Walters MS, Gomi K, Ashbridge B, et al. Generation of a human airway epithelium derived basal cell line with multipotent differentiation capacity. *Respir Res*. 2013;14:135. doi:10.1186/1465-9921-14-135.

111 Lenz A-G, Stoeger T, Cei D, et al. Efficient bioactive delivery of aerosolized drugs to human pulmonary epithelial cells cultured in air-liquid interface conditions. *Am J Respir Cell Mol Biol*. 2014;51(4):526-535. doi:10.1165/rcmb.2013-0479OC.

112 Schamberger AC, Mise N, Jia J, et al. Cigarette smoke-induced disruption of bronchial epithelial tight junctions is prevented by transforming growth factor-β. *Am J Respir Cell Mol Biol*. 2014;50(6):1040-1052. doi:10.1165/rcmb.2013-0090OC.

113 Macosko EZ, Basu A, Satija R, et al. Highly Parallel Genome-wide Expression Profiling of Individual Cells Using Nanoliter Droplets. *Cell*. 2015;161(5):1202-1214. doi:10.1016/j.cell.2015.05.002.

114 Ziegenhain C, Vieth B, Parekh S, et al. Comparative Analysis of Single-Cell RNA Sequencing Methods. *Mol Cell*. 2017;65(4):631-643.e4. doi:10.1016/j.molcel.2017.01.023.

115 Wiśniewski JR, Zougman A, Nagaraj N, Mann M. Universal sample preparation method for proteome analysis. *Nat Methods*. 2009;6(5):359-362. doi:10.1038/nmeth.1322.

116 Grosche A, Reichenbach A. Neuroscience. Developmental refining of neuroglial signaling? *Science*. 2013;339(6116):152-153. doi:10.1126/science.1233208.

117 Käll L, Canterbury JD, Weston J, Noble WS, MacCoss MJ. Semi-supervised learning for peptide identification from shotgun proteomics datasets. *Nat Methods*. 2007;4(11):923-925. doi:10.1038/nmeth1113.

118 Rainer J, Sanchez-Cabo F, Stocker G, Sturn A, Trajanoski Z. CARMAweb: comprehensive R- and bioconductor-based web service for microarray data analysis. *Nucleic Acids Res*. 2006;34(Web Server issue):W498-503. doi:10.1093/nar/gkl038.

119 Navarro P, Trevisan-Herraz M, Bonzon-Kulichenko E, et al. General statistical framework for quantitative proteomics by stable isotope labeling. *J Proteome Res*. 2014;13(3):1234-1247. doi:10.1021/pr4006958.

120 Lindahl M, Leanderson P, Tagesson C. Novel aspect on metal fume fever: zinc stimulates oxygen radical formation in human neutrophils. *Hum Exp Toxicol*. 1998;17(2):105-110. doi:10.1177/096032719801700205.

121 Wu Z, Shi P, Lim HK, et al. Inflammation Increases Susceptibility of Human Small Airway Epithelial Cells to Pneumonic Nanotoxicity. *Small*. 2020;16(21):e2000963. doi:10.1002/smll.202000963.

122 Brand P, Lenz K, Reisgen U, Kraus T. Number size distribution of fine and ultrafine fume particles from various welding processes. *Ann Occup Hyg*. 2013;57(3):305-313. doi:10.1093/annhyg/mes070.

123 Donaldson K, Tran L, Jimenez LA, et al. Combustion-derived nanoparticles: a review of their toxicology following inhalation exposure. *Part Fibre Toxicol*. 2005;2:10. doi:10.1186/1743-8977-2-10.

124 Pezzulo AA, Starner TD, Scheetz TE, et al. The air-liquid interface and use of primary cell cultures are important to recapitulate the transcriptional profile of in vivo airway epithelia. *Am J Physiol Lung Cell Mol Physiol*. 2011;300(1):L25-31. doi:10.1152/ajplung.00256.2010.

125 Rayner RE, Makena P, Prasad GL, Cormet-Boyaka E. Optimization of Normal Human Bronchial Epithelial (NHBE) Cell 3D Cultures for in vitro Lung Model Studies. *Sci Rep*. 2019;9(1):500. doi:10.1038/s41598-018-36735-z.

126 Chow C-M, Georgiou A, Szutorisz H, et al. Variant histone H3.3 marks promoters of transcriptionally active genes during mammalian cell division. *EMBO Rep*. 2005;6(4):354-360. doi:10.1038/sj.embor.7400366.

127 Tsao P-N, Vasconcelos M, Izvolsky KI, Qian J, Lu J, Cardoso WV. Notch signaling controls the balance of ciliated and secretory cell fates in developing airways. *Development*. 2009;136(13):2297-2307. doi:10.1242/dev.034884.

128 Liu Y, Zhou T, Sun L, Wang H, Zhou L. The effect of Notch signal pathway on PM2.5-induced Muc5ac in Beas-2B cells. *Ecotoxicol Environ Saf*. 2020;203:110956. doi:10.1016/j.ecoenv.2020.110956.

129 Carlier FM, Dupasquier S, Ambroise J, et al. Canonical WNT pathway is activated in the airway epithelium in chronic obstructive pulmonary disease. *EBioMedicine*. 2020;61:103034. doi:10.1016/j.ebiom.2020.103034.

130 Kneidinger N, Yildirim AÖ, Callegari J, et al. Activation of the WNT/β-catenin pathway attenuates experimental emphysema. *Am J Respir Crit Care Med*. 2011;183(6):723-733. doi:10.1164/rccm.200910-1560OC.

131 Meng J, Yang J, Pan T, Qu X, Cui S. ZnO nanoparticles promote the malignant transformation of colorectal epithelial cells in APCmin/+ mice. *Environ Int*. 2022;158:106923. doi:10.1016/j.envint.2021.106923.

132 Pan C-H, Liu W-T, Bien M-Y, et al. Effects of size and surface of zinc oxide and aluminum-doped zinc oxide nanoparticles on cell viability inferred by proteomic analyses. *Int J Nanomedicine*. 2014;9:3631-3643. doi:10.2147/IJN.S66651.

133 Schikowski T, Mills IC, Anderson HR, et al. Ambient air pollution: a cause of COPD? *Eur Respir J*. 2014;43(1):250-263. doi:10.1183/09031936.00100112.

134 Tung NT, Ho S-C, Lu Y-H, et al. Association Between Air Pollution and Lung Lobar Emphysema in COPD. *Front Med (Lausanne)*. 2021;8:705792. doi:10.3389/fmed.2021.705792.

135 Stewart CE, Torr EE, Mohd Jamili NH, Bosquillon C, Sayers I. Evaluation of differentiated human bronchial epithelial cell culture systems for asthma research. *J Allergy (Cairo)*. 2012;2012:943982. doi:10.1155/2012/943982.

136 Wawrzyniak P, Krawczyk K, Acharya S, et al. Inhibition of CpG methylation improves the barrier integrity of bronchial epithelial cells in asthma. *Allergy*. 2021;76(6):1864-1868. doi:10.1111/all.14667.

137 Hewson CK, Capraro A, Wong SL, et al. Novel Antioxidant Therapy with the Immediate Precursor to Glutathione, γ-Glutamylcysteine (GGC), Ameliorates LPS-Induced Cellular Stress in In Vitro 3D-Differentiated Airway Model from Primary Cystic Fibrosis Human Bronchial Cells. *Antioxidants (Basel)*. 2020;9(12). doi:10.3390/antiox9121204.

138 Perra L, Balloy V, Foussignière T, et al. CHAC1 Is Differentially Expressed in Normal and Cystic Fibrosis Bronchial Epithelial Cells and Regulates the Inflammatory Response Induced by Pseudomonas aeruginosa. *Front Immunol*. 2018;9:2823. doi:10.3389/fimmu.2018.02823.

139 Phillips J, Kluss B, Richter A, Massey E. Exposure of bronchial epithelial cells to whole cigarette smoke: assessment of cellular responses. *Altern Lab Anim*. 2005;33(3):239-248. doi:10.1177/026119290503300310.

140 Mastalerz M, Dick E, Chakraborty A, et al. Validation of in vitro models for smoke exposure of primary human bronchial epithelial cells. *Am J Physiol Lung Cell Mol Physiol*. 2022;322(1):L129-L148. doi:10.1152/ajplung.00091.2021.

141 Leibrock L, Wagener S, Singh AV, Laux P, Luch A. Nanoparticle induced barrier function assessment at liquid-liquid and air-liquid interface in novel human lung epithelia cell lines. *Toxicol Res (Camb)*. 2019;8(6):1016-1027. doi:10.1039/c9tx00179d.

142 Diabaté S, Armand L, Murugadoss S, et al. Air-Liquid Interface Exposure of Lung Epithelial Cells to Low Doses of Nanoparticles to Assess Pulmonary Adverse Effects. *Nanomaterials (Basel)*. 2020;11(1). doi:10.3390/nano11010065.

143 Lenz AG, Karg E, Lentner B, et al. A dose-controlled system for air-liquid interface cell exposure and application to zinc oxide nanoparticles. *Part Fibre Toxicol*. 2009;6:32. doi:10.1186/1743-8977-6-32.

144 Ding Y, Weindl P, Lenz A-G, Mayer P, Krebs T, Schmid O. Quartz crystal microbalances (QCM) are suitable for real-time dosimetry in nanotoxicological studies using VITROCELL®Cloud cell exposure systems. *Part Fibre Toxicol*. 2020;17(1):44. doi:10.1186/s12989-020-00376-w.

145 Hu Y, Lou J, Mao Y-Y, et al. Activation of MTOR in pulmonary epithelium promotes LPS-induced acute lung injury. *Autophagy*. 2016;12(12):2286-2299. doi:10.1080/15548627.2016.1230584.

146 Chen Y, Guo S, Jiang K, Wang Y, Yang M, Guo M. Glycitin alleviates lipopolysaccharide-induced acute lung injury via inhibiting NF-κB and MAPKs pathway activation in mice. *Int Immunopharmacol*. 2019;75:105749. doi:10.1016/j.intimp.2019.105749.

147 Berger M, Boer JD de, Lutter R, et al. Pulmonary challenge with carbon nanoparticles induces a dose-dependent increase in circulating leukocytes in healthy males. *BMC Pulm Med*. 2017;17(1):121. doi:10.1186/s12890-017-0463-x.

148 Xia T, Kovochich M, Liong M, et al. Comparison of the mechanism of toxicity of zinc oxide and cerium oxide nanoparticles based on dissolution and oxidative stress properties. *ACS Nano*. 2008;2(10):2121-2134. doi:10.1021/nn800511k.

149 Wilhelmi V, Fischer U, Weighardt H, et al. Zinc oxide nanoparticles induce necrosis and apoptosis in macrophages in a p47phox- and Nrf2-independent manner. *PLoS ONE*. 2013;8(6):e65704. doi:10.1371/journal.pone.0065704.

150 Zhang J, Qin X, Wang B, et al. Zinc oxide nanoparticles harness autophagy to induce cell death in lung epithelial cells. *Cell Death Dis*. 2017;8(7):e2954. doi:10.1038/cddis.2017.337.

151 Ekstrand-Hammarström B, Akfur CM, Andersson PO, Lejon C, Osterlund L, Bucht A. Human primary bronchial epithelial cells respond differently to titanium dioxide nanoparticles than the lung epithelial cell lines A549 and BEAS-2B. *Nanotoxicology*. 2012;6(6):623-634. doi:10.3109/17435390.2011.598245.

152 Murugadoss S, Mülhopt S, Diabaté S, et al. Agglomeration State of Titanium-Dioxide (TiO2) Nanomaterials Influences the Dose Deposition and Cytotoxic Responses in Human Bronchial Epithelial Cells at the Air-Liquid Interface. *Nanomaterials (Basel)*. 2021;11(12). doi:10.3390/nano11123226.

153 Emura M, Aufderheide M, Mohr U. Target cell types with stem/progenitor function to isolate for in vitro reconstruction of human bronchiolar epithelia. *Exp Toxicol Pathol*. 2015;67(2):81-88. doi:10.1016/j.etp.2014.11.003.

154 Robinot R, Hubert M, Melo GD de, et al. SARS-CoV-2 infection induces the dedifferentiation of multiciliated cells and impairs mucociliary clearance. *Nat Commun*. 2021;12(1):4354. doi:10.1038/s41467-021-24521-x.

155 Meindl C, Stranzinger S, Dzidic N, et al. Permeation of Therapeutic Drugs in Different Formulations across the Airway Epithelium In Vitro. *PLoS ONE*. 2015;10(8):e0135690. doi:10.1371/journal.pone.0135690.

156 Turdalieva A, Solandt J, Shambetova N, et al. Bioelectric and Morphological Response of Liquid-Covered Human Airway Epithelial Calu-3 Cell Monolayer to Periodic Deposition of Colloidal 3-Mercaptopropionic-Acid Coated CdSe-CdS/ZnS Core-Multishell Quantum Dots. *PLoS ONE*. 2016;11(2):e0149915. doi:10.1371/journal.pone.0149915.

157 Schmid O, Stoeger T. Surface area is the biologically most effective dose metric for acute nanoparticle toxicity in the lung. *Journal of Aerosol Science*. 2016;99:133-143. doi:10.1016/j.jaerosci.2015.12.006.

158 Aufderheide M, Scheffler S, Ito S, Ishikawa S, Emura M. Ciliatoxicity in human primary bronchiolar epithelial cells after repeated exposure at the air-liquid interface with native mainstream smoke of K3R4F cigarettes with and without charcoal filter. *Exp Toxicol Pathol*. 2015;67(7-8):407-411. doi:10.1016/j.etp.2015.04.006.

159 Smyth T, Veazey J, Eliseeva S, Chalupa D, Elder A, Georas SN. Diesel exhaust particle exposure reduces expression of the epithelial tight junction protein Tricellulin. *Part Fibre Toxicol*. 2020;17(1):52. doi:10.1186/s12989-020-00383-x.

160 Zarcone MC, Duistermaat E, van Schadewijk A, Jedynska A, Hiemstra PS, Kooter IM. Cellular response of mucociliary differentiated primary bronchial epithelial cells to diesel exhaust. *Am J Physiol Lung Cell Mol Physiol*. 2016;311(1):L111-23. doi:10.1152/ajplung.00064.2016.

161 Dong Z, Yuan Y. Accelerated inflammation and oxidative stress induced by LPS in acute lung injury: Inhibition by ST1926. *Int J Mol Med*. 2018;41(6):3405-3421. doi:10.3892/ijmm.2018.3574.

162 Cabrera-Benítez NE, Pérez-Roth E, Ramos-Nuez Á, et al. Inhibition of endotoxin-induced airway epithelial cell injury by a novel family of pyrrol derivates. *Lab Invest*. 2016;96(6):632-640. doi:10.1038/labinvest.2016.46.

163 Brekman A, Walters MS, Tilley AE, Crystal RG. FOXJ1 prevents cilia growth inhibition by cigarette smoke in human airway epithelium in vitro. *Am J Respir Cell Mol Biol*. 2014;51(5):688-700. doi:10.1165/rcmb.2013-0363OC.

164 Valencia-Gattas M, Conner GE, Fregien NL. Gefitinib, an EGFR Tyrosine Kinase inhibitor, Prevents Smoke-Mediated Ciliated Airway Epithelial Cell Loss and Promotes Their Recovery. *PLoS ONE*. 2016;11(8):e0160216. doi:10.1371/journal.pone.0160216.

165 Amatngalim GD, Schrumpf JA, Dishchekenian F, et al. Aberrant epithelial differentiation by cigarette smoke dysregulates respiratory host defence. *Eur Respir J*. 2018;51(4). doi:10.1183/13993003.01009-2017.

166 Duclos GE, Teixeira VH, Autissier P, et al. Characterizing smoking-induced transcriptional heterogeneity in the human bronchial epithelium at single-cell resolution. *Sci Adv*. 2019;5(12):eaaw3413. doi:10.1126/sciadv.aaw3413.

167 Gindele JA, Kiechle T, Benediktus K, et al. Intermittent exposure to whole cigarette smoke alters the differentiation of primary small airway epithelial cells in the air-liquid interface culture. *Sci Rep*. 2020;10(1):6257. doi:10.1038/s41598-020-63345-5.

168 Tatsuta M, Kan-O K, Ishii Y, et al. Effects of cigarette smoke on barrier function and tight junction proteins in the bronchial epithelium: protective role of cathelicidin LL-37. *Respir Res*. 2019;20(1):251. doi:10.1186/s12931-019-1226-4.

169 Chen G, Korfhagen TR, Karp CL, et al. Foxa3 induces goblet cell metaplasia and inhibits innate antiviral immunity. *Am J Respir Crit Care Med*. 2014;189(3):301-313. doi:10.1164/rccm.201306-1181OC.

170 Ravindra NG, Alfajaro MM, Gasque V, et al. Single-cell longitudinal analysis of SARS-CoV-2 infection in human airway epithelium identifies target cells, alterations in gene expression, and cell state changes. *PLoS Biol*. 2021;19(3):e3001143. doi:10.1371/journal.pbio.3001143.

171 Gong H, Linn WS, Terrell SL, et al. Exposures of elderly volunteers with and without chronic obstructive pulmonary disease (COPD) to concentrated ambient fine particulate pollution. *Inhal Toxicol*. 2004;16(11-12):731-744. doi:10.1080/08958370490499906.

172 Gohy S, Carlier FM, Fregimilicka C, et al. Altered generation of ciliated cells in chronic obstructive pulmonary disease. *Sci Rep*. 2019;9(1):17963. doi:10.1038/s41598-019-54292-x.

173 Yaghi A, Dolovich MB. Airway Epithelial Cell Cilia and Obstructive Lung Disease. *Cells*. 2016;5(4). doi:10.3390/cells5040040.

174 Yaghi A, Zaman A, Cox G, Dolovich MB. Ciliary beating is depressed in nasal cilia from chronic obstructive pulmonary disease subjects. *Respir Med*. 2012;106(8):1139-1147. doi:10.1016/j.rmed.2012.04.001.

175 Ancel J, Belgacemi R, Diabasana Z, et al. Impaired Ciliary Beat Frequency and Ciliogenesis Alteration during Airway Epithelial Cell Differentiation in COPD. *Diagnostics (Basel)*. 2021;11(9). doi:10.3390/diagnostics11091579.

176 Thomas B, Koh MS, O'Callaghan C, et al. Dysfunctional Bronchial Cilia Are a Feature of Chronic Obstructive Pulmonary Disease (COPD). *COPD*. 2021;18(6):657-663. doi:10.1080/15412555.2021.1963695.

177 Xian M, Ma S, Wang K, et al. Particulate Matter 2.5 Causes Deficiency in Barrier Integrity in Human Nasal Epithelial Cells. *Allergy Asthma Immunol Res*. 2020;12(1):56-71. doi:10.4168/aair.2020.12.1.56.

178 Hedström U, Öberg L, Vaarala O, et al. Impaired Differentiation of Chronic Obstructive Pulmonary Disease Bronchial Epithelial Cells Grown on Bronchial Scaffolds. *Am J Respir Cell Mol Biol*. 2021;65(2):201-213. doi:10.1165/rcmb.2019-0395OC.

179 Bourdon JA, Saber AT, Jacobsen NR, et al. Carbon black nanoparticle instillation induces sustained inflammation and genotoxicity in mouse lung and liver. *Part Fibre Toxicol*. 2012;9:5. doi:10.1186/1743-8977-9-5.

180 Jackson P, Hougaard KS, Boisen AMZ, et al. Pulmonary exposure to carbon black by inhalation or instillation in pregnant mice: effects on liver DNA strand breaks in dams and offspring. *Nanotoxicology*. 2012;6(5):486-500. doi:10.3109/17435390.2011.587902.

181 Ghosh A, Coakley RC, Mascenik T, et al. Chronic E-Cigarette Exposure Alters the Human Bronchial Epithelial Proteome. *Am J Respir Crit Care Med*. 2018;198(1):67-76. doi:10.1164/rccm.201710-2033OC.

182 Parris BA, O'Farrell HE, Fong KM, Yang IA. Chronic obstructive pulmonary disease (COPD) and lung cancer: common pathways for pathogenesis. *J Thorac Dis*. 2019;11(Suppl 17):S2155-S2172. doi:10.21037/jtd.2019.10.54.

183 Scott ES, Goddard CA, Wiseman JW, Evans MJ, Colledge WH. A murine tracheal culture system to investigate parameters affecting gene therapy for cystic fibrosis. *Gene Ther*. 2000;7(7):612-618. doi:10.1038/sj.gt.3301148.

184 Rigden HM, Alias A, Havelock T, et al. Squamous Metaplasia Is Increased in the Bronchial Epithelium of Smokers with Chronic Obstructive Pulmonary Disease. *PLoS ONE*. 2016;11(5):e0156009. doi:10.1371/journal.pone.0156009.

185 Adcock IM, Caramori G, Barnes PJ. Chronic obstructive pulmonary disease and lung cancer: new molecular insights. *Respiration*. 2011;81(4):265-284. doi:10.1159/000324601.

186 Steiling K, Ryan J, Brody JS, Spira A. The field of tissue injury in the lung and airway. *Cancer Prev Res (Phila)*. 2008;1(6):396-403. doi:10.1158/1940-6207.CAPR-08-0174.

187 He L-X, Tang Z-H, Huang Q-S, Li W-H. DNA Methylation: A Potential Biomarker of Chronic Obstructive Pulmonary Disease. *Front Cell Dev Biol*. 2020;8:585. doi:10.3389/fcell.2020.00585.

188 Suzuki M, Wada H, Yoshino M, et al. Molecular characterization of chronic obstructive pulmonary disease-related non-small cell lung cancer through aberrant methylation and alterations of EGFR signaling. *Ann Surg Oncol*. 2010;17(3):878-888. doi:10.1245/s10434-009-0739-3.

189 Danahay H, Pessotti AD, Coote J, et al. Notch2 is required for inflammatory cytokine-driven goblet cell metaplasia in the lung. *Cell Rep*. 2015;10(2):239-252. doi:10.1016/j.celrep.2014.12.017.

190 Fujisawa T, Velichko S, Thai P, Hung L-Y, Huang F, Wu R. Regulation of airway MUC5AC expression by IL-1beta and IL-17A; the NF-kappaB paradigm. *J Immunol*. 2009;183(10):6236-6243. doi:10.4049/jimmunol.0900614.

191 Chen G, Sun L, Kato T, et al. IL-1β dominates the promucin secretory cytokine profile in cystic fibrosis. *J Clin Invest*. 2019;129(10):4433-4450. doi:10.1172/JCI125669.

192 Xia W, Bai J, Wu X, et al. Interleukin-17A promotes MUC5AC expression and goblet cell hyperplasia in nasal polyps via the Act1-mediated pathway. *PLoS ONE*. 2014;9(6):e98915. doi:10.1371/journal.pone.0098915.

193 Abdal Dayem A, Hossain MK, Lee SB, et al. The Role of Reactive Oxygen Species (ROS) in the Biological Activities of Metallic Nanoparticles. *Int J Mol Sci*. 2017;18(1). doi:10.3390/ijms18010120.

194 Birben E, Sahiner UM, Sackesen C, Erzurum S, Kalayci O. Oxidative stress and antioxidant defense. *World Allergy Organ J*. 2012;5(1):9-19. doi:10.1097/WOX.0b013e3182439613.

195 Crystal RG, Randell SH, Engelhardt JF, Voynow J, Sunday ME. Airway epithelial cells: current concepts and challenges. *Proc Am Thorac Soc*. 2008;5(7):772-777. doi:10.1513/pats.200805-041HR.

196 Hackett NR, Heguy A, Harvey B-G, et al. Variability of antioxidant-related gene expression in the airway epithelium of cigarette smokers. *Am J Respir Cell Mol Biol*. 2003;29(3 Pt 1):331-343. doi:10.1165/rcmb.2002-0321OC.

197 James A. Airway Remodeling in Asthma: Is it Fixed or Variable? *Am J Respir Crit Care Med*. 2017;195(8):968-970. doi:10.1164/rccm.201611-2285ED.

198 Ito JT, Lourenço JD, Righetti RF, Tibério IFLC, Prado CM, Lopes FDTQS. Extracellular Matrix Component Remodeling in Respiratory Diseases: What Has Been Found in Clinical and Experimental Studies? *Cells*. 2019;8(4). doi:10.3390/cells8040342.

199 Namvar S, Labram B, Rowley J, Herrick S. Aspergillus fumigatus-Host Interactions Mediating Airway Wall Remodelling in Asthma. *J Fungi (Basel)*. 2022;8(2). doi:10.3390/jof8020159.

200 Gohy ST, Hupin C, Fregimilicka C, et al. Imprinting of the COPD airway epithelium for dedifferentiation and mesenchymal transition. *Eur Respir J*. 2015;45(5):1258-1272. doi:10.1183/09031936.00135814.

201 He S, Chen D, Hu M, et al. Bronchial epithelial cell extracellular vesicles ameliorate epithelial-mesenchymal transition in COPD pathogenesis by alleviating M2 macrophage polarization. *Nanomedicine*. 2019;18:259-271. doi:10.1016/j.nano.2019.03.010.

202 Hedström U, Hallgren O, Öberg L, et al. Bronchial extracellular matrix from COPD patients induces altered gene expression in repopulated primary human bronchial epithelial cells. *Sci Rep*. 2018;8(1):3502. doi:10.1038/s41598-018-21727-w.

203 Wittekindt OH. Tight junctions in pulmonary epithelia during lung inflammation. *Pflugers Arch*. 2017;469(1):135-147. doi:10.1007/s00424-016-1917-3.

204 Cai Y, Varasteh S, van Putten JPM, Folkerts G, Braber S. Mannheimia haemolytica and lipopolysaccharide induce airway epithelial inflammatory responses in an extensively developed ex vivo calf model. *Sci Rep*. 2020;10(1):13042. doi:10.1038/s41598-020-69982-0.

205 Royer P-J, Henrio K, Pain M, et al. TLR3 promotes MMP-9 production in primary human airway epithelial cells through Wnt/β-catenin signaling. *Respir Res*. 2017;18(1):208. doi:10.1186/s12931-017-0690-y.

206 Ruffin M, Roussel L, Maillé É, Rousseau S, Brochiero E. Vx-809/Vx-770 treatment reduces inflammatory response to Pseudomonas aeruginosa in primary differentiated cystic fibrosis bronchial epithelial cells. *Am J Physiol Lung Cell Mol Physiol*. 2018;314(4):L635-L641. doi:10.1152/ajplung.00198.2017.

207 Murugadoss S, Brassinne F, Sebaihi N, et al. Agglomeration of titanium dioxide nanoparticles increases toxicological responses in vitro and in vivo. *Part Fibre Toxicol*. 2020;17(1):10. doi:10.1186/s12989-020-00341-7.

208 Ji J, Ganguly K, Mihai X, et al. Exposure of normal and chronic bronchitis-like mucosa models to aerosolized carbon nanoparticles: comparison of pro-inflammatory oxidative stress and tissue injury/repair responses. *Nanotoxicology*. 2019;13(10):1362-1379. doi:10.1080/17435390.2019.1655600.

209 Canivet L, Denayer F-O, Dubot P, Garçon G, Lo Guidice J-M. Toxicity of iron nanoparticles towards primary cultures of human bronchial epithelial cells. *J Appl Toxicol*. 2021;41(2):203-215. doi:10.1002/jat.4033.

Acknowledgements

Affidavit

LMU LUDWIG-MAXIMILIANS-UNIVERSITÄT MÜNCHEN	Promotionsbüro Medizinische Fakultät	MMRS	

Affidavit

Dr. med. Mircea-Gabriel Stoleriu

_____
Surname, first name

Robert-Koch-Alle 2_____
Street

82131, Munich-Gauting, Germany_____
Zip code, town, country

I hereby declare, that the submitted thesis entitled:

"Secretory to multi-ciliated cell imbalance by altered cellular progeny in end-stage COPD facilitates resilience to environmental pollutants"

is my own work. I have only used the sources indicated and have not made unauthorised use of services of a third party. Where the work of others has been quoted or reproduced, the source is always given.

I further declare that the submitted thesis or parts thereof have not been presented as part of an examination degree to any other university.

Munich,
8.11.2022   Mircea-Gabriel Stoleriu
place, date   Signature doctoral candidate

Confirmation of congruency

LUDWIG-MAXIMILIANS-UNIVERSITÄT MÜNCHEN	Promotionsbüro Medizinische Fakultät

Confirmation of congruency between printed and electronic version of the doctoral thesis

Dr. med. Mircea-Gabriel Stoleriu

_____
Surname, first name

Robert-Koch-Alle 2_____
Street

82131, Munich-Gauting, Germany _____
Zip code, town, country

I hereby declare, that the submitted thesis entitled:

"Secretory to multi-ciliated cell imbalance by altered cellular progeny in end-stage COPD facilitates resilience to environmental pollutants"

……….

is congruent with the printed version both in content and format.

Munich,
8.11.2022   Mircea-Gabriel Stoleriu
place, date   Signature doctoral candidate

Author contributions (alphabetical order)

M. Ansari and Prof. Dr. F.J. Theis: analyzed the single cell data (**Figure 38-48**), interpreted the single cell and transcriptome data and revised the manuscript

Prof. Dr. J. Beckers, Dr. M. Irmler: performed the transcriptome analysis upon RNA isolation, provided and interpreted the transcriptome data of the NP exposed ALI cultures

Prof. Dr. J. Behr: provided support in the clinical data collection and results interpretation, analyzed and interpreted the data, revised the manuscript

Dr. G. Burgstaller, M. Gerckens: established the novel IF protocol for bronchial punches, gave support for IF data representation and quantification (bronchial punches, **Figure 31**)

A. Castelblanco: developed an automated tool for the quantification and statistical analysis of ciliary beating frequencies for the recorded videos at ALI (**Figure 18, 24, 27, 37**)

Dr. Y. Ding, Dr. O. Schmid, Dr. T. Stoeger, Dr. C.Voss: gave support in the exposure experiments (ALICE CLOUD System), analyzed and interpreted the data, revised the manuscript (**Figure 13-14**)

Prof. Dr. O. Eickelberg, Dr. A.C. Schamberger: gave support in the establishment of the 3D ALI cultures, analyzed and interpreted the data

Dr. J.M. Fertmann, PD Dr. T. Kauke, PD Dr. Ch. Schneider: performed the surgical procedures in all patients undergoing lung transplantation and provided native bronchial tissue samples for the CPC-M bioarchive, gave scientific feedback and interpreted the data

Prof. Dr. Dr. R. Hatz, Dr. M. Lindner: performed the surgical procedures in all tumor patients included in the study and provided native bronchial tissue samples for the CPC-M bioarchive, gave scientific feedback, interpreted the data and revised the manuscript

Prof. Dr. S Hauck: performed the secretome analysis and interpreted the secretome data

Dr. M. Heydarian: performed IF stainings of the paraffin embedded native bronchial tissue samples, quantified and interpreted the stainings (**Figure 33, 43**).

PD Dr. A. Hilgendorff: Principal Investigator and Supervisor of the project, designed the study, planed the experiments, analyzed and interpreted all data, revised the manuscript

Dr. H. Schiller: designed the study, analyzed and interpreted the single cell data (**Figure 38-48**), interpreted the multi-omics data and revised the manuscript

J.J. Schneider: performed in collab. with Dr. M.G. Stoleriu the ALI cultures, CSE exposures, functional assays (TEER, WST, LDH) and IF for CSE experiments (**Figure 34, 35**)

Dr. B. Schubert: supervised the statistical analysis for secretome and transcriptome data

Dr. M.G. Stoleriu: drafted the manuscript, performed the 3D ALI cultures (*in vitro*, *ex vivo*) and nanoparticle exposures, performed and analyzed the functional assays (TEER, WST, LDH, CBF) as well as IF, RNA and protein isolation

Dr. M. Strunz: performed in collab. with Dr. M.G. Stoleriu the single cell isolation and analysis, collected data and evaluated the single cell results (**Figure 38-48**)

List of publications

<u>Publication Originating from this thesis</u>

1 **Stoleriu MG**, Ansari M, Strunz M, et al. Secretory to multi-ciliated cell imbalance by altered cellular progeny in end-stage COPD facilitates resilience to environmental pollutants (in preparation).

<u>Publications not included into this thesis:</u>

1 **Stoleriu MG**, Steger V, Mustafi M, et al. A new strategy in the treatment of chemoresistant lung adenocarcinoma via specific siRNA transfection of SRF, E2F1, Survivin, HIF and STAT3. Eur J Cardiothorac Surg. 2014;46(5):877-886. doi:10.1093/ejcts/ezu087.

2 **Stoleriu MG**, Gerckens M, Hetrodt J, et al. Clinical Course of Three Postoperative Symptomatic COVID-19 Cases in Patients After Lung Lobectomy. Ann Thorac Surg. 2020;110(6):e461-e463. doi:10.1016/j.athoracsur.2020.06.001.

3 **Stoleriu MG**, Gerckens M, Obereisenbuchner F, et al. Automated quantitative thin slice volumetric low dose CT analysis predicts disease severity in COVID-19 patients. Clin Imaging. 2021; 79:96-101. doi:10.1016/j.clinimag.2021.04.008.

4 **Stoleriu MG**, Gerckens M, Ströh K, et al. Prävention postoperativer COVID-19-Erkrankungen in der Thoraxchirurgie: Lehren aus der ersten COVID-19-Welle. Pneumologie. 2021;75(12):960-970. doi:10.1055/a-1526-9979.

5 Fischer DS, Ansari M, Wagner KI, et al. Single-cell RNA sequencing reveals *ex vivo* signatures of SARS-CoV-2-reactive T cells through 'reverse phenotyping'. Nat Commun. 2021;12(1):4515. doi:10.1038/s41467-021-24730-4.

6 Gerckens M, Schorpp K, Pelizza F, et al. Phenotypic drug screening in a human fibrosis model identified a novel class of antifibrotic therapeutics. Sci Adv. 2021;7(52):eabb3673. doi:10.1126/sciadv.abb3673.

7 Timing of surgery following SARS-CoV-2 infection: an international prospective cohort study. Anaesthesia. 2021;76(6):748-758. doi:10.1111/anae.15458.

8 SARS-CoV-2 vaccination modelling for safe surgery to save lives: data from an international prospective cohort study. Br J Surg. 2021;108(9):1056-1063. doi:10.1093/bjs/znab101.

9 Effects of pre-operative isolation on postoperative pulmonary complications after elective surgery: an international prospective cohort study. Anaesthesia. 2021;76(11):1454-1464. doi:10.1111/anae.15560.

10 SARS-CoV-2 infection and venous thromboembolism after surgery: an international prospective cohort study. Anaesthesia. 2022;77(1):28-39. doi:10.1111/anae.15563.

11 Ambike S, Cheng C-C, Feuerherd M, et al. Targeting genomic SARS-CoV-2 RNA with siRNAs allows efficient inhibition of viral replication and spread. Nucleic Acids Res. 2022;50(1):333-349. doi:10.1093/nar/gkab1248.